UNIVERSITÀ
DEGLI STUDI
FIRENZE

DOTTORATO DI RICERCA IN
INGEGNERIA INDUSTRIALE

Curriculum:
ENERGETICA E TECNOLOGIE INDUSTRIALI ED AMBIENTALI INNOVATIVE

CICLO XXXIII
COORDINATORE Prof. Giampaolo Manfrida

Design Solutions for Reducing Losses in Aeronautical Low-Pressure Turbines

Settore scientifico disciplinare ING-IND/08

Dottorando
Giorgio Amato

Tutor
Prof. Andrea Arnone

Coordinatore
Prof. Giampaolo Manfrida

Firenze 2017/2020

... o resterai più semplicemente
dove un attimo vale un altro
senza chiederti come mai,
continuerai a farti scegliere o
finalmente sceglierai.»

Fabrizio De André

Abstract

The present thesis deals with the generation of innovative design solutions for reducing aerodynamic losses in Low-Pressure Turbines through the combined use of Artificial Neural Networks and CFD (Computational Fluid Dynamics). In particular, a lean model for optimizing blade airfoils in a multi-row environment and the development of a passive control device for reducing secondary losses are presented.

The first procedure allows building a 1.5 stage by starting from a single blade profile, which is one of the main focuses of low TRL (Technology Readiness Level) design activities. In the obtained setup, two airfoil aerodynamic optimizations are performed by considering steady and unsteady conditions separately. The evaluation of the unsteady phenomena proves to be critical already at the considered blade design stage. Indeed, such practice allows achieving better aerodynamic performance and reducing the blade count per row.

The second part of the thesis explains the blade fence development, which has been performed in collaboration with Avio Aero and Università degli Studi di Genova (UniGE). Such shelf-like devices are applied onto the blade surface to hinder the generation of secondary flows. The blade fence shape is the result of numerical aerodynamic optimizations so that the devices determine the reduction not only of the secondary loss but also of the flow turning deviation at the vane outlet. Such beneficial effects are also confirmed by the results of the experimental campaign conducted by UniGE on linear cascades.

Contents

List of Figures

List of Tables

Nomenclature

A	Surface area
AI	Artificial Intelligence
ANN	Artificial Neural Network
AR	Aspect Ratio
B2B	Blade-to-Blade
BC	Boundary Condition
BDF	Backward Difference Formula
BPR	By-Pass Ratio
C	Blade chord or Coefficient
c	Absolute velocity
cf	Skin friction coefficient
CFD	Computational Fluid Dynamics
CFL	Courant-Friedrichs-Lewy number
cp	Pressure coefficient
CSV	Corner Shed Vortex
CV	Corner Vortex
DF	Diffusion Factor
DoF	Degree of Freedom
DR	Diffusion Rate
EXP	Experiments
f	Predominant frequency or Activation function
$\bar{f}$	Reduced frequency
g	Blade gap
GE	General Electric
GPU	Graphics Processing Unit
h	Enthalpy
H	Shape factor or Blade height

k	Thermal conductivity or wave number
LE	Leading Edge
LPT	Low-Pressure Turbine
$\dot{m}$	Mass-flow
M	Mach number
N	Number of time samplings or cells
n	Normal direction or Width
OPT	Optimum geometry
p	Pressure
R	Gas constant or Residual
r	Radius
R&D	Research and Development
Re	Reynolds number
S	Steady
s	Entropy or Curvilinear abscissa or Space
SFC	Specific Fuel Consumption
T	Temperature or Disturbance passing period
t	Time or Thickness
TE	Trailing Edge
TEWV	Trailing Edge Wake Vortex
TKE	Turbulent Kinetic Energy
TLS	Turbulent Length Scale
TRL	Technology Readiness Level
Tu	Turbulent intensity
U	Velocity or Unsteady
u	Peripheral velocity
UGT	Unguided Turning
(U)RANS	(Unsteady) Reynolds-Averaged Navier-Stokes
UniFI	Università degli Studi di Firenze
UniGE	Università degli Studi di Genova
V	Volume or Vortex
v	Relative velocity
w/o	without

Y or cpt	Total pressure loss coefficient
Z	Zweifel number

Greek

α	Blade-to-blade flow angle
β	Meridian flow angle
γ	Intermittency
δ	Boundary layer thickness
δ^*	Boundary layer displacement thickness
ζ	Entropy loss coefficient or Energy loss coefficient
η	Efficiency
θ	Momentum thickness
ν	Fluid kinematic viscosity
ρ	Fluid density
σ	Rate of entropy generation per unit volume
ϕ	Flow coefficient
ω	Angular velocity

Subscripts

0	Stagnation quantity
∞	Free-stream
θ,t	Momentum thickness at transition onset
ax,x	Axial
bsl	baseline
is	Isentropic transformation
in or 1	at inlet to blade row or stage
out or 2	at exit from blade row or stage
ref	Reference quantity
SKE	Secondary Kinetic Energy
sec	Secondary
tt	Total-to-total

1 Introduction

The development of the civil aeronautical sector has been dramatically fast during the last decades and has undoubtedly contributed to achieving the present level of welfare in the most developed countries. It is worth noting that not only the annual flight number has increased, but also the linked industrial activities have remarkably developed. The European passengers in 2018 were 1106 million: such a datum corresponds to an increase of 6% compared with 2017 and is about three times more than in 1992 [1], [2]. However, the COVID-19 pandemic has been determining dramatic consequences on the sector. In 2020, the traffic decreased by 88% in April and 54% in September compared to the same periods in 2019 [3].

Anyway, before the pandemic, the aeronautical sector has been heavily criticized for its environmental impact. If, on the one hand, the aircraft emissions are far lower per km flown than in the past (54 kg/passenger in 2015 against 85 kg/passenger in 1992 [2]), on the other hand, the traffic increase has determined the necessity of new strategies to protect the planet [4], [5]. The goals, which the European Union has set itself, are ambitious, and consequently, the efforts in the Research and Development (R&D) sectors must be increased. However, not only the technical challenges need to be faced, but also the economic ones. Indeed, the average budget for R&D in civil aeronautics is already high: about 7 billion € per year [6].

Besides, it is worth noting that the reported data refer to Europe only, while the aeronautical sector growth concerns the entire globe. Therefore, environmental protection must become a

priority for every nation in order to achieve effective results in reducing air pollution and limiting global climate change.

As far as technical challenges are concerned, CFD (Computational Fluid Dynamics) has been playing a fundamental role for decades since it has allowed reducing the number of experiments and prototypes to design any new device. As a consequence, both the cost and time of production have remarkably reduced. Moreover, the steep development of computational resources and the introduction of high-computing clusters and GPUs have made the use of high-fidelity approaches affordable for many research applications. However, they are still too demanding for the industrial design of turbomachines, and especially for the multi-stage ones that operate at high Reynolds numbers.

So far, high-fidelity CFD models may be thought of as approaches to deepen the flow-field knowledge within limited computational domains. Alternatively, they can be used to improve the standard URANS (Unsteady Reynolds Averaged Navier-Stokes) approaches by calibrating the inner models through the high-fidelity analysis data [7], [8].

In summary, URANS approaches are far the most widespread models among R&D groups in the aeronautical sector as they are, at present, the best trade-off between result accuracy and computational cost for the CFD simulations. More in details, the unsteady (URANS) models are mainly used in the design validation phase or for research activities since their computational cost is still incompatible with the routine design practice of multi-stage turbomachines. By contrast, the out-and-out design is generally performed via steady (RANS) simulations.

Besides the CFD, Artificial Intelligence (AI) has been providing relevant contributions to R&D groups in the aeronautical sector. Indeed, it allows generating new geometries for whatever component by learning from the large amount of data that is stored in company archives. Furthermore, the coupling of AI and CFD turns out to be perfect for design purposes, since the new geometries generated by the former tool can be promptly analyzed via the latter one.

In this frame, the work presented in the thesis aims to take advantage of the aforementioned numerical tools to develop innovative design solutions for reducing the aerodynamic losses in aeronautical Low-Pressure Turbines (LPTs). More in details, the coupling of RANS/URANS approaches with Artificial Neural Networks (ANNs) is used to perform two different tasks. The first one refers to the implementation of a lean method to carry out aerodynamic optimizations of LPT blade airfoils within multi-row environments. The second one, instead, concerns the development of a novel device, referred to as blade fence, for reducing secondary losses.

The main physical phenomena occurring within LPTs are widely explained in chapter 2 by highlighting the interactions and the interconnections that are typical of real flow-fields. Such detailed bibliographical research has been conducted to provide a solid theoretical background for the research activities presented in the thesis. In other words, chapter 2 provides the key to identify the best and simultaneously feasible solutions for LPTs among the infinite options obtained through ANNs and CFD.

In chapter 3, a brief overview of the numerical methods used throughout the PhD is reported. In particular, the description

of the main features of the adopted CFD code (named TRAF) and ANN model is provided.

Then, the method for optimizing blade airfoils is explained in chapter 4. It refers to low TRL design phases in which single blade profiles are usually analyzed, and thus the process to build the multi-row environment is first shown. The analyses to generate the database for ANN training are performed via both RANS and URANS approaches so that a comparison between the optimal geometries obtained under steady and unsteady conditions is possible. In particular, the differences in design specifications and flow-field patterns are highlighted. Moreover, the aerodynamic performance of the optimal airfoils is investigated under off-design conditions.

In chapter 5, the activity about the blade fences is presented. The device is one of the main results originating from the joint project among the TRAF-group (T-group) of Università degli Studi di Firenze (UniFI), Avio Aero (a GE Aviation Business) and the Aerodynamics and Turbomachinery laboratory of Università degli Studi di Genova (UniGE). In particular, the device concept has been developed via the aforementioned numerical tools. Indeed, the extensive optimization process to determine the fence shape is presented in the first part of the chapter. Then, the main details of the experimental test-rig used for the device performance measurements, performed at UniGE, are reported. Finally, the results of the experimental and CFD analyses for validating the fence effects are shown for both design and off-design conditions.

It is worth noting that the development and validation of blade fences are reported in a two-part paper [9], [10] that was presented at ASME Turbo Expo 2019 in Phoenix, AR, USA.

In conclusion, closing remarks and some hints for future developments of the work presented within the thesis are reported in chapter 6.

2 The Aeronautical Low-Pressure Turbine

The aeronautical low-pressure turbine (LPT) is one of the main components of the turbofan engines. As it is directly coupled to the fan in conventional engines, many constraints must be considered during the design process. The LPT rotational speed must be low to maintain feasible values for the blade tip peripheral velocity of the fan. The diameter of the latter is much larger than that of the LPT, which is furtherly limited by the presence of the by-pass duct. These two aspects cause the average velocity of turbine blades to be low (Mach number (M) equal to 0.4 - 0.7), and thus the work output of a single stage is limited. In light of this, the number of stages in LPTs is relatively high. These characteristics determine both a great weight (about 20-30% of the overall engine weight) and a high number of expensive components. Although the efficiency of modern LPTs is already higher than 90%, the necessity of further improvements becomes clear by considering this data: a 1% decrease in direct operating costs of the engine, which may be obtained through a 1% increase in the component efficiency or through a 17% decrease in the engine weight, corresponds to the reduction of about $ 200000 of the annual flight cost of one single aircraft [11].

In this frame, the trend with commercial aeroengines concerns the increase of the propulsive efficiency since the thermodynamic one is already close to its asymptotical value. Such an improvement may be achieved by increasing the by-pass ratio (BPR). For a BPR greater than 10, the conventional engine architecture may become less performant than the geared

one since the latter allows decoupling the rotational velocity of fan and LPT, reducing the number of components, and thus lowering the overall risk of failure [12].

Anyway, the increase in BPR determines two main variations in the LPT design specifications. First, the adoption of ultra-high lift profiles in order to provide the required work output through a lower number of blades or even stages. Second, the decrease in the diameter of LPTs and thus of their aspect ratio. Such a change determines the rising relative importance of secondary flows as the span fraction affected by endwall flow structures increases.

The present chapter has the purpose of introducing the theoretical issues related to the research activities reported in the remainder of the thesis. After a brief description of the concept of aerodynamic loss and the main methods to assess the performance of the engine components, the physical phenomena that mostly affect the state-of-the-art LPTs are examined in depth. In particular, it is reported a focus about the unsteady disturbances, the transition mechanism and the secondary flows. Finally, the interaction between incoming wakes and blades is analyzed by highlighting the influence on the three aforementioned physical phenomena.

2.1 Aerodynamic Performance

The efficiency is one of the most important performance parameters for aeroengines as it significantly affects the fuel consumption and thus the impact of flights from the point of

view of both the environment and economics. However, the aeroengine overall efficiency is the composition of the efficiency of each component and, in particular, the LPT efficiency turns out to be closely related to the overall performance. Indeed, an 1% increase in LPT polytropic efficiency leads to a 0.7% increase in the overall engine efficiency [13] and a 0.5-1% decrease in SFC. [11]. The concept of loss within turbomachines is directly connected to that of efficiency, i.e., every flow feature that involves an efficiency reduction may be considered a loss. From a thermodynamic point of view, any flow irreversibility determines the generation of entropy and consequently a reduction of isentropic efficiency. In other words, any fluid dynamic mechanism creating entropy is a source of loss and it is thus possible to define loss coefficients for single blades in terms of entropy generation. The entropy does not depend on the frame of reference and is an additive property: every measure of entropy change takes into account all the loss mechanisms occurred upstream of the considered measurement plane. Entropy change also contemplates losses due to unsteady effects, such as the energy separation [14]. It is worth noting that this property is locally evaluated, and its absolute value is always arbitrary. Therefore, Denton [15] defined the entropy loss coefficient for turbines by

$$\zeta_s = \frac{T_{out}\Delta s}{h_{0,out} - h_{out}} \tag{2.1}$$

Then, Chaluvadi [16] introduced the following equation to compute the rate of entropy generation per unit volume (σ) due to the viscous dissipation within a volume V of surface A:

$$\int_V \sigma \, \mathrm{d}V + \int_A \frac{k}{T} \nabla T \cdot \vec{n} \, \mathrm{d}A = \frac{\partial}{\partial t} \int_V \rho s \; dV \; + \int_A \rho s \, \vec{v} \cdot \vec{n} \, \mathrm{d}A \tag{2.2}$$

where k is the thermal conductivity, and T is the temperature.

However, in cascades, the use of entropy loss coefficient is not as common as that of energy loss coefficient, which turns out to be very useful for design purposes. For turbines, it is defined by

$$\zeta = \frac{h_{out} - h_{out,s}}{h_{0,out} - h_{out}} \tag{2.3}$$

It is worth noting that for stationary cascade blades, where the fluid is adiabatic, the loss of total pressure and the entropy change are conceptually equivalent. Indeed, for small changes in total pressure:

$$\Delta s = -R \frac{\Delta p_0}{p_0} \tag{2.4}$$

For this reason, the loss in cascade tests is often evaluated through the total pressure loss coefficient, which is also extremely easy to calculate. For turbines, it may be defined by

$$Y = \frac{p_{0,in} - p_{0,out}}{p_{0,out} - p_{out}} \tag{2.5}$$

In conclusion, for M smaller than 0.3, all the definitions of loss coefficients are practically equivalent so that the use of the total pressure loss coefficient in low-speed tests turns out to be not only theoretically justified but also fairly accurate.

Although many different loss coefficients are reported in literature, the aforementioned ones are probably the most used to evaluate the amount of loss as well as to investigate the sources of the loss itself. The mechanisms, which produce entropy in turbomachines, are basically three: the viscous friction, the heat transfer and the nonequilibrium processes (shock waves and quick expansions). It is often stated that the entropy change within a turbomachine is closely related to the

turbulent kinetic energy (TKE) production. Turbulence is an extremely complex phenomenon and deserves a specific explanation, albeit concise. According to the process of energy cascade, at high values of Reynolds number (Re), mean flow instabilities determine the generation of small structures, which get TKE from the mean flow itself and in turn transport TKE to the smaller scales. As a consequence, the viscosity preserves a key role regardless of the global value of Re since the latter locally remains low for the small structures. As flow scales become so small that they are not able to furtherly transfer TKE to the smaller ones, they convert TKE into heat. These purely viscous dissipative scales are referred to as Kolmogorov microscales. The enhanced diffusion of physical properties and the mechanical energy dissipation, which are characteristic aspects of turbulent flows, are substantially driven by the microscales themselves. Because of the operating conditions of civil aeronautical LPTs, the entropy generation is mostly due to viscous shear and turbulence production. The former occurs within both the boundary layer and the free shear layer, such as in mixing processes. Conversely, turbulence production mostly occurs within wakes and turbulent boundary layers. More in details, the viscous dissipation is predominant in the stagnation region near the LE, within the pressure side boundary layer and even within the accelerating part of the suction side boundary layer. On the other hand, turbulence produces more losses within the decelerating part of the suction side boundary layer as the TKE embedded within the wakes of the upstream rows severely alters the transition process [17].

2.1.1 Loss Breakdown

The historical loss breakdown reported below is an attempt to evaluate the effect of irreversible processes on total loss by separately considering the different blade regions. Although it is well known that loss mechanisms are usually not independent, the loss breakdown approach is still widely used in the design process since it allows quantifying the impact of specific design choices or devices.

Profile loss. The entropy generation over blade surfaces (far from the endwalls) depends on the development of boundary layers. More in details, the sources of profile losses are the viscous friction within the boundary layer over the entire blade surface, the mixing of suction and pressure boundary layers downstream of the trailing edge (TE), the flow separations and the shock waves. The latter does not usually occur in civil aircraft LPTs and thus they are neglected in the remainder of the present work. The blade boundary layer loss accounts for over the 50% of the overall profile loss and reaches even larger values in LPTs since their blades are characterized by large aspect ratios (usually in the range 3-7). This loss is related to the fraction of work lost to overcome the viscous shear near the wall. The no-slip condition locally induces significant velocity gradients in the normal direction so that the entropy generation mainly occurs in the inner part of the boundary layer, especially for turbulent flows in which the velocity distribution changes more sharply near the blade surface. The magnitude of the loss depends on the boundary layer development, which in turn is driven by Re, the turbulence level and the pressure distribution over the blade surface. Moreover, these features are closely related to the transition process. Since the blade surface regions

where the velocity is higher produce a larger amount of loss, the suction side impact is dominant over that of the pressure side. In other words, the losses generated within laminar boundary layers are much lower than those produced within the turbulent ones. Consequently, the transition onset position over the suction surface has a remarkable impact on the overall profile loss. It is worth noting that the boundary layer state also determines the intensity of other detrimental effects: the blockage and the aerodynamic drag. Moving forward, the TE mixing loss is due to the steep local variation of velocity and pressure: the flow experiences a sort of sudden increase of cross-section. Moreover, the boundary layer separates on both sides of the blade, and consequently, two counterrotating vortices develop right downstream within the so-called base region: its pressure, referred to as base pressure, turns out to be lower than that at row outlet. The low pressure acting on the TE causes entropy generation, as well as the mixing of the boundary layer just before the TE and the blockage effect. The latter is induced by both the TE thickness and the local boundary layer thickness. Therefore, the TE mixing loss depends on the boundary layer development, on the ratio of the TE thickness against the boundary layer thickness and on the TE shape. It is worth noting that this loss accounts for about the 35% of the overall profile loss, although its impact may be lower in LPTs (without large separations) since the TEs are relatively thin. Finally, the separation loss occurs when the blade boundary layer separates from the surface and separation bubbles containing low momentum flow develop right downstream. The magnitude of this loss is relevant only when separation bubbles are large, i.e., the effect of the separation bubble is not locally confined. In that case, the blade loading reduces as well as the aerodynamic performance. Furthermore, the presence of large

separations induces larger vortices downstream of the TE. They are associated with a higher dissipation within the wake. Conversely, short bubbles induce local effects on pressure distribution with a lower impact on the overall performance. In light of this, the evaluation of the boundary layer state is crucial to limit the amount of loss. It is usually evaluated through the so-called shape factor (H), which is defined by

$$H = \frac{\delta^*}{\theta} \tag{2.6}$$

where $\delta*$ and θ are integral parameters of the boundary layer referred to as displacement thickness and momentum thickness, respectively. For compressible flows, they are defined by:

$$\delta^* = \int_0^\infty \left(1 - \frac{\rho(y)\ u(y)}{\rho_\infty\ U_\infty}\right) dy \tag{2.7}$$

$$\theta = \int_0^\infty \frac{\rho(y)\ u(y)}{\rho_\infty\ U_\infty} \left(1 - \frac{u(y)}{U_\infty}\right) dy \tag{2.8}$$

The most relevant values of the shape factor are 2-3 for laminar flows, 1.4-1.6 for turbulent flows and greater than 3.5 for separated flows. Finally, it is worth noting that in the operating range of civil aeronautical LPTs the impact of Mach number (M) on the profile loss is deemed to be low [15].

Secondary (or Endwall) loss. The boundary layer developing over the hub and casing surfaces gives rise to losses within and outside of the blade vane. Indeed, about 2/3 of the total entropy generation near the endwalls is due to the viscous shear near the endwalls located upstream of the blade leading edge (LE) and downstream of its TE. The endwall boundary layer at blade inlet, in turn, causes the generation of secondary flows within the blade passage. Since it is an inviscid

phenomenon, secondary flows do not by themselves generate losses. However, they enhance the mixing out of the endwall boundary layer through the passage so that entropy generation increases. Secondary flows also alter the transition and separation mechanisms over the blade surface since they force low-momentum fluid off the wall. Moreover, a large amount of loss is connected to the dissipation that occurs within the core of the vortical structures. The latter mechanism accounts for about 30% of the overall endwall loss [18]. Since the trend with modern aeroengines concerns the BPR increase, the incidence of secondary loss on LPT overall losses may rise with respect to the 20-25% of the conventional engines.

Leakage loss. The flow convecting through the blade clearance gap is referred to as leakage flow and determines two effects: the reduction of the mass flow rate through the passage and the entropy rise. The first causes the work done by the turbine and the pressure drop to diminish. On the other hand, the second determines the efficiency reduction since entropy generation occurs due to mixing and viscous friction at the casing wall within the clearance. Also, losses increase at the suction side where the leakage flow undergoes mixing with the main flow. More in details, a vortex sheet generates at the interface between the two flows since their velocities differ in both magnitude and direction. As the leakage flow convects downstream, the vortex sheet rolls up into a concentrated vortex. As far as tip leakage loss is concerned, its magnitude is closely related to the presence of the blade shroud. In that case, the interaction between the leakage flow and the main one is significantly reduced. In addition, the pressure gradient driving the leakage flow changes.

For unshrouded blades, the leakage flow is determined by the pressure difference between pressure and suction side, while for shrouded blades it is caused by the pressure drop from upstream to downstream of the blade. Finally, it is worth noting that the tip leakage loss, which accounts for about 30% of the total loss, largely depends on the ratio of the clearance gap to the blade height: an increase of 1% in that ratio determines a loss of 2-3% of the efficiency [19].

So far, blade profiles have been considered in a steady setup, i.e., without incoming wakes. The impact of unsteadiness, and above all incoming wakes, significantly affects the amount of the overall loss since the unsteady disturbances determine both TKE migration and production.

First, turbulent structures transported by wakes interact with the blade boundary layer, especially with that over the decelerating part of the suction side. The transition mechanism may be substantially altered by the wake passing, and consequently, the extent of laminar and turbulent regions may change. As the profile loss is largely dependent on the transition onset position, the wake-blade interaction plays a key role in loss generation. The wake-induced transition occurs upstream of the steady transition onset so that the extent of the suction turbulent region grows, and the related losses increase as well. Conversely, the induced transition turns out to be beneficial in presence of large separations when it leads to the early bubble reattachment. In addition, although the magnitude of loss is much lower on the pressure side, the interaction between wakes and the local blade boundary layer is remarkable, as confirmed by the coherent structures induced in the near-wall region [17].

Second, travelling downstream, incoming wakes experience diffusion, which damps the momentum deficit, and undergo the deformation process within the blade passage that causes entropy generation in the core-flow. That loss production within the wake region is due to the shear stress and above all to the local TKE production, which is then transported beyond the TE.

In light of this, the entropy generation within the vane significantly rises as the number of wakes, which simultaneously occupy the passage, increases. However, high values of blade passing frequency correspond to a short circumferential distance between consecutive wakes, and consequently, the wake-to-wake interaction enhances so that each wake weakens before entering the blade passage. By increasing the reduced frequency ($\bar{f}$) (paragraph 2.2), the phenomenon of wake-merging leads to the formation of a high background turbulent intensity (Tu) rather than discrete unsteady patches, each associated with high Tu. This high freestream turbulence improves the stability of the suction surface boundary layer so that the impact of unsteadiness on the profile loss greatly diminishes. Furthermore, when wakes interact before the blade LE, they undergo diffusion within a region with constant surface area in the stream-wise direction; therefore, the amount of loss due to wake mixing considerably diminishes. Moreover, no discrete wakes enter the blade passage, and this results in a lower turbulence production even within the vane.

To summarize, if the circumferential distance between successive wakes is short, the overall loss significantly lowers. However, not only the $\bar{f}$ on wake-merging but also the flow coefficient ($\phi = \frac{c_x}{u}$) turns out to modify the intensity of this phenomenon. In fact, the wake trajectories become more

tangential by reducing ϕ: the longer the path, the stronger the wake decay. As a consequence, for low values of ϕ, incoming wakes induce lower unsteadiness even on the blade pressure side, and thus the resulting skin friction diminishes [20]. In conclusion, it is worth noting that a low amount of loss in the freestream is produced even in steady conditions since the homogeneous freestream turbulence decays while migrating [21].

2.2 Unsteadiness

The flow within turbomachines is intrinsically unsteady due to the interactions between rows that are in relative motion. Unsteadiness affects turbomachine performance in several ways. First, it alters the distributions of pressure and temperature on blade and endwall surfaces by modifying the aerodynamic loading and heat-exchange properties. The aerodynamic design has neglected the unsteady effects for decades considering them negative for performance a priori. Conversely, the role of unsteadiness has been assuming increasing importance as the understanding of its mechanisms and its effects deepens. Furthermore, pressure fluctuations are the main cause of aero-elastic and aero-acoustic issues, which contribute to high-cycle fatigue stress, and the simultaneously presence of thermal loadings causes the risk of blade failure to increase.

In light of this, the design process not only should consider the unsteady phenomena but also should adopt a multi-disciplinary approach to achieve better performance and more reliability. Consequently, the complexity of the design process would

dramatically increase as each branch has specific requirements, and the solutions that turn out to be beneficial for some disciplines are often detrimental for others.

It is common to classify the unsteady disturbances into flow-field interactions, which are deterministic, or instabilities, which are conversely stochastic. For example, the wake-blade interaction and the clocking are deterministic phenomena as they show a periodic pattern that depends on the machine operating point and the blade count. In other words, the characteristic frequencies of these interactions are a function of the rotational speed and the geometry of the considered turbine. On the other hand, phenomena, such as the TE vortex shedding or the flutter, are stochastic since their frequency is not ascribable to the machine geometry.

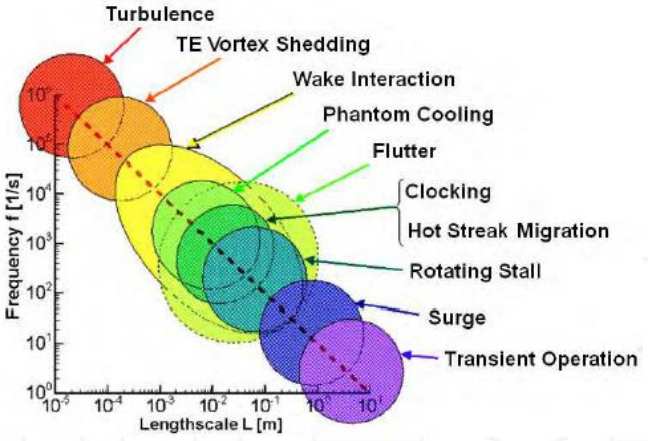

Figure 2.1: Time and length scales of unsteady mechanisms within turbomachines [22]

Figure 2.1 shows the time and spatial scales of perturbations, which are the source of fluctuations themselves and characterize flows within turbomachines. The complexity of the problem regarding unsteadiness is apparent by considering that the spectrum of flow structures includes five and six orders of magnitude in length- and time-scales, respectively.

As far as LPTs are concerned, the most important unsteady mechanisms occurring within this type of turbomachines are listed and explained below. For the sake of simplicity, a single stage is taken into account in the explanations. In other words, interactions among rows of different stages are not considered in the present paragraph.

Wake-blade interaction. The wake is a flow structure characterized by constant static pressure and a velocity deficit in the body-relative frame. Differently from the potential field it propagates by convection, thus only travels downstream of the blade TE. The stator wakes interact with the rotor blades generating an unsteady force field on the latter and pressure waves within the fluid, which cause acoustic emissions. In addition, the variation over time of the rotor pressure field influences the heat exchange between fluid and blade. All these interactions are related to the transition mechanism since the boundary layer state significantly affects the fluid physics.

Potential interaction. This phenomenon arises because every blade has a potential field (due to circulation), which propagates throughout space. In order to understand the unsteady effects generated by the potential interactions, it is possible to decompose the pressure field in the region between stator and rotor in three fields: one is steady and uniform, another one is non-uniform and steady in the stator frame of reference and the

last one is steady and non-uniform in the rotor frame of reference [23]. The two steady non-uniform fields are due to the lift force generated by the stator and the rotor blades, respectively. The relative motion makes the stator TE experience an unsteady pressure because of the rotor non-uniform field. Likewise, the rotor TE experiences an unsteady pressure because of the stator non-uniform field. This potential interaction is purely inviscid and not related to turbulent fluctuations. Conversely, it depends on M and exponentially decays with the pitch length-scale and not on that of the chord [24]. By considering LPTs, M is low, and the axial distances between consecutive rows are large (typically from 25% up to 60% of the axial chord). Besides, the potential disturbance decay is quite fast: the field propagates upstream and downstream up to a distance, which is equal to the pitch of the considered row. The fluctuations in pressure gradient are generally weak, even if it is worth noting that small changes in static pressure may drastically alter the behavior of inflectional and separated boundary layers. Generally speaking, the potential interaction effect is less relevant than that concerning the wake-blade interaction, as the former is not associated with turbulent fluctuations that affect the transition mechanism [25].

Stream-wise vortices. The tip leakage and the secondary flows generate vortices, which propagate downstream in the main direction of the flow altering the velocity field. As a consequence, they modify the interaction with the following row and, in particular, the pressure field. Although the entropy generation related to the leakage flow is mostly due to the high level of mixing with the main flow, it is also caused by the mixing that occurs within the clearance. Indeed, this phenomenon induces flow angle variations. Even though some

authors [15], [26] stated that the mixing loss mostly depends on the difference in swirl velocity between leakage and main flow, Wallis et al. [27] pointed out that the reduction in relative swirl velocity leads to an increased amount of loss. This contrast shows the importance of unsteady interactions between tip leakage and main flow, and the necessity to delve into this subject [28]. Furthermore, the size and location of secondary flows significantly vary as the leakage flow interacts with the endwall boundary layers [26], [29], which have a key role for the secondary flow development. The stream-wise vorticity may also impact on mixing loss within the blade passage. Since the blade potential field near the LE induces the compression of entering vortices, its velocity deficit diminishes as well as the entropy production rate due to the mixing. Conversely, deformations experienced by incoming vortices within the passage improve the amount of mixing loss [30].

Clocking. The axial and tangential relative positions of rotors severely affect both the potential field and the wake distribution within turbines. The term clocking means that the blade position in the circumferential direction of homologous rows is designed to maximize the beneficial unsteady effects caused by row relative motion. In details, the design target is the alignment of rotor [stator] blade LEs and the upstream rotor [stator] wakes as the efficiency diminishes when wakes enter a row in the middle of the vane [31]. Indeed, the maximum aerodynamic effect is gained when consecutive rotor [stator] rows have the same blade count, while no clocking benefits are detected when the blade count ratio is far from unity [32]. However, turbomachines seldom have consecutive homologous rows with the same blade count as disciplines like aero-acoustics and aero-mechanics impose different design constraints.

After the description of physical phenomena, the explanation of unsteady features is reported to understand their effects on the flow-field.

From a physical point of view, the complexity of unsteady problems noticeably increases with respect to steady ones since the total enthalpy along a streamline does not remain constant. As a consequence, the relations between blade loading and incoming flow angles, which are valid in steady cases, are not so in unsteady ones. Besides, the possibility to neglect compressible effects does not depend on M only [33]. However, the overall effect due to the flow unsteadiness can be analyzed via the inviscid incompressible fluid dynamics since viscous stress, compressibility and heat transfer interact with the unsteady phenomena modifying the magnitude, but not the physical features [34].

An important characteristic of unsteady flows, referred to as energy separation [14], is the exchange of energy with the mean flow. It may be analytically explained by considering the first law of thermodynamics for an adiabatic, inviscid flow without body forces. It may be written as

$$\frac{Dh_0}{Dt} = \frac{1}{\rho}\frac{\partial p}{\partial t} \qquad 2.9$$

As a result, the unsteady phenomena are the only mechanisms able to modify the total enthalpy of a fluid element. In particular, the total enthalpy of a particle varies if the local static pressure of the fluid fluctuates in time.

In addition, any variations in stagnation enthalpy (or stagnation temperature) may cause comparable variations in stagnation pressure without altering the thermodynamic loss [35], since the

second law of thermodynamics relates changes in total pressure and total enthalpy by

$$T_0 ds = dh_0 - \frac{1}{\rho_0} dp_0 \tag{2.10}$$

The equations above show the relation between static pressure fluctuations in time (which are typical of unsteady flows), total temperature, total enthalpy and total pressure [36]. It is worth noting that for incompressible flows, the relation between the variations in time of total and static pressure may be written by manipulating equation 2.9 as

$$\frac{Dp_0}{Dt} = \frac{\partial p}{\partial t} \tag{2.11}$$

Furthermore, by considering a turbine rotor in the relative frame of reference, the static pressure diminishes moving from the pressure side to the suction side. Conversely, in the absolute frame of reference, the pressure changes over time: the fluid particles flow through the rotor passage and undergo a reduction in static pressure and thus in total enthalpy.

$$\frac{1}{\rho}\frac{\partial p}{\partial t}\bigg|_{abs} = -\omega r \frac{1}{\rho}\frac{\partial p}{\partial y}\bigg|_{rel} \tag{2.12}$$

Stagnation pressure and enthalpy changes in unsteady isentropic flows can be explained with the parallelism between static pressure and body force potential. The time-derivative of static pressure $\partial p/\partial t$ acts as an unsteady force potential, and therefore it produces the same effect of any body-force potentials in particle mechanics: any changes in force potential translates into changes in the mechanical energy of the system. Furthermore, if the main unsteady effect is generated by the translation at a constant speed of spatial nonuniformities, such

a disturbance can be considered periodic. Consequently, flow quantities only depend on the tangential position and the product of translational velocity, radius and time. That is the case of turbomachines, where the main source of unsteadiness is the relative motion between successive rows, at least for subsonic M [37], [38]. As a consequence, for each blade radius, the rotor translational velocity multiplied by the component of the pressure force per unit mass in the translational direction gives the magnitude of power exchange per unit mass [34].

Another feature of unsteady flows concerns the variation of the time-averaged total pressure. By writing the velocity like the sum of its time mean value plus its fluctuating component, the momentum equation for incompressible inviscid fluids becomes:

$$\frac{\partial v'}{\partial t} - (\bar{v} + v') \times (\bar{\omega} \times \omega') = \frac{\overline{\nabla p_0}}{\rho} \qquad 2.13$$

By applying the time-average and assuming the mean flow irrotational:

$$\overline{v' \times \omega'} = \frac{\overline{\nabla p_0}}{\rho} \qquad 2.14$$

As a result, time-averaged gradients in total pressure due to flow fluctuations occur only if the unsteady velocity field is rotational. Indeed, many unsteady phenomena existing within turbomachines are associated with vortical flow structures.

In brief, these two features of unsteady flows imply that the unsteady static pressure field associated with total enthalpy variation is due to some type of vortical structures [33].

It is worth noting that steady flows show a remarkable sensitivity to the disturbances due to flow instability. For example, the unsteady perturbations may induce a non-linear response that causes the mean flow to change. More in details, in LPTs the amplitude of velocity fluctuations is one order of magnitude lower than that of the mean velocity. Such intensity is not able to significantly perturb an attached boundary layer [39], [40] since non-linear effects become relevant for oscillations with amplitudes of more than 30%. However, a much lower intensity of freestream fluctuations is able to promote the transitional non-linear response of a laminar boundary layer.

Moving from the description of unsteady flow features to the characterization of a flow, the introduction of a parameter to measure its level of unsteadiness is fundamental. The key parameter is referred to as Strouhal number (St) and may be defined in case of periodic vibrations with a predominant frequency f by:

$$St = fL/U_{ref} \tag{2.15}$$

In the turbomachinery field, the Strouhal number is equivalent to the reduced frequency ($\bar{f}$), that is the ratio between the convection time and the disturbance one. The former is the time it takes for a particle to convect through the considered volume while the latter is the time in which flow quantities locally undergo significant variations [25]. A close approximation of the $\bar{f}$ for LPTs is given by the ratio between the time it takes for a particle to convect through the considered vane and the upstream blade passing frequency. As a consequence, $\bar{f}$ may be defined by [41]:

$$\bar{f} \sim f \frac{C_x}{c_x} = \frac{u}{g} \frac{C_x}{c_x} \tag{2.16}$$

Moreover, $\bar{f}$ is about equal to the square of the ratio of boundary layer thickness (δ) against the viscous layer (δ_v). As $\bar{f}$ considers the time that unsteady disturbances with frequency f take to propagate through a viscous layer, it quantifies the magnitude of unsteady effects.

$$(\frac{\delta}{\delta_v})^2 \sim f\ \frac{C_x}{c_x} \qquad 2.17$$

Therefore, it is proved that $\bar{f}$ not only considers the convective unsteady effects but also the viscous ones. However, $\bar{f}$ does not quantify these effects. Rather, it expresses the relation between steady and unsteady phenomena in a flow. More specifically, if $\bar{f}$ is much higher than unity, the unsteady effects are predominant. If it is about one, the unsteady and quasi-steady effects are of the same entity. Finally, if it is much lower than unity, the flow is quasi-steady.

Furthermore, $\bar{f}$ is related to the number of wakes per vane at each instant: the higher the value, the higher the number of wakes. That aspect is observable in Figure 2.2, which shows the close relation between $\bar{f}$ and ϕ expressed as

$$\bar{f} \sim \frac{1}{\phi}\frac{C_x}{g} \qquad 2.18$$

From the physics point of view, without changing $\bar{f}$, the incidence of incoming wakes in the stationary frame of reference increases as ϕ diminishes.

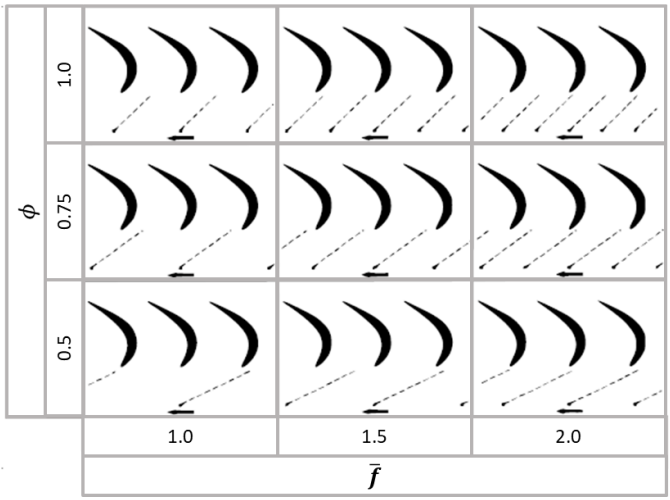

Figure 2.2: $\bar{f}$ and ϕ impact on blade wakes [24]

Clearly, the variation of the incidence determines remarkable effects on blade loading and aerodynamic performance since the boundary layer state results to be affected.

Moreover, as already mentioned in the frame of the unsteady loss (paragraph 2.1.1), $\bar{f}$ together with ϕ significantly affect the wake flow path and drive the wake-merging mechanism: as ϕ diminishes and $\bar{f}$ simultaneously increases, the entropy generation decreases [20].

2.3 Transition

The laminar-to-turbulent transition has been defined by Emmons [42] as a stochastic, three-dimensional, unsteady phenomenon that occurs over a region where laminar and turbulent flows coexist. Therefore, the concept of intermittency has been introduced to quantitively analyze that mechanism: it is the fraction of time in which the flow is turbulent at a considered point of a volume. The intermittency can be evaluated through two quantities: the transition onset position and the spot production rate. Then, they are sufficient to predict the transition phenomenon impact on the flow-field. More in details, the transition onset depends on the freestream Tu and the unsteadiness due to wake passage, while the production rate, and thus the transition process length, is mainly controlled by the pressure gradient at the onset, Tu and, if present, the separation. However, the production rate is also affected by other parameters such as the surface roughness and the streamline curvature (Görtler instabilities), the compressibility and the heat transfer, but their impact is generally five to ten times smaller than that of the pressure gradient [43]. From a practical point of view, in the most part of transitional models the occurrence of transition is evaluated via the momentum thickness Reynolds number:

$$Re_\theta = \frac{U\ \theta}{\nu} \tag{2.19}$$

which determines the boundary layer state by using the related integral property.

As mentioned above, several flow characteristics impact on the transition process, which, therefore, involves different physical mechanisms as the flow conditions vary. An historical classification of the transition modes, which may occur in steady environments, has been provided by Mayle [43]:

Natural. Schlichting [44] pointed out the existence of a critical value of Re_θ at which the boundary layer becomes susceptible to disturbances. Through the steps shown in Figure 2.3 (a), two-dimensional instabilities referred to as Tollmien-Schlichting waves develop within the boundary layer. They convect at a speed of about one third of freestream velocity [13] and their amplification leads to the span-wise distortion of the vortices, which, in turn, become three-dimensional and experience large fluctuations. Then, these vortices burst into turbulent spots. In region 4, the boundary layer is alternately laminar and turbulent, and where two spots coalesce, a fully developed, continuously turbulent boundary layer generates. However, the natural mode only occurs for low values of freestream Tu ($<0.5\%$) [45], which are not common in turbomachines.

Bypass. The first stages of natural transition are bypassed, and turbulent spots promptly generate within the boundary layer as the amplitude of forcing disturbances is sufficiently large. Besides, the bypass transition occurs faster than the natural one as the length of the unstable laminar flow is shorter [46]. In other words, the turbulent spot production rate rises as the freestream Tu or the turbulence length scale at the beginning of transition increase. The bypass transition is the most common mode in turbomachines for it occurs at high levels of freestream Tu.

Separated-Flow. In the low-pressure regions of turbomachines, the transition can occur either within the blade boundary layer before its laminar separation or within the free shear layer of the separation bubble (like in Figure 2.3 (b)). In any case, the mechanism turns out to be more sensitive to Tu than to its length scale. Depending on the pressure gradient and Re_θ, the process may involve Tollmien-Schlichting instabilities or bypass them. Besides, Hatman and Wang [47], [48], [49], [50] introduced a sub-classification of the separated-flow transition mode, which is based on the relative position of the transition onset and the point of laminar separation:

Transitional separation mode ($Re_\theta > 320$). The transition starts before the point of laminar separation. In the attached boundary layer Tollmien-Schlichting waves may develop whereas Kelvin-Helmotz instabilities originate and grow in the free shear layer downstream of the point of separation. The Kelvin-Helmotz waves periodically pair up and grow so that a vortex shedding process occurs, which, in turn, interacts with the transitional free-shear layer and promotes the flow reattachment [25].

Laminar separation mode. The transition onset is downstream of the point of laminar separation. When Tollmien-Schlichting waves develop before separation, they interact with the separated shear layer. As the damping effect of a free shear layer is much lower than that of an attached boundary layer [48], the transition length is shorter for separated flows.

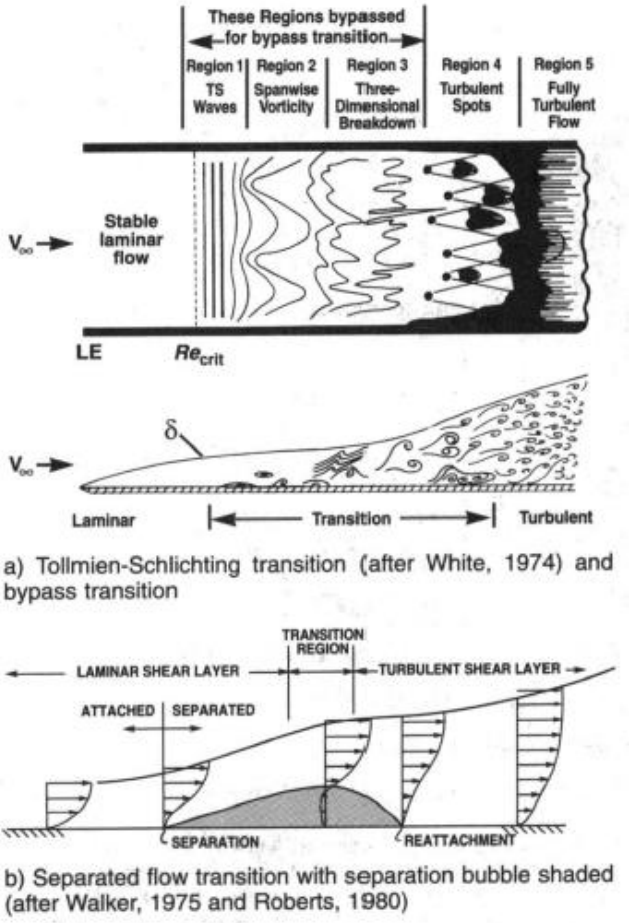

Figure 2.3: **Transition modes** [13]

Since different types of separations exist and their impact on performance is completely different, a clarification is necessary. The most common classification of separation bubbles depends

on the length of their unstable free shear layer [43], and thus they are referred to as short or long. The former type does not alter the pressure distribution far from itself. Indeed, short bubbles only produce a local displacement effect to overcome the adverse pressure gradient. Since they are connected to a phenomenon of vortex shedding, short bubbles are unsteady flow features: two counterrotating vortices exist within the bubble and a third one periodically generates between them so that the two structures located more downstream are ejected. As a consequence, a fourth vortex develops within the bubble to balance the single structure that is still there. In light of this, the laminar shear layer of short bubbles is highly unstable and promotes the formation of turbulent spots. Moreover, high values of freestream Tu lead to an early transition onset and the separation bubble becomes shorter and thinner. However, the extent of the reattachment process becomes greater since the breakdown occurs within a larger stream-wise distance [51]. When the fluid reattaches, the boundary layer may be either fully turbulent or in the late stages of the transition process; therefore, the profile loss is determined by a competing effect between the bubble length and turbulent wetted surface downstream of the reattachment [52].

On the other hand, long bubbles alter the pressure distribution over the whole blade and cause a dramatic increase in losses. The length of the separation bubble is closely related to the pressure gradient and Re_θ. Indeed, if the adverse pressure gradient is mild and Re_θ is in the range between 240 and 320, the bubble is short, and the free shear layer reattachment is guaranteed by the vortex shedding process. Conversely, when the adverse pressure gradient is strong and Re_θ is lower than 240, the shear layer reattachment cannot occur, and the separation bubble is long [25].

The explanation of transitional modes under steady conditions may be completed by analyzing the origin of the disturbances that trigger the transition process itself. Indeed, under different conditions, the generated flow structures significantly change as well as the interactions that occur between them. A schematic of the various routes of the laminar-to-turbulent transition process is reported in Figure 2.4. Within a laminar boundary layer, flow fluctuations may originate due to inherent instabilities of the boundary layer itself. Alternatively, they are due to induced disturbances, which are determined by external sources. If these fluctuations develop, they may trigger the transition process. More in details, above a critical Re_θ, a laminar boundary layer becomes inherently unstable and may select and amplify some disturbance frequencies, whose exponential amplification rate leads the most amplified mode to be dominant over the others. This mechanism of selective amplification may be associated with either viscous or inviscid instabilities of the boundary layer [53], [54].

At low freestream Tu, the transition process occurs in the natural mode for attached flows: freestream disturbances are selected and amplified so that Tollmien-Schlichting waves generate within the boundary layer. The development of these two-dimensional waves leads to the formation of three-dimensional secondary and tertiary instabilities. When the pressure gradient is adverse, velocity profiles in the attached boundary layer may become inflectional, and the separated shear layer shows inviscid instabilities [55]. They are of Kelvin-Helmotz type and perturb the outer part of the separated shear layer. Differently, viscous instabilities act within the reverse-flow region near the wall. As far as separation bubbles are concerned, inviscid instabilities, which are convective in nature, are predominant. Downstream of the separation, Kelvin-

Helmotz structures develop and cause the separated shear-layer to roll up into coherent full-span vortices. Between two consecutive vortices, the presence of smaller vortical scales proves the inception of breakdown to turbulence that quickly occurs within a short stream-wise distance. The coherent structures are stretched and distorted during the transition and reattachment processes so that they result in hairpin-like vortices [51]. To summarize, at low freestream Tu, the transition process may be driven by the disturbances that convect from the upstream boundary layer, by the instabilities of the separated shear layer or by interactions of the two [56].

At high freestream Tu, external disturbances may induce the formation of stream-wise streaky structures, referred to as Klebanoff streaks, near the LE where the boundary layer is thinner. Indeed, the receptivity depends on the ratio between the boundary layer thickness and the freestream instability wavelength. When the latter is much larger than the former, the receptivity is high [57]. In this receptivity process, referred to as shear sheltering (label (a) in Figure 2.4), high-frequency disturbances are damped by the boundary layer shear whereas low-frequency disturbances penetrate and are amplified by the mean shear of the boundary layer itself [58]. It is worth noting that the Klebanoff streaks convect slower than the freestream flow within the boundary layer. If Tollmien-Schlichting waves and Klebanoff streaks coexist, they interact and induce transition through the generation and breakdown of Λ-vortices (label (b) in Figure 2.4). When these structures are lifted away from the wall, they experience a local breakdown to turbulence (label (c) in Figure 2.4). Moreover, turbulent spots originate due to the high shear associated with the stream-wise streaks [51]. Finally, Klebanoff streaks may interact with the shear layer, which becomes locally unstable and prevents the generation of

full-span roll-up vortices (label (d) in Figure 2.4). In other words, during the initial receptivity phase of the bypass transition mode, the freestream Tu induces linear disturbances into the laminar boundary layer. While high-frequency wave instabilities decay, linear disturbances may develop under these conditions. Consequently, periodic coherent longitudinal streaks originate and become elongated and more intense in amplitude. The breakdown depends on the development of secondary instabilities (Kelvin-Helmotz structures) that randomly induce the local formation of turbulent spots within the flow. Then, they develop in the stream- and span-wise direction and merge with others until the boundary layer is fully turbulent [59].

After the explanation of the transition mechanisms, a concise focus on the turbulent spot characteristics is necessary to better understand this flow feature. It occurs in all the aforementioned modes and plays a key role in loss generation since it greatly influences the boundary layer state. The schematic of the turbulent spot in Figure 2.5 shows its typical triangular shape [13] and the different velocities, referred to as celerities, of its leading and trailing edges [60]. This difference influences the growth rate of the spot while it travels downstream; however, a self-similar shape is maintained. The turbulent spots also spread in the span-wise direction resulting mostly unaffected by the neighbors. The characteristic properties of the turbulent spot, i.e., the spreading angle and the leading and trailing edge celerities, depend on the local value of the pressure gradient [61], [62]. On the contrary, the celerities are not influenced by the transition mode: values are similar for separated and attached flows [63].

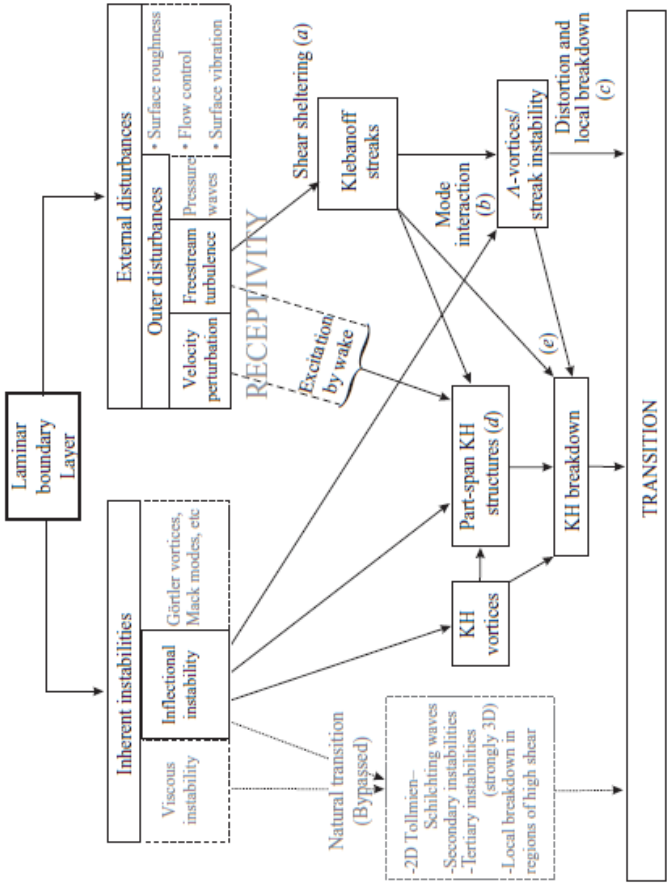

Figure 2.4: Schematic of routes to transition [56]

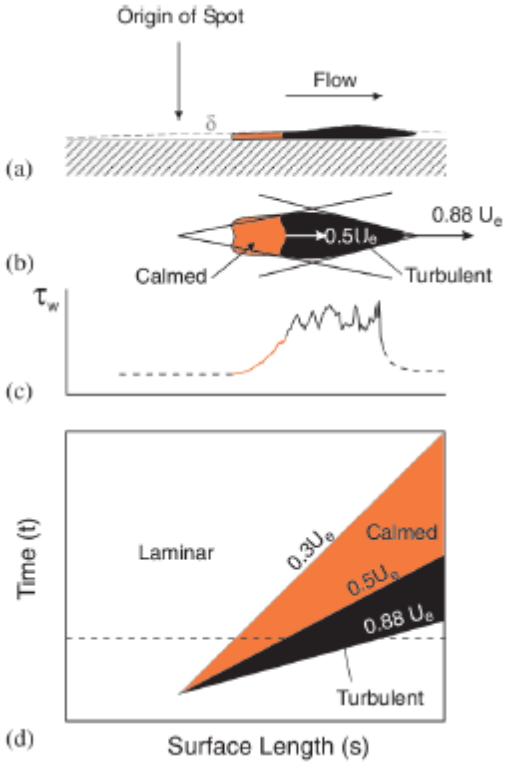

Figure 2.5: Turbulent spot: a) axial view, b) plan form, c) wall shear stress along the centerline of the spot, d) distance-time diagram [60]

Figure 2.5 (b) also shows the presence of the so-called calmed region that generates behind the turbulent spots (and turbulent strips) [60]. It always arises as it does not depend on the occurred transition mode. Indeed, the calmed region may be thought of as a continuous connection in terms of wall shear stress and velocity between the laminar and the turbulent regions (Figure 2.5 (c)).

Furthermore, the calmed region is unreceptive to disturbances, and thus the boundary layer is locally more resistant to transition than the surrounding laminar fluid. The high level of shear stress and the low shape factor (H) also guarantee high resistance to separation. As the velocity of the calmed region is lower than that of the turbulent region, the extension of the former turns out to be wider and wider moving towards the blade TE (Figure 2.5 (d)).

It is worth noting that the arrowhead of turbulent spots may point upstream or downstream: it depends on the breakdown position as the local velocity determines the spot shape. When the breakdown occurs near the wall, the local convection velocity is low and thus the arrowhead points downstream. On the contrary, when the breakdown occurs in the outer part of the boundary layer, where the velocity is higher than that near the wall, the arrowhead points upstream. This is the case of a boundary layer perturbed by freestream disturbances [64].

In conclusion, the turbulent-to-laminar transition exists and is commonly referred to as reverse transition or re-laminarization. It may occur due to external forces, flow curvatures, viscosity or severe accelerations. As a consequence, the stream-wise vortex lines, which are typical of turbulent flows, become stretched. Within the boundary layer, a balance of convection, production, and dissipation of TKE occurs as in the laminar-to-turbulent transition. However, the turbulent production exhibits the opposite sign, and thus the turbulence energy is dissipated or absorbed by the mean flow.

2.4 Secondary Flows

The definitions of secondary flows in literature are various. One very general describes a secondary flow as a flow at the right angle to the primary one [65], where the primary flow (almost) coincides with the pattern under inviscid conditions. Other definitions concern the physics of the issue. A fluid particle turned by a curved surface experiences the deflection of its axis of rotation perpendicularly to the direction of turning. As a consequence, a component of vorticity parallel to the direction of the flow streamlines arises [19]. In other words, when a wall boundary layer within turbomachines is turned by the blade surfaces, the secondary flows are present [66]. Starting from the first schematic of the flow vortex system near the endwall [67], relevant contributions have been provided by many authors that have improved the baseline model by observing additional flow features and interactions among the vortical structures via innovative experimental techniques [68], [69].

Figure 2.6 shows a comprehensive schematic of secondary flows within the passage of a turbine cascade. The pressure gradient at endwall becomes adverse near the blade LE, thus the endwall boundary layer undergoes a three-dimensional separation at the so-called saddle point and rolls up [70]. Consequently, a multi-vortex structure, referred to as horseshoe vortex, generates near the stagnation line [71]. Due to the presence of these vortices, the flow fluctuates and causes the periodic change of the vortex structure itself (Section A-A). Then, the horseshoe vortex splits into two counterrotating legs: the pressure side leg (V_{ph}), which rotates anti-clockwise with respect to the flow direction, and the suction side one (V_{sh}), which rotates clockwise.

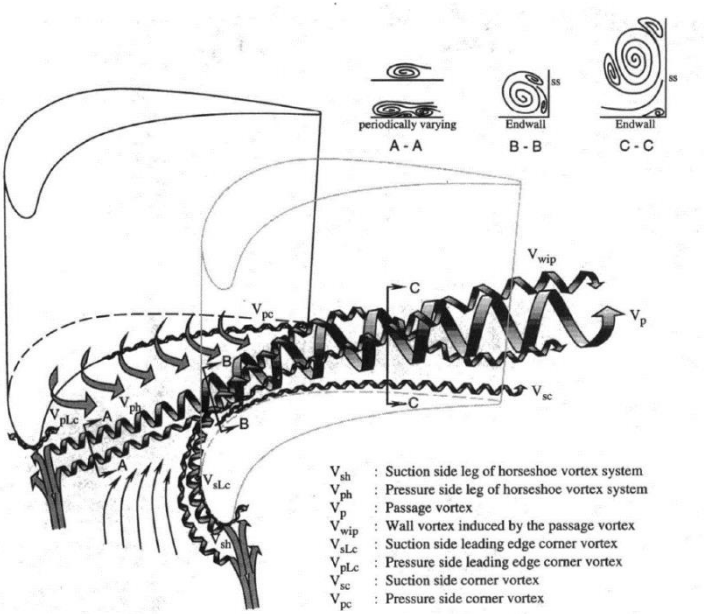

Figure 2.6: Schematic of vortex flow pattern [72]

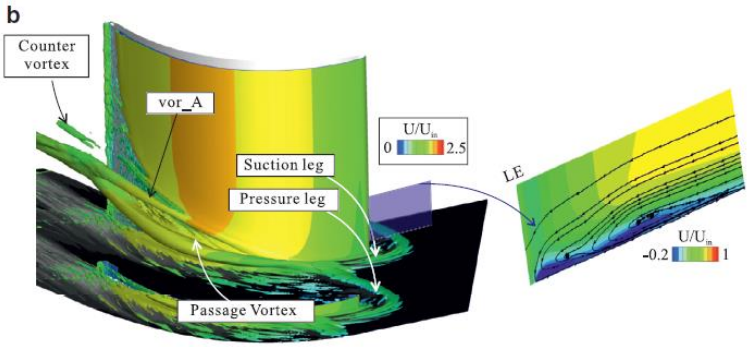

Figure 2.7: Q-criterion isosurface and time-averaged velocity magnitude contours [73]

Within blade passages, the vorticity associated with the inlet boundary layer experiences a quick conversion of its tangential component to the stream-wise one. Besides, the original multi-vortex pattern is progressively replaced by a single-vortex structure. After forming at the saddle point, the V_{sh} travels near the corner between the blade and the endwall. On the other hand, undergoing the tangential pressure gradient within the blade passage, the V_{ph} is pushed towards the suction side of the adjacent blade. Indeed, while the pressure gradient is constant along the span, the velocity at endwall is lower than that at midspan. As a result, streamlines have a shorter radius of curvature at endwall, and thus the fluid convects towards the adjacent blade suction surface instead of flowing parallel to it. Moreover, as the blade loading and the turning increase, an earlier migration of boundary layer fluid towards the suction surface occurs. Likewise, the swirl angle affects the trajectory of fluid particles: the smaller the swirl angle, the earlier the streamlines at endwall reach the suction surface of the adjacent blade. It is worth noting that downstream of the $V_{ph,}$ the boundary layer generates again within the passage and turns out to be laminar regardless of the state of the incoming endwall boundary layer [73]. The V_{ph} may go through two different mechanisms near the blade LE [74]. The flow closest to the endwall undergoes early deflection and develops into vortex legs that cross the blade passage upstream of the passage vortex. Conversely, the boundary layer flow, which is farther from the endwall, entrains low momentum fluid from the newly formed endwall boundary layer while travelling through the blade passage. Therefore, the vortex strengthens and becomes the main secondary flow structure [18]: the aforementioned passage vortex (V_p). It is then apparent that its size is closely related to the momentum thickness of the endwall boundary layer. The V_p

travels downstream close to the suction side and is progressively lifted off the endwall due to the strong tangential crossflow. Besides, the V_p entraining fluid from both the endwall boundary layer and the main flow grows significantly in size. Since it is counterrotating with respect to the V_{sh}, the former not only weakens the latter but also forces it off the endwall. While travelling downstream the V_{sh} may wrap and revolve around the V_p [75]: the relative position at the exit plane is determined by the vorticity magnitude of the two vortices. Alternatively, the V_{sh} may either convect above the V_p [76] and merge with it near the TE (vor_A in Figure 2.7) or may travel downstream remaining close to the corner. Although the V_{ph} and the V_p have the same direction of rotation, if the momentum of the V_{ph} fluid is high enough to withstand that of the V_p fluid, the merging process between the two do not complete. In that case, the V_p turns out to be displaced towards the midspan since it is pushed off the endwall by the V_{ph} [77].

The endwall boundary layer between two consecutive saddle points is forced towards the suction side: a part of it progressively climbs the blade wall along the so-called separation line while the other stays at the corner between blade and endwall. Because of the strong vorticity of local flow structures, especially of the V_p, the boundary layer low-momentum fluid undergoes separation, and then rolls up into many small clockwise rotating vortices: they generate a vortex street referred to as wall vortex (V_{wip}) (Figure 2.6) or concentrated shed vortex (CSV) [78]. After forming close to the corner, it is swept up by the V_p on the blade wall and then travels downstream along the separation line (above the V_p itself). Due to the significant V_{wip} intensity, the blade wall boundary layer is lifted off the suction surface and contributes to feeding the V_p [72]. Alternatively, some authors claim that

the vortex, which counterrotates against the V_p at the TE, is the counter vortex (Figure 2.7). It originates for the interaction between the TE vorticity and that caused by the relative skew of the boundary layer over the suction surface [79]. In addition, small vortices may generate at the corner between the blade and the endwall so that they are referred to as corner vortices (CV). Travelling downstream, they remain close to the blade up to the exit plane. It is worth noting that, whereas corner vortices always originate along the suction and pressure surface, their generation at LE is largely dependent on the local blade shape [80]. Moreover, when the V_{sh} stays at the blade-endwall corner, it interacts and merges with the suction CV. Although the resulting vortex is small, it generates a shear layer between the two counterrotating vortices and balances the V_p in the corner region [81]. The endwall vortices and, above all, the V_p determine a significant difference in terms of momentum and span-wise velocity between the fluid on the suction and that on the pressure side. This gradient induces a shear layer at the TE, which tends to roll up into a clockwise rotating vortex, referred to as trailing shed vortex or as trailing edge wake vortex (TEWV) [82]. The latter connects with the CV and the V_{wip} and generates a large vortex system that counterrotates against the V_p. This interaction induces shear and dissipation that lead to a progressive breakdown of the vortex system back into separate structures [83]. In LPTs, the boundary layer may be separated over the diffusive part of the blade suction side even at midspan. In that case, secondary flows, especially the V_p, may force the low-momentum fluid of the separated boundary layer towards the midspan inducing that fluid to roll up into a sort of tornado vortex. It is called separation vortex, originates above the V_p and then convects downstream rotating with the same direction of it [84].

In light of the mechanisms that drive the generation of endwall flow structures, the key role of the inlet boundary layer is apparent. The vorticity associated with the inlet boundary layer undergoes differential convection within the blade passage, which induce a crossflow velocity and thus the endwall flow structures develop. In other words, secondary flows originate due to the distortion of the inlet vorticity through an inviscid phenomenon [36]. Therefore, the inlet vorticity is the most important parameter for the analysis of such flow structures, while integral parameters of the boundary layer turn out to be inadequate. Indeed, different boundary layers may be equivalent in terms of integral parameters even if their vorticity distribution differs. More in detail, the intensity of secondary flows mainly depends on the vorticity in the near-wall region of the boundary layer: the lower the momentum in the inner part is, the stronger the endwall flow structures are. On the other hand, variations in the outer part of the boundary layer do not significantly affect the development of secondary flows [85]. The inlet conditions also determine the span-wise extent of the inlet boundary layer that interacts with the passage vortex: the lower the momentum thickness, the larger the extent. As a consequence, the span-wise position of the passage vortex core rises as the secondary flow penetration increases [74].

As far as LPTs are concerned, secondary flows affect a portion of blade height of about 20-30% at both the hub and the casing. By considering the lower half of the span, the flow within the passage may be divided into two regions: near the hub the flow is three-dimensional, while near the midspan it may be considered two-dimensional. The flow features, which contribute to the loss generation rate within the blade passage, are the same in both the regions: the dissipation of the mean kinetic

energy due to velocity gradients and the turbulent Reynolds stress.

However, their relative importance locally changes. More in details, they equally contribute to the loss generation rate within the endwall region upstream of the LE. Downstream of it, the situation varies since the interaction between the suction leg of the horseshoe vortex and the suction boundary layer turns out to be not significant in terms of loss production despite the small relative distance. On the other hand, the TKE increases near the endwall downstream of the separation line that is delimited by the horseshoe vortex legs. However, since the pressure gradient is favorable, the TKE growth is moderate up to the suction peak. Besides, the highest values of turbulent production are located at the endwall-blade corner as the passage vortex induces the washing-up of the endwall boundary layer. Indeed, the vortex core is close to the endwall when it reaches the suction side. Travelling downstream, the loss core associated with the passage vortex progressively moves towards the midspan and interacts with the boundary layer at a higher span so that turbulent production peaks locally arise. It is worth noting that upstream of the suction peak the boundary layer is predominantly laminar within the two-dimensional region, thus the mean flow kinetic energy is dissipated by viscous effects, only. Their magnitude even increases in the three-dimensional area since both the blade and the endwall boundary layers contribute to the loss generation. In addition, the local kinetic energy dissipation is also due to turbulent Reynolds stress as the endwall boundary layer undergoes the three-dimensional separation near the LE. However, this effect is less relevant than the viscous one [73]. In the rear part of the blade, losses are closely related to the transition and/or separation occurrence. Indeed, in both the two-dimensional and the three-dimensional

regions, the loss due to the turbulent production sharply increases downstream of the transition point. On the contrary, the loss induced by velocity gradients moderately grows from the leading- up to the trailing edge of the blade. Besides, its peak is lower than that of TKE loss. If the suction boundary layer is separated at midspan like in Figure 2.8, the profile loss significantly grows whereas the loss generation rate starts increasing downstream of the transition point. Conversely, within the three-dimensional flow region, the interaction between the passage vortex and the boundary layer causes high mixing of momentum so that an early transition occurs. As a consequence, the separation bubble length is reduced, and a region (labeled B) of low loss generation rate develops above the passage vortex up to the blade TE. Moreover, the constant washing-up of suction surface boundary layer due to the passage vortex does not permit any local transition (region A) and the loss turns out to be lower. These effects mitigate the growth of kinetic energy dissipation rate due to turbulent Reynolds stress if compared with that in the two-dimensional region. As a result, the dissipation may be stronger in the latter than in the former. However, the overall impact of secondary flows on performance is detrimental [86].

It is worth noting that the state of the inlet boundary layer has a relevant impact on loss generation. However, remarkably differences between the effect of laminar and turbulent boundary layers are not observable within the region of favorable pressure gradient since the interaction between the endwall boundary layer and the suction one is weak. On the contrary, they significantly interact in the rear part of the blade, where the turbulent boundary layer at endwall induces an increase in mixing and loss production with respect to a laminar one. Moreover, the inflow conditions do not induce significant

effects on loss production within the two-dimensional region. Within the three-dimensional region, the loss production due to velocity gradients is moderately affected by the endwall boundary layer state, while it highly impacts on turbulent production [73].

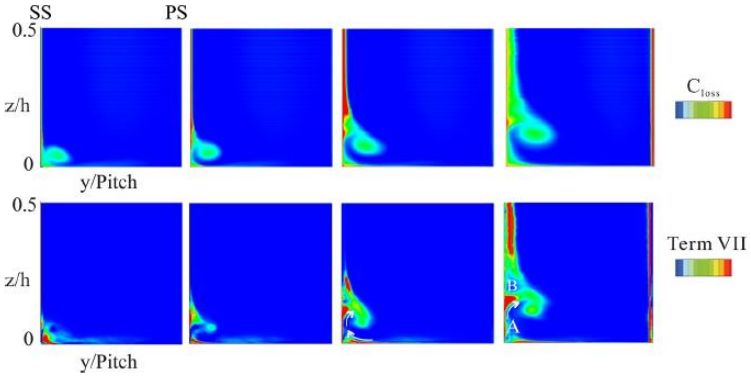

Figure 2.8: Contours of total pressure loss coefficient (top) and deformation work due to turbulent stress (bottom) at different axial postions: 0.5 C_x, 0.65 C_x, 0.8 C_x, T.E. [86]

Downstream of the blade TE, the TKE decreases faster within the two-dimensional region than within the three-dimensional one since the passage vortex mixes out slower than the wake. The kinetic energy dissipation is mainly due to turbulent effects, yet their decay is steeper than that due to viscous effects. In the three-dimensional region, the turbulent production concerns the convection of low momentum fluid from the wake region into the main flow, and consequently the convection of the main flow into the wake region. On the other hand, the turbulent production in the two-dimensional region is due to the presence of the shear layer on the suction side [73]. It is worth noting

that neither the absolute maximum of loss nor the maximum loss associated with the passage vortex coincide with the passage vortex core. The absolute maximum is closer to the counter vortex, while the peak associated with the passage vortex is above the passage vortex core itself [87].

In other words, the passage vortex significantly contributes to the loss within the blade passage, while its impact is lower within the wake. Conversely, the counter vortex, the trailing shed vortex, the separation vortex (if present) and the corner vortex produce a similar amount of loss both within the passage and within the wake [88]. It is worth noting that the mixing process involving wakes and the main flow is unlikely to be complete before the downstream blade row; therefore, it induces a detrimental effect on the performance of following rows [89]. Furthermore, downstream of the TE, secondary flows induce a radial flow angle distortion due to the composition of the tangential velocity component associated with the main flow and the secondary ones, which largely depend on the span-wise position. Indeed, secondary structures not only have different magnitude and different radial penetration depth but also the direction of rotation changes, i.e., the sign of the tangential velocity component varies. In the end, the flow near the endwall turns out to be over-turned, while towards midspan it is under-turned; therefore, the incidence on the downstream blade is increased near the endwall and decreased farther of it. The entity of the induced under-turning is closely linked to secondary flow magnitude: if the latter increases, the former increases as well. On the contrary, the near endwall over-turning is not significantly affected. In other words, the inner part of the inlet boundary layer by determining the vorticity magnitude of the boundary layer itself at the exit plane changes even the impact on the performance of downstream blades. In particular,

a thicker endwall boundary layer at inlet leads to higher vorticity at the exit plane, and consequently the impact on the performance of the downstream blades increases [85].

It is intuitive that all the aforementioned flow structures occur at both hub and casing endwall so that the secondary flows have symmetric pattern with respect to the blade midspan plane. It is essentially true for straight blades in linear cascade rigs without cavities. Differently, flow symmetry is not present in actual LPTs as the pitch and the tangential velocity are not uniform along the span: the velocity magnitude is lower near the casing than close to the hub, and thus the intensity of secondary flows turns out to be smaller near the shroud [81]. Moreover, the three-dimensional shape of blades induces flow migration in radial direction and leakage flows: both the features contribute to the local alteration of the near-endwall flow structures.

In actual LPTs, the endwall flow undergoes other two mechanisms at the inter-blade gap that alter the secondary flow structures: the change of the frame of reference and the external forcing due to the purge flow. The former induces the boundary layer deviation with respect to the main flow and consequently determines negative incidence onto the downstream blade. In other words, secondary flows are reinforced as the stream-wise vorticity increases while crossing the gap between stator and rotor. This effect turns out to be relevant for thick boundary layers, only [15]. The mechanism concerning the purge flow not only increases the boundary layer thickness but also skews the near-endwall flow angle. Indeed, the injection of cavity flow forces the main flow off the endwall and induces blockage effect. Consequently, the main flow velocity increases while the near-endwall momentum and the swirl angle reduce downstream of

the cavity. In light of the considerations reported above, these effects cause stronger secondary flows and consequently the related losses rise. In particular, the detrimental impact of the passage vortex grows and both the induced under-turning and overturning increase. Besides, a high purge flow rate may induce flow separation at endwall that, in turn, increases the TKE and the losses due to the instability of the separated shear layer [86].

2.5 Wake-Blade Interaction

The understanding of the interaction between blade and wake is crucial to successfully design high- and ultra-high-lift blade profiles since the relevance of the aspects concerning unsteadiness, transition and secondary flows dramatically increases. Besides, each of these phenomena is not independent of the others and interacts with them so that the environment complexity greatly rises. For example, the occurrence of large separation bubbles due to the severe diffusion over the last part of the suction side may be prevented due to the interaction between the wakes and the separated boundary layer: the TKE transported by the wakes induce an early transition so that the bubble reattaches earlier. Another example concerns the blade loading increase in the high- and ultra-high-lift concept. It leads to stronger pressure gradients within blade passages that, in turn, cause secondary flows to be more intense. At the same time, the flow structures near the endwall are also affected by the wakes that alter the driving mechanisms of the vortices themselves.

In light of this, the present paragraph analyzes the physical phenomena involved in the interaction between wakes and blades, as well as their impact on aerodynamic performance. In particular, the following subparagraphs further investigate the wake evolution within the blade passage, its impact on the transition process and that on the secondary flows, respectively. However, many transversal aspects are highlighted in the whole paragraph to remark, once again, the complex interactions among all these phenomena within LPTs.

2.5.1 Wake Kinematics

The process of mixing between wakes and the surrounding inviscid flow turns out to be slow despite the remarkable velocity deficit in the wake-relative frame of reference [90]. Thus, the flow entering the downstream blade passage is still affected by the presence of wake segments. In order to describe the effects of wakes on the performance of the downstream blade rows, various models have been proposed in literature.

The schematic of the so-called negative jet model is shown in Figure 2.9: the velocity flow-field is the result of the superimposition of a jet, which represents the wake, onto a uniform freestream flow. For turbines, the direction of jets is negative, i.e., travelling towards the upstream blade row [91]. As a result, within the blade passage, the wake fluid progressively builds up over the suction side while a thin wake leg points upstream and towards the pressure side [92].

In another model, the cross-transport one [93], the stagnation temperature is considered as a convective scalar in unsteady flows. Consequently, its increase near the blade suction side and decrease close to the blade pressure side are of equal magnitude as the wake is a defect in the rotor-relative stagnation temperature. However, more recent measurements [94] collected on traverses placed downstream of the passage exit plane show an opposite trend to that expected from the cross-transport model. Indeed, the stagnation pressure increases over the pressure side and decreases over the suction one with respect to the values at the inlet.

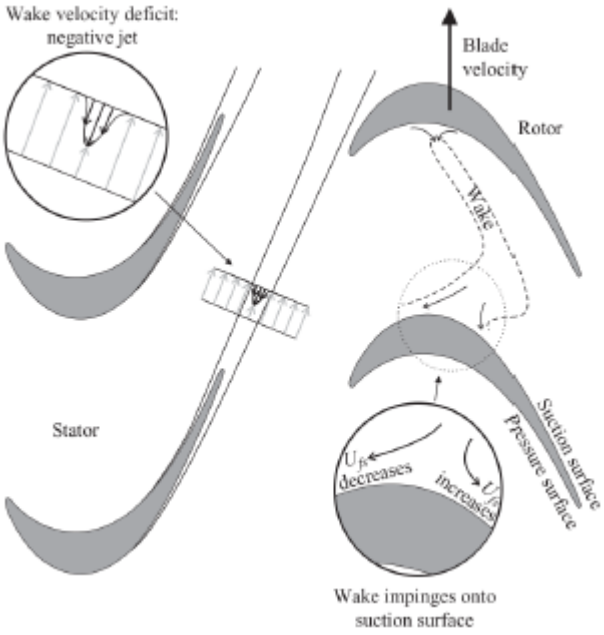

Figure 2.9: Negative jet [96]

The main drawback of the cross-transport model is in the fact that it neglects the effects of fluctuating static pressure on the time-averaged stagnation quantities [95]. In other words, it does not consider the energy separation phenomenon.

The wake transport generates a recirculating velocity field within the vane on each side of the wake, and thus velocity field fluctuations that induce static pressure perturbations. The stagnation quantities convect with the flow, and also the unsteady static pressure partially convects; therefore, some fluid particles are always in contact with regions of positive $\partial p/\partial t$ so that their stagnation quantities increase. On the contrary, other particles are always in regions of negative $\partial p/\partial t$, and thus their stagnation pressure and enthalpy decrease.

This mechanism tends to amplify the fluctuation amplitude and the distribution of peaks and troughs of the stagnation quantities. In some cases, their fluctuations downstream of the blade are larger in amplitude than the wake defect at the inlet. Furthermore, the migration of low total pressure fluid toward the suction side causes an increase in time-averaged entropy on the suction side itself. By contrast, it decreases on the pressure side where the wake fluid is replaced by the freestream one. Basically, the negative jet and the energy separation co-exist. One dominates the other in some unsteady flow-fields and vice-versa [35].

A detailed analysis of the wake kinematics within the blade passage is shown in Figure 2.10. When the wake impinges onto the pressure side near the LE (label A), the velocity of the near-wall fluid decreases in the region located downstream of the wake (C) due to the momentum transport associated with the negative jet. Conversely, the near-wall velocity increases in the region placed behind the wake (D) [97]. Moreover, the wake

approaching the adjacent blade suction side induces blockage effect (B) in the region downstream of the wake front itself. It is worth noting that the crossflow fluctuation due to the negative jet is balanced by the clockwise rotating vortex (F) that originates downstream of the wake. Also, the velocity decreases near the pressure side while increases at the suction side. As a consequence, the velocity of the accelerated fluid near the suction side is further increased (E). On the other hand, the anti-clockwise rotating vortex (G), which generates upstream of the wake, induces the opposite effect: the fluid decelerates near the suction side and accelerates close to the pressure surface. Both the swirling structures strengthen convecting downstream (H, M and K, N, respectively) since the passage geometry induces the flow acceleration. In other words, the negative jet periodically influences the boundary layer width since the induced vortex structures alter the near-wall velocity field. As a result, the boundary layer becomes more inflectional upstream of the wake center and less inflectional behind the wake itself [92]. When the wake impinges onto the adjacent blade suction side, it splits into two separate regions: the jet accelerates the near-wall flow in the region downstream of the wake center and decelerates that in the region upstream of it. In other words, the negative jet induces the generation of the counterrotating large-scale structures that, in turn, interact with the suction boundary layer: the strong shear leads to the generation of small counterrotating vortices close to the wall placed under the large structures. Therefore, while the large vortex downstream of the wake accelerates the fluid near the suction surface, the underlying small one decelerates it in the wall proximity. The opposite occurs behind the wake. More in details, the large-scale counterclockwise vortex causes the shear layer to roll up. Consequently, 3D vortices, which are associated with large size

and high-intensity turbulent small-scale structures, originate within the boundary layer. In between the near-wall counterrotating vortices, both the size and the Tu of the small-scale structures diminish since their generation mechanism changes. Indeed, the near-wall clockwise vortex is caused by the shear between the large-scale counterclockwise vortex and the boundary layer. On the other hand, the small-scale structures upstream of the wake centerline are transported by the wake itself and may be amplified in the wake-blade interaction. The near-wall anti-clockwise vortex induces even lower turbulent activity as the boundary layer relaxes after the wake bulk passage [98].

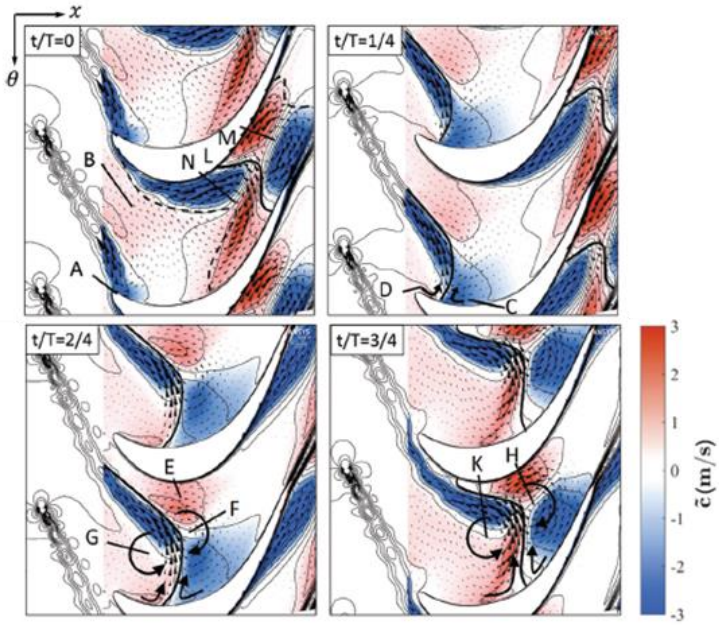

Figure 2.10: Velocity fluctuation contours with projected fluctuation velocity vectors [81]

Finally, it is worth noting that four cells of altered velocity periodically develop within the passage. Their influence is apparent even downstream of the TE, where accelerated and decelerated cells merge with the neighboring homologues that come from the adjacent blade passages. These four cells of low and high total pressure dramatically influence the instantaneous measurement of loss, since they periodically alter the property distribution at the measurement planes [81].

As far as the blade loading is concerned, for a given inlet flow angle, the time-averaged pressure distribution of a blade with incoming wakes differs from that of an undisturbed blade for some small deviations near the LE and the TE. In the former region, the alteration is due to local and periodic fluctuations of the inlet flow angle (up to several degrees) due to the wake velocity defect. The induced negative incidence leads to the flow acceleration on the pressure side and deceleration on the suction one. By contrast, near the TE, the differences are mostly due to the wake impact on the transition process. As a consequence, this effect is more significant in presence of separation bubbles, which may be suppressed by passing wakes [83]. However, the wake distortion mechanism induces periodic effects on the instantaneous pressure distribution. The passage of the four altered-velocity cells locally determines positive and negative loading variations: accelerating cells induce static pressure reduction and vice-versa. In conclusion, the blade loading alteration is observable on both the suction and pressure sides, however, the impact on the former is much more relevant. Finally, this effect significantly rises by increasing $\bar{f}$ as the flow-field cannot return to the unperturbed conditions between successive wakes.

Solid lines in Figure 2.10 highlight the wake centerline. It is apparent that wake segments experience a massive distortion convecting through the passage, and their shape radically change. However, before entering the blade passage, the wakes do not show any distinct vortical structures. Then, the suction side part convects over the blade surface. By contrast, the pressure side one undergoes a velocity field with uniform direction and varying magnitude since it increases away from the blade surface. The resulting stream-wise velocity gradient induces the straining of wake segments, and it occurs with a stronger rate near the suction side. Moreover, the local change of the wake orientation is induced. Indeed, near the suction side, the wake segments are compressed in the wake centerline direction and stretched in the normal one (with respect to the wake centerline itself). Also, the compression along the wake causes the increase of velocity defect and Tu. Conversely, near the pressure side, the wake segments are stretched in the wake centerline direction and compressed in the normal one [99]. The process of wake distortion is historically divided into four successive phases:

Bowing. It is due to the difference of velocity between the mid-passage region and that close to the blade surfaces at row inlet plane. As the wake fluid travels with the local velocity, it is faster in the mid-passage and slower near the blade surfaces. Therefore, the wake experiences a distortion into a bowed shape. The vorticity increases near the bow apex due to the convection.

Reorientation. The wake segment velocity is higher near the suction side than close to the pressure side because of the circulation of the blade. This velocity difference generates a variation of the angle of wake segments.

Elongation. Since the velocity field non-uniformities cause the wake segments to elongate on the pressure side, their width decreases to keep the wake fluid vorticity constant.

Stretching. The wake segments accelerate more near the suction surface than near the pressure one. Thus, the wake width significantly increases on the suction side, whereas the pressure side leg becomes thin and stretched. The stretching of particles parallel to the blade surface induces the reduction of the mean span-wise vorticity.

It is worth noting that the vortex filaments within the wakes do not have any preferred orientation upstream of the blade passage. The stretching mechanism determines the alignment of these filaments with the axis of principal stress, and consequently that component of the vorticity magnitude increases. Undergoing further stretching, the vortex filaments collapse into circular tubes. They are the legs of long hairpin vortices, whose heads are embedded in the wake. Within the freestream flow in the front part of the passage, primary longitudinal vortices are not oriented in the stream-wise direction, but rather in the wake centerline direction. However, the blade turning causes those vortices to move towards the blade surface and determines their alignment with the stream-wise direction [99]. In other words, the wake disturbance induces high-level velocity fluctuations in the pressure side near-wall region, which determine the generation of the primary vortices. After the wake passage, smaller (and less intense) vortices originate at the same span location of the precursor large rotating cells, but closer to the wall. These small vortices rotate with the same direction as the large ones and induce the generation of counter-rotating vortices.

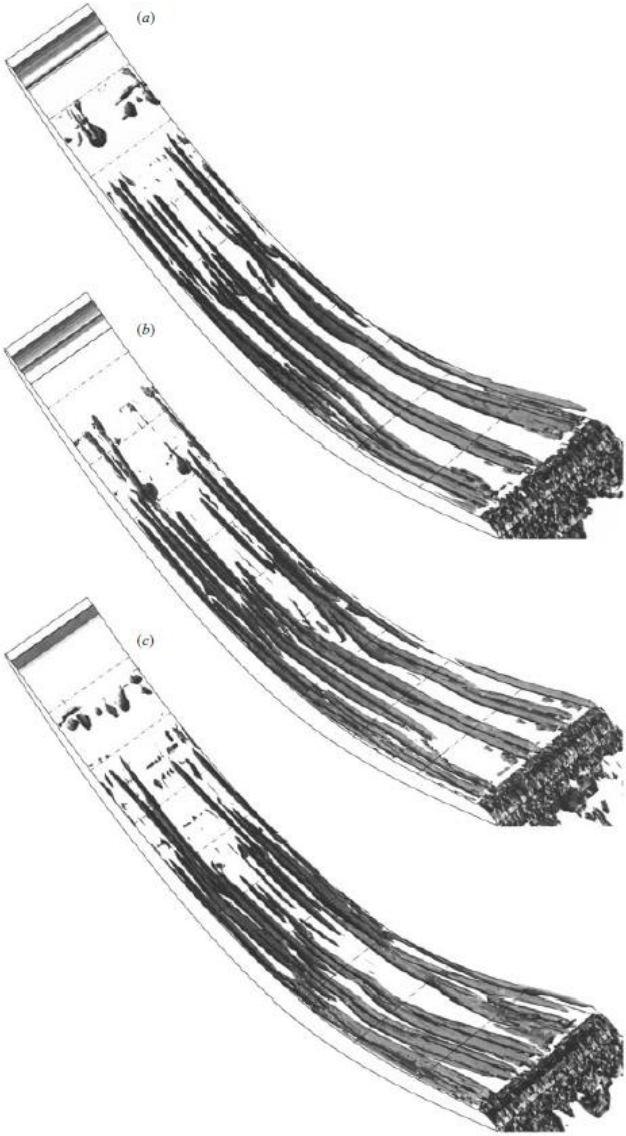

Figure 2.11: Time-accurate representations of the largest negative eigenvalue of $(S^2 + \Omega^2)$ along the pressure side [99]

Then, the vortex pairs move towards the blade surface and force fluid off the wall so that low-speed streaks with a characteristic mushroom shape generate. These "mushrooms" are observable, for example, in the contour plots of the fluctuating stream-wise velocity [100]. The severe deformation that the wake segments experience within the passage changes its relative direction with respect to the blade surface. In addition, two (or more) wake segments may be simultaneously present within one passage. As a consequence, after the velocity peak, the interaction with the near-wall flow significantly increases and the structures introduced above continuously originate and re-organize. Indeed, moving towards the TE, the span-wise fluctuations increase in magnitude and occupy a larger span height. It is worth noting that primary and secondary vortices, as well as their effects, are observable within a distance from the wall equal to about the 3% of the blade axial chord (Figure 2.11).

The mechanisms behind the wake distortion cause turbulence to reduce near the pressure side and close to the forward part of the suction side (Figure 2.12). The TKE peaks labeled F, G and H correspond to the flow accumulation under the centers of the two counter-rotating regions. Indeed, production of TKE occurs where the turbulence extracts work from the mean flow, i.e., where the high turbulent stress confined to the wake encounter high spatial velocity gradients. More specifically, the turbulence production is high where turbulent stress and spatial velocity gradients are aligned. As a consequence, not only the magnitude but also the relative direction and the mean flow strain rate matter.

The turbulence peak within the boundary layer is observable when the wake segment reaches the rear part of the suction side (Figure 2.12 (a), (f))). The interaction between the wakes and

the local inflectional velocity profiles causes the breakdown of vortical structures and triggers the transition to turbulent flow. While turbulence production and TKE levels are low in laminar boundary layers, they noticeably increase in transitional and, above all, in turbulent ones [101].

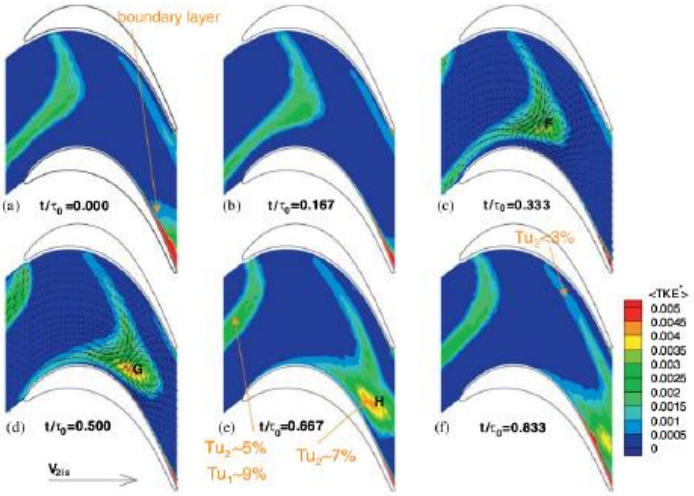

Figure 2.12: Evolution over time of wakes in blade vanes [92]

Basically, by rising $\bar{f}$, the simultaneous presence of more than one wake leads to the reduction of the size of the unperturbed region within the vane. More in details, as $\bar{f}$ increases, the size of the large-scale structures reduces, and consequently, the induced distortions within the passage are smaller. The TKE production due to the large vortices is then reduced. However, wakes also transport small-scale turbulence that determines the increase of the overall TKE production. The related loss

dramatically increases near the suction side where the wake fluid builds up. Finally, the impact of $\bar{f}$ on the TKE production turns out to be remarkable even at the pressure side near the TE [17]. The analysis of the turbulence characteristics shows that the flow is isotropic in the freestream while it is anisotropic in the wake. It is worth noting that the regions of high-level anisotropy coincide with the high-level TKE ones. Moreover, during the wake convection through the blade passage, the anisotropy does not persist, and the flow becomes progressively more and more isotropic [92].

So far, only the interactions between two consecutive rows have been considered. As the LPTs are multi-stage machines, wake disturbances may affect many rows even if the impact is usually relevant on three or four of the following rows. Anyway, the considerations below are necessary to deepen these multi-row interactions. While the stator wakes are stationary in the absolute frame of reference, they are not so in the rotor-relative one. Then, the downstream rotor blades chop them in a segment number that depends on $\bar{f}$. On the other hand, the rotor wakes are stationary in the rotor-relative frame of reference. Therefore, the rotor blades cut the stator wakes in segments that travel in the absolute flow direction, whereas the stator blades chop the rotor wakes in segments that travel in the rotor-relative flow direction. The concept of wake avenues may help to explain the wake segment behavior through consecutive rows [102]. In the relative frame of reference, the segments of rotor 3 follow a well-defined path (Figure 2.13) toward rotor 4. Between stator 4 and rotor 4, the wake segments of rotor 3 are contained in the region limited by the wakes of stator 4. Even if rotor 3 and 4 are stationary in the relative frame of reference, the wake segments coming from rotor 3 are unsteady for rotor 4. It is due to the stator 4 action since it cuts the wakes of rotor 3 (steady in the

relative frame) in periodic wake segments for rotor 4. As consecutive rotors usually have different blade counts, the wake segments enter the downstream row passages at different circumferential positions. Therefore, the pressure field of the downstream row is also influenced by the blade circumferential position of the homologous upstream row. Moreover, the interaction between consecutive homologous rows leads to the modulation of the wake strength. Traces of this phenomenon, referred to as beating, are observable in unsteady data at frequencies equal to the sum and difference of the blade passing frequencies of consecutive rotors (or stators) [103], [104].

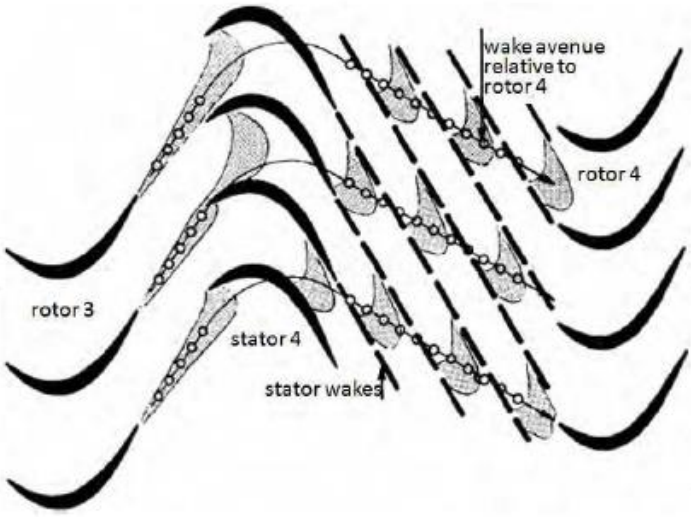

Figure 2.13: Wake avenues [102]

As far as turbulence is concerned, it rises throughout the turbine for the number of wake segments increases moving towards the exit plane. This progressive freestream "filling in" with the high-

TKE fluid contained in the wakes leads to higher overall Tu values: typically, 5-10% in rotor wakes and 3-5% in the freestream of embedded stages. Also, periodic fluctuations in velocity are of the same order of magnitude [105].

To sum-up, the flow complexity rises by moving toward the turbine exit as the number of structures and unsteady interactions significantly increase.

2.5.2 Wake-Induced Transition

The design of LPT blades in steady environments leads to moderate flow deceleration on the rear part of the suction side in order to avoid laminar separation and the related increase of losses. Indeed, in that concept of design, the blade performance is mostly affected by the flow regime: laminar, turbulent, transitional or separated. By contrast, a design process carried out in unsteady setups is largely influenced by the presence of the time-dependent phenomena. Among these, the interaction between wakes and the blade boundary layer is the most relevant. Clearly, this type of setup results to be closer to that of actual LPTs.

As incoming wakes impinge onto the LPT blade surface, the embedded high-level turbulence penetrates into the laminar boundary layer and triggers the laminar-to-turbulent transition [106]. From the physical point of view, this mechanism turns out to be very similar to the bypass transition mode induced by high freestream Tu under steady conditions (paragraph 2.3). Likewise, the characteristics of the turbulent spots, which

originate in the two modes, are almost analogous. Anyway, the wake-induced transition process is mostly dependent on Re [107], [108]. At high values of Re, the laminar separation does not occur. This is the case of blade profiles characterized by low diffusion over the rear part of the suction side as the laminar boundary layer remains attached up to the transition onset. Therefore, wakes periodically trigger the transition of the boundary layer that does not separate even between consecutive wakes. Then, at moderate values of Re, the laminar-to-turbulent transition finishes before the steady laminar separation occurs and it happens only if the deceleration on the suction side is sufficiently high. This is the case of high and ultra-high lift profiles. Finally, at low values of Re, the laminar separation arises upstream of the transition onset so that the latter occurs over the bubble shear layer. Again, the separation occurs only if the pressure gradient over the rear part of the suction side is high enough. It is worth noting that since the pressure gradient is favorable and the Re_θ is low, the boundary layer remains laminar before the suction peak despite the periodic disturbance of wakes and regardless of the value of Re. Conversely, the incoming wakes determine considerable values of Re_θ over the rear part of the suction side. Indeed, the wake-induced transition starts for values higher than 90-150 for standard profiles [109] and higher than 225 for the ultra-high-lift ones.

The remainder of the paragraph further explains the wake-induced transition within the fully attached boundary layers first. Then, the transition mechanism over the separation bubble shear layers is shown.

In the first scenario, the span-wise turbulent spots generated by the interaction between wakes and the boundary layer coalesce into strips, which develop while travelling downstream along the

blade [110], [64]. The trajectory of a strip along the blade maps out the so-called wake-induced path (Figure 2.14). Its first region (labeled B) is characterized by transitional strips, and thus the local intermittency is lower than 1. The value of the intermittency within region B is fundamental as it determines the effectiveness of the calmed region in suppressing flow separation. In other words, the calmed region effectiveness depends on the formation and development of the turbulent spots in the wake-induced path. Besides, the transition onset between consecutive wakes depends on the intermittency within region B. The two regions A and C are fully laminar and fully turbulent, respectively, thus the intermittency of the strips within region C is equal to 1 [13]. Conversely, it is equal to 0 in region A. It is worth noting that both the propagation and the development of a strip are independent of the characteristics of the wake that has generated the turbulent spots which are, in turn, the precursors of the considered strip. Moreover, the transition travels downstream along the blade regardless of the simultaneous occurrence of other transition modes [111]. The extent in time of a wake disturbance depends on $\bar{f}$, which thus affects the time-averaged loss [43]. Between two consecutive wakes, the transition may occur because of disturbances that are not related to the wakes themselves. The latter mode can be generally defined as the non-wake-induced transition. While the wake-induced transition occurs mostly via a bypass mode, a lower level of turbulence is associated with the non-wake-induced transition, and consequently, the transition may occur via any of the processes explained in paragraph 2.3. Actually, several modes are observable along the non-wake-induced path or path between wakes (Figure 2.14) [13]. The wake-induced path and the path between wakes are coupled by the calmed region (labeled D), which develops in the wake-induced path

and decays asymptotically between two consecutive wakes. The two regions E and F are transitional and fully turbulent, respectively.

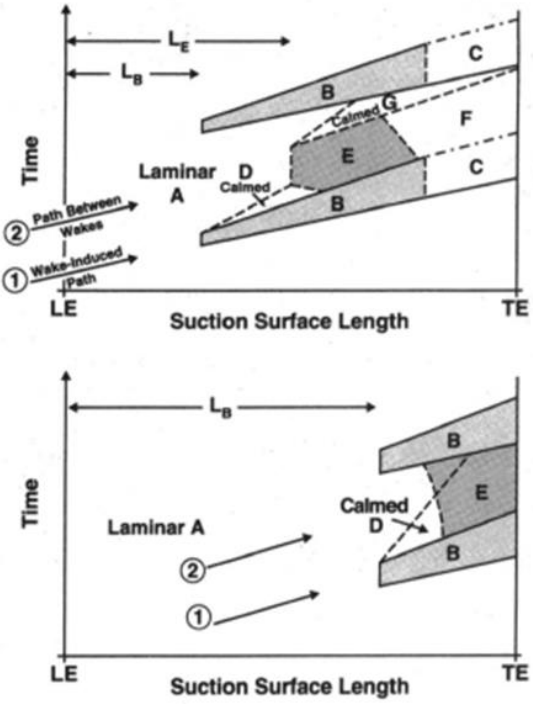

Figure 2.14: Boundary layer development: (a) take-off, (b) cruise [13]

The comparison between Figure 2.14 (a) and (b) shows lower effectiveness of the wake Tu in destabilizing the laminar boundary layer as Re decreases. Indeed, the transitional strips within region B are weaker, and thus the transition onset moves

toward the TE. The size of the calmed region grows as well as that of region E. In brief, a large transitional region develops in the last part of the blade and suppresses the flow separation. Finally, as far as the blade loading is concerned, its increase causes the transition onset to move upstream: its position largely depends on the pressure gradient and the wake Tu. Consequently, the transitional and turbulent regions also occur upstream and occupy a wider surface over the blade.

A schematic concerning the physical mechanism, which occurs in the second scenario, is shown in Figure 2.15: the interaction between a wake, represented by the negative jet, and a separated boundary layer is observable. The solid lines mark the local velocity profiles while the dotted lines denote the separated shear layer. After impinging on the blade, the wake splits into two streams, as explained in paragraph 2.5.1. One causes the flow downstream of the wake centerline to accelerate. The other induces the flow upstream of the wake centerline to decelerate. The outer and inner parts of the boundary layer show a lag in the response to the wake: the inner region responds more slowly due to viscous effects. As a consequence, the wake induces the intensification of the separation shear. When the wake reaches the separation point, the wall-normal velocity component deforms the shear layer, which becomes unstable and triggers the formation of an inviscid Kelvin-Helmotz roll-up vortex embedded in the boundary layer. The roll-up vortex is proved to be a deterministic coherent structure (since it is observable in the ensemble-averaged pressure traces) that moves downstream lower than the wake. Indeed, the latter travels with the same velocity as the freestream. In other words, the wake segments start perturbing the downstream boundary layer before the passage of the roll-up vortex itself [112]. As the wake impinges on the blade near the laminar separation point, large-

amplitude pressure oscillations arise with a peak-to-peak magnitude of about one third of the exit dynamic head [112]. Besides, the roll-up vortices induce the thickening of the boundary layer, then the flow curvature increases, and strong pressure gradients locally occur.

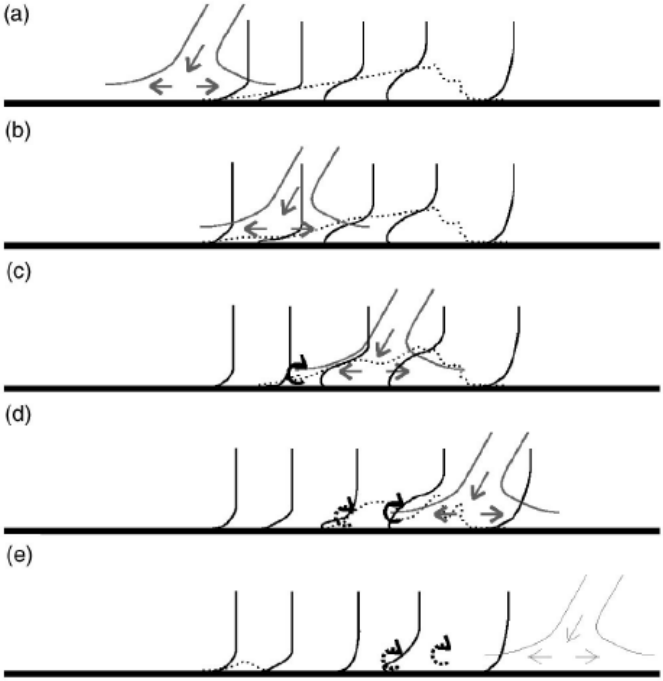

Figure 2.15: Sketch of roll-up mechanism [101]

As far as TKE is concerned, the vortex formation is associated with high values since the near-wall vorticity induces high-velocity gradients. Moreover, the roll-up vortex breakdown to turbulence occurs rapidly and triggers the boundary layer

transition. The calmed region, where the turbulence starts decaying, appears behind the turbulent zone. It is unreceptive to disturbances, and thus suppresses the high-frequency fluctuations due to the boundary layer reattachment. Finally, the boundary layer separates again before the following wake passage. If $\bar{f}$ is low, steady conditions re-establish in the boundary layer behind the roll-up vortices so that other deterministic coherent structures develop due to the natural transition. Indeed, these new coherent structures are characterized by a sinusoidal-like shape and induce pressure oscillations of smaller magnitude and lower frequency: they are typical of Tollmien-Schlichting waves (labeled A in Figure 2.17) [113].

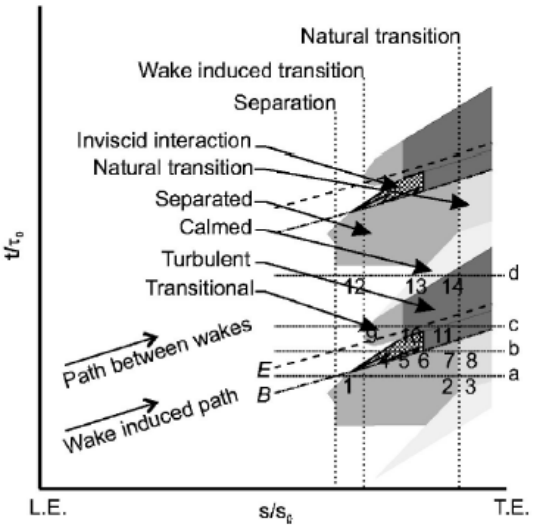

Figure 2.16: Space-time graph of the interaction between the wakes and the suction surface boundary layer [101]

Figure 2.16 shows a schematic of the (second scenario) wake-induced transition mechanism in a space-time graph to compare with the homologue concerning the first scenario. Two paths are still observable: the wake-induced path and the path between wakes. The first differs from the preceding wake-induced path [13] since the wake interacts with a separated boundary layer rather than an attached one.

As explained above, the rolling-up of the separated shear layer into vortices is an inviscid mechanism. As a consequence, it does not occur because the turbulence diffuses into the boundary layer. Conversely, it occurs because the boundary layer immediately responses to the wake disturbance. Only at this point, the wake turbulence diffuses into the attached boundary layer and triggers the bypass transition [101]. It is worth noting that a lift increase induces the bowing of the wake segment, which leads to a greater lag between the inviscid formation of roll-up vortices and the transition induced by the wake turbulence [25]. Moving forward, along the path between wakes there are two regions characterized by a low-level dissipation: the calmed region and a region where the boundary layer starts to separate because of the adverse pressure gradient. This mechanism, which contributes to the loss reduction achieved in high-lift profiles, occurs when both $\bar{f}$ and Re are in a favorable range, which mainly depends on the considered geometry [114].

Figure 2.17 shows the alternation of high and low levels of wall shear stress. In other words, it shows the alternation of turbulent and laminar regions. They are connected by the calmed region, which then decays due to either the passage of the successive wake or the occurrence of the natural transition.

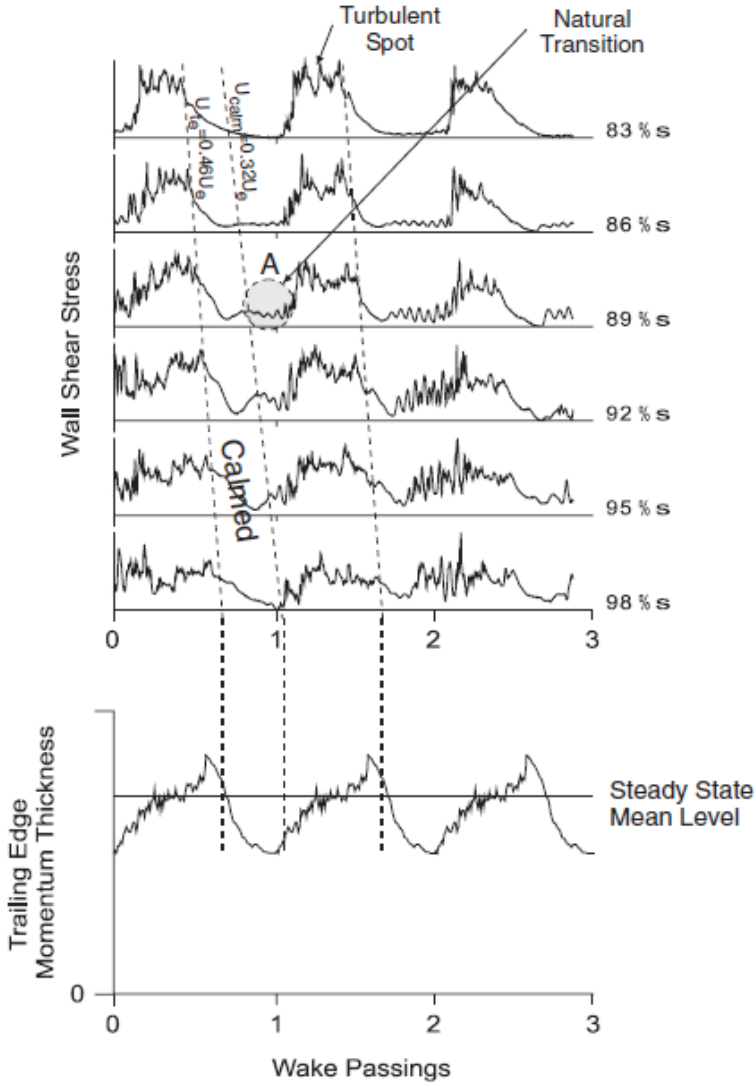

Figure 2.17: Wall shear stress at different suction surface sections and TE momentum thickness [108]

The latter causes a higher viscous dissipation than that occurring in the calmed region because of the energy exchange between the mean flow and the velocity fluctuations [108]. Moving toward the TE, the natural transition is gradually hindered by the calmed region. Indeed, as the latter grows, the bypass transition mode replaces the natural one. When the following wake impinges on the boundary layer, other turbulent spots arise and promote the transition.

The graph of the momentum thickness at the bottom of Figure 2.17 shows a comparison between the momentum thickness at TE under steady and unsteady conditions. The incoming wakes periodically suppress the steady separation bubble, which then starts arising again and causes the momentum thickness to sharply rise. The following wake impinging onto the boundary layer triggers the transition process, and the losses further increase. Anyway, the momentum thickness considerably diminishes within the calmed region so that the overall unsteady loss turns out to be lower than that under steady conditions.

Since the incoming wakes have a high turbulence level, they periodically induce disturbances into the boundary layer and trigger the shear-sheltering receptivity mechanism explained in paragraph 2.3. The mechanism is similar to that concerning the freestream turbulence; however, the wake-generated Klebanoff streaks are characterized by higher vorticity levels and irregular structures (process a, Figure 2.18). Since the wake-amplified streaks convect downstream slower than the freestream flow, they trigger the transition process after the wake passage. It occurs through the generation and breakdown of Λ-vortices (process b and c, Figure 2.18).

It is worth noting that the high momentum thickness associated with the region of wake-amplified Klebanoff streaks significantly

impacts on the LPT performance. Kelvin-Helmotz structures originate (process d, Figure 2.18) before the wake-amplified streaks reach the separation bubble. Therefore, their generation is possibly due to either the weak Klebanoff streaks or the large-scale velocity perturbations induced by the wake. It may also occur because of a combination of the two flow features. Anyway, secondary instabilities induced within the separated shear-layer interact with Kelvin-Helmotz structures so that the formation of full-span vortices like those in the bypass mode is prevented [56].

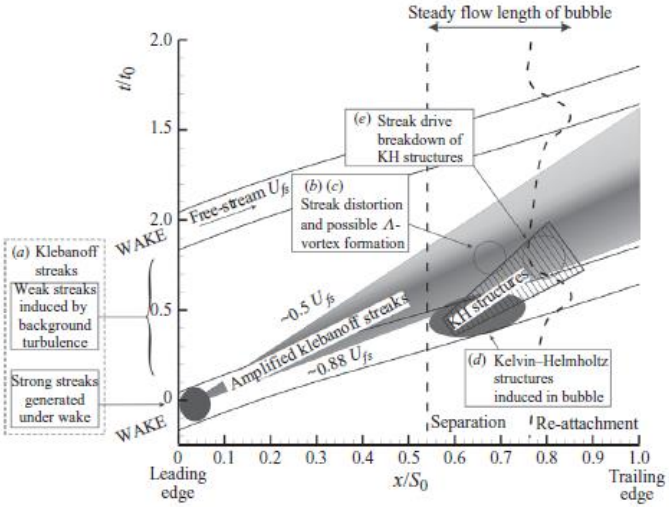

Figure 2.18: Space-time graph of transition process [56]

Wake-generated Klebanoff streaks promote the early reattachment of the separation bubble and determine the Kelvin-Helmotz breakdown to turbulence (process e, Figure

2.18), which usually occurs in the outer part of the boundary layer. In other words, turbulent spots originate since the negative stream-wise fluctuations associated with the inflectional profiles turn to intense forward part-span vortices [64].

The contour plots in Figure 2.19 are useful to deepen the impact of Re and freestream Tu on the wake-induced transition over the separated shear-layer (i.e., second scenario). The dotted lines outline the time-varying locations of separation and reattachment (the latter is also labeled "R"). Besides, the dashed lines mark the time-averaged positions of those mechanisms. It is worth noting that the separation point moves slightly upstream when the wake is approaching, because of the negative jet, which alters the local pressure field [101]. Along the wake trajectory, labeled "W", there are two other markers: "P" and "Q" point the wake centerline and the turbulent patch formation, respectively.

Furthermore, label "C" denotes the separated flow transition, while "K" points the calmed region. Finally, the three lines marked $0.88U_\infty$, $0.5U_\infty$ and $0.3U_\infty$ outline two separate regions: the turbulent strip region and the calmed one, respectively. The Re severely affects the distance between the separation point and the transition onset (Figure 2.19 (a), (b)). High values lead to a faster formation of turbulent patches, and consequently, to smaller separation bubbles due to the early transition [63]. Re also impacts on the pressure oscillation due to the interaction between wakes and the separated shear layer: the higher the Re, the shorter the period of pressure oscillations. On the other hand, the magnitude of those oscillations increases [112].

Moving forward, it is apparent by comparing Figure 2.19 (a) and (c) that the freestream Tu does not severely affect the wake-

induced transition process. Indeed, the edges of the colored contours at high freestream Tu match fairly good with the superimposed dotted line, which denotes the time-varying reattachment at low freestream Tu (they are the same as in Figure 2.19 (a)). In brief, the turbulence within wakes dominates the transition mechanism rather than the freestream Tu level. On the contrary, the freestream turbulence affects the flow behavior between two successive wakes: high freestream Tu promotes an early transition and the formation of turbulent boundary layer [63], [115].

The wake passing frequency does not show any significant effect on both the separation location and the wake-induced transition onset. By contrast, the reattachment position occurs earlier by increasing the wake passing frequency. In other words, the transition process becomes faster as $\bar{f}$ rises [116]. Besides, the boundary layer behavior between two successive wakes changes: high values of $\bar{f}$ prevent the boundary layer from returning to the undisturbed status. Consequently, the separation bubbles are shorter, and the turbulent region grows. Therefore, by varying $\bar{f}$ the amount of loss depends on the net result of these two contrasting mechanisms: the reduction of loss related to the bubble size, and its increase due to the extent of the fully turbulent strip. The effect of the wake passing frequency is even more relevant at low values of Re because separation bubbles tend to be longer and thicker. In addition, at low values of Re, the calmed region is weaker, and thus the damping effect on pressure fluctuations diminishes [63].

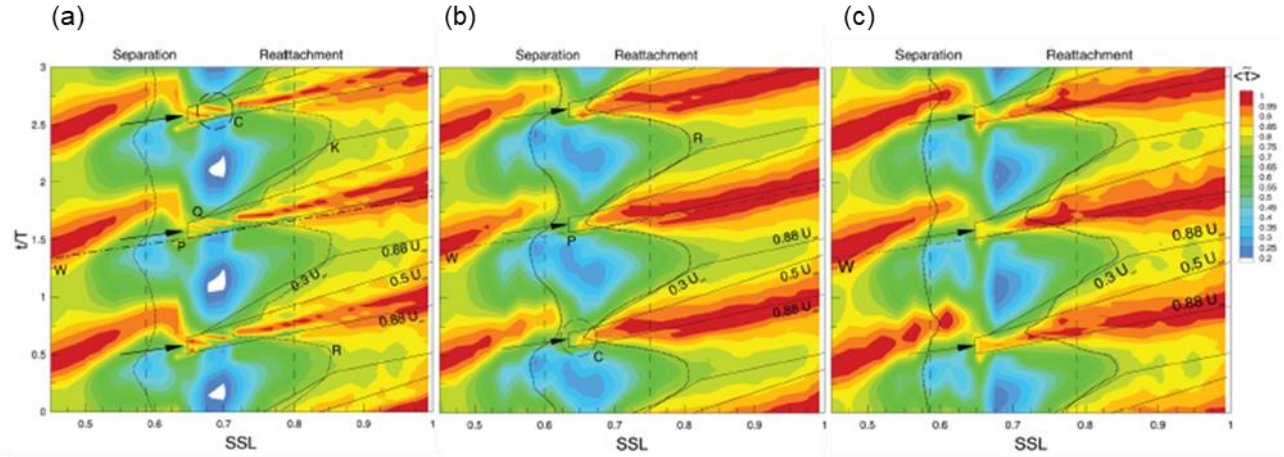

Figure 2.19: s-t diagrams with contours of quasi-wall shear stress at Φ=0.7, f^{+}=1.52: a) Re=50000, fsTu=0.4%, b) Re=100000, fsTu=0.4%, c) Re=50000, fsTu=4% [63]

It is worth noting that the period of pressure oscillations generated by the interaction between wakes and the separated boundary layer does not appreciably change with wake passing frequency, whereas the oscillation magnitude becomes larger as $\bar{f}$ lowers [112].

In conclusion, another phenomenon, which may affect the transition process, is the clocking. For example, the circumferential position of the upstream stator blades (S1) determines the circumferential position of their wake segments that enter the downstream stator blades (S2). The S1 wake segments induce the transition on S2 blade as well as the upstream rotor (R1) wakes. Therefore, the wake-induced transition on S2 blades occurs at twice the R1 blade passing frequency if the S1 wakes segments reach the S2 surface in between two R1 wakes [13].

2.5.3 Wake Effects on Secondary Flows

The incoming wakes, as explained above, may be thought of as periodic flow disturbances entering downstream blade rows. Since the inflow conditions are closely related to the endwall flow generation and development, the wakes induce instantaneous variations of the vortical structures shown in paragraph 2.4. More in details, the wakes continuously alter the intensity and the position of the secondary flows over time, and thus they continuously affect both the over- and the under-turning of the flow downstream of the blade TE [117]. As a consequence, all of the considerations reported below about

vortical structure strengthening and/or displacement must be thought of as time-averaged effects rather than steady ones. In addition, the secondary flow pattern cannot be considered steady since minor vortices may periodically arise, interact with the main structures, and then decay. For example, in linear cascades, the flow angle alteration due to the wake may lead to the formation of an additional vortex close to the endwall. It rotates clockwise and turns out to weaken not only the passage vortex but also the TE and the corner ones.

As the magnitude of unsteady effects depends on $\bar{f}$ and ϕ, they also influence the secondary flows. Indeed, by increasing the wake passing frequency, the intensity of the endwall flows reduces. Besides, for high values of ϕ, the velocity of wakes has a lower tangential component, and thus secondary flows are weaker. However, $\bar{f}$ shows a much stronger impact on both the position and the intensity of the vortical structures [83].

Moving forward, the flow-field analysis is necessary to investigate the physical mechanisms that determine the variation over time of the endwall vortices and are induced by the wake. The turbulence of the latter strengthens the endwall boundary layer that becomes more resistant to separation and deflection. As a consequence, the amount of low-momentum material convected across the blade passage diminishes so that both the passage vortex and the pressure side leg of the horseshoe vortex weaken. Similarly, the wake effect on the suction surface transition determines the alteration of the shed vortex intensity since the width of the blade boundary layer varies [97]. The interaction between wakes and the blade boundary layer also affects the downstream wake width, and, in turn, the non-uniformity of the flow-field entering the following

row. Finally, the alteration of the transition mechanism may also influence the generation of the separation vortex.

The annular geometry dramatically increases the complexity of the present physical problem. First, both the pitch and the circumferential velocity increase by moving towards the casing so that the blade load and velocity triangles change. Likewise, the wake width and the turbulence level increase. Then, radial clearances determine the interaction between the leakage flow and the main flow within the passage. Furthermore, the impact of unsteadiness on the hub endwall boundary layer turns out to be even detrimental in terms of separation suppression, while that on the casing boundary layer is beneficial. The interaction between rotating bars and stationary casing leads to high shear stress, and, in turn, high turbulence in the tip region that strengthens the boundary layer.

On the other hand, the effect of the rotating endwall at the hub is opposite to that of wakes, and the boundary layer turns out to be less stabilized. Therefore, a more detailed analysis of $\bar{f}$ effect is necessary: by increasing it, the span fraction affected by secondary flows becomes smaller at the casing since both the radial mixing and the amount of involved low momentum fluid diminish. As a result, the vortical structures between the endwall and the passage vortex weaken. Likewise, the passage vortex becomes less intense and its core is pushed towards the casing. On the contrary, the corner vortex strengthens. Besides, the loss cores of both the passage vortex and the neighbor counterrotating vortices (CSV + TEWV) merge into a single structure at the casing. Conversely, the effect at the hub is much less significant: the passage vortex is larger yet it turns out to be more diffused. Also, the counterrotating vortex weakening is less intense (Figure 2.20).

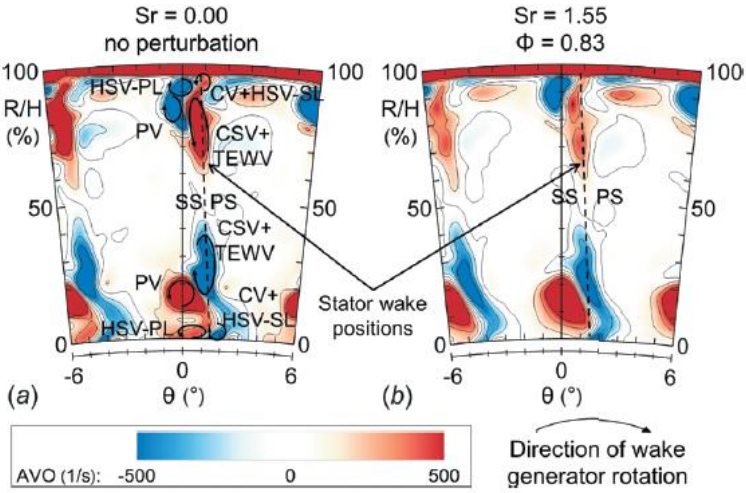

Figure 2.20: Time-averaged axial vorticity contours at 0.15C downstream of blade TE: a) no perturbation, b) incoming bar wakes [97]

The effect over time of wakes on the velocity distribution for the 3D region is analogous to that explained for the 2D region (paragraph 2.5.1). However, the non-uniform distribution of velocity along the span induces a time shift between midspan and near endwall region, where the presence of vortical structures furtherly slow the flow propagation. Moreover, the occurrence of secondary flows close to the suction side determines the local displacement of the two regions of wake-altered velocity. In other words, in the 3D region, the velocity field is distorted by the low-momentum fluid of both the incoming wakes and the vortical structures. Indeed, the passage of accelerated fluid cells induces the periodic weakening of the passage vortex, which later interacts with the decelerated fluid cells and strengthens again. Conversely, the concentrated shed

vortex shows the opposite response to the wake-altered velocity fluid cells. This direct impact of wakes on the endwall vortices is superimposed to the so-called indirect impact, which is the alteration of secondary flows due to the wake effect on their drivers. In particular, the pressure gradient across the blade passage is altered, and the interaction with the endwall boundary layer both upstream and within the blade passage varies. Therefore, the vortex generation is largely affected by the periodic decrease of the crossflow transport. Indeed, the pressure side leg of the horseshoe vortex periodically weakens and impinges on the adjacent blade suction side further downstream, where the passage vortex is affected by the corner separation. As a consequence, the passage vortex and the concentrated shed vortex move back and forth over time in the radial direction. The displacement and intensity variation of secondary flows are more apparent at the hub, where the effects induced by unsteady disturbances are quite slow and gradual. Conversely, the vortex system near the casing shows a more immediate and discontinuous response, especially for the clockwise rotating vortex system, which is composed of the concentrated shed vortex and the TE wake vortex.

In actual LPTs, the wakes are clearly produced by blades, whereas in many low TRL experiments, rotating bars are used to generate periodical inflow disturbances. This difference greatly affects the wake characteristics so that the effects on downstream blades turn out to be altered. One of these differences concerns the lack of secondary flow structures within bar wakes due to the bar geometry itself. Moreover, the blade wakes have a 3D region near the two endwalls and a 2D region near midspan. As explained above, secondary flows formed within the upstream blade are convected downstream and do not completely mix before entering the following passage. As a

consequence, in actual LPTs, the flow distortion due to the wake is not constant along the span. In the 2D region, it introduces high-level turbulence that significantly influences the transition process. It, in turn, alters the loss production over the entire blade suction surface, even though the main effects are concentrated between the peak and the TE. On the other hand, in the 3D region, the vortices coming from the upstream blade enhance the mixing within the blade passage near the endwall so that loss production dramatically increases over the entire suction side length [73]. It is worth noting that the presence of secondary flow structures in incoming wakes increases the flow swirl angle in the near endwall region. Conversely, the purge flow induces the same effect, but with the opposite sign; therefore, the simultaneous presence of wakes and purge flow mitigate the swirl angle distortion due to the former [86].

3 Numerical Methods

The present chapter deals with the numerical tools used throughout the work presented in the thesis. The first paragraph outlines the main features of the adopted CFD code named TRAF (TRAnsonic Flow) that has been developed by the research group of Prof. Andrea Arnone. Besides, the second paragraph introduces the basic concepts of Machine Learning and in particular of Artificial Neural Networks.

3.1 The TRAF Code

The development of the TRAF code started in 1988 in the framework of a joint research project between "Università degli Studi di Firenze" and NASA (ICASE and ICOMP) that was focused on the viscous analysis of internal cascade flows. TRAF is a 3D URANS code that includes several techniques to enhance computational efficiency and accuracy.

The 3D-unsteady Navier-Stokes equations are averaged adopting the Reynolds approach (RANS) and expressed in conservative form for each blade passage: they are expressed with respect to a curvilinear coordinate system ξ, η, ζ. The relation between the Cartesian coordinate system and the curvilinear one is handled through transformation matrices and Jacobian.

Several turbulence closure models ranging from algebraic to two-equation approaches are implemented in the code. The complete list is reported below :

- Baldwin-Lomax algebraic model [118]
- Baldwin-Lomax algebraic model with Degani-Schiff correction [119]
- Mixing length algebraic model [120]
- One-equation Spalart-Allmaras model [121]
- One-equation Spalart-Allmaras model with Spalart-Shur correction [122]
- Two-equation k-ω Wilcox Low-Reynolds model [123]
- Two-equation k-ω Wilcox High-Reynolds model 1988 ver. [123]
- Two-equation k-ω Menter SST model [124]
- Two-equation k-ω Wilcox High-Reynolds model 2006 ver. [125]

As far as the laminar-to-turbulent transition models are concerned, two options are available in the code:

- One-equation Laminar Kinetic Energy (LKE) [126]
- Two-equation γ-$Re_{\theta,t}$ Langtry-Menter [127]

Both the models may be coupled with the two-equation turbulence closure ones. Moreover, they have provided accurate results in the field of LPTs, where the transition mechanism plays a key role, and the accurate prediction of its effects is then crucial [128], [129].

3.1.1 Spatial Discretization

The spatial discretization in the code is based on a finite-volume approach. Besides, the governing equations are discretized in space via an integral formulation and without any intermediate mapping [130], [131], [132]. The viscous terms are discretized using 2nd order accurate central differences. Contrarily, two different options are available for the inviscid fluxes:

- 2nd order cell-centered scheme
- Roe's upwind scheme

In the first case, the fluxes are assessed after computing flow quantities at the face center by averaging the dependent variables of the adjacent cell-center elements. Two models of artificial dissipation are available: scalar [130] and matrix [133]. To minimize the amount of artificial diffusion within shear layers, a specific eigenvalue scaling technique is adopted [134], [135]. Moreover, as the physical diffusion associated with the diffusive terms is generally unable to prevent the potential odd-even point decoupling, which is typical of centered schemes, the artificial dissipation terms are included even far from the shear layer regions. In that way, higher stability is guaranteed and oscillations near shocks or stagnation points are prevented.

In the second model [136], a higher order of spatial accuracy is achieved via a MUSCL (Monotone Upstream-centered Schemes for Conservation Laws) extrapolation scheme (3rd order spatial discretization). It is coupled with a TVD (Total Variation Diminishing) scheme to prevent numerical instabilities [137].

3.1.2 Time-Stepping and Dual-Time-Stepping

In the time-stepping scheme, the system of differential equations is solved in time using an explicit four-stage Runge-Kutta scheme [130]. In particular, a hybrid version of that scheme is implemented to reduce the computational cost. The viscous terms are evaluated only at the first stage and then left unchanged for the remaining stages of the method. Satisfactory high-frequency damping properties are obtained by performing the evaluations of the artificial dissipating terms at the first and second stage. It is worth noting that these damping properties are noticeably relevant for the multigrid process.

For time-accurate simulations, a dual-time stepping method [138], [139] is adopted. Such a name derives from the coexistence of the physical time and a pseudo-time. The derivatives in time (t) of governing equations are discretized via a three-points Backward Difference Formula (BDF). The resulting implicit scheme, which is second-order accurate in time, is linearized by introducing inner iterations to obtain the solution at instant n before calculating that at instant $n+1$. In other words, the unsteady problem is reduced to a steady-state one in the pseudo-time (t^*). In the latter, the time-derivative term is used as a solution-dependent source term; therefore, the solution is evaluated in t^* via the addition of a pseudo-time-derivative term, and iterations are performed to achieve steady conditions. Since the dual-time-stepping scheme does not have any constraint concerning the stability on the Δt size, the latter may be chosen by considering only the time resolution of analyzed unsteady phenomena. In the turbomachinery field, 50-100 Δt per BPF have proven to be sufficient to guarantee a satisfactory accuracy. Moreover, the BDF accuracy may be promptly

assessed for periodic problems, and such a result can be thought of as an approximation of the accuracy for actual problems. By considering a periodic disturbance characterized by a specific wave number (k), the number of time samplings (N) per period (T) may be defined as:

$$N = \frac{T}{\Delta t} = \frac{2\pi}{k\Delta t} \qquad 3.1$$

The deviation between the exact solution and the BDF time-difference-operator turns out to be relevant as N becomes lower than 16. In details, N=16 corresponds to an error of about 5% and 0.5% in the prediction of the real and imaginary components of k, respectively. As a consequence, N must be at least equal to 15÷16 for the highest harmonic that exists in the domain to accurately compute the present unsteady phenomena.

3.1.3 Acceleration Techniques

Four acceleration techniques are implemented within the code to remarkably reduce the computational cost and speed up the solution convergence [140]:

- Local time-stepping
- Residual smoothing
- Multigrid
- Grid refinement

For time-marching approaches, a faster disturbance annihilation can be achieved by locally using the maximum available time step. That limit for the local Δt is computed by:

$$\Delta t = CFL \left(\frac{\Delta t_c \, \Delta t_d}{\Delta t_c + \Delta t_d} \right) \qquad 3.2$$

where both the convective (Δt_c) and diffusive (Δt_d) interval contributions are considered. *CFL* (Courant-Friedrichs-Lewy) number is a constant.

An implicit smoothing of the residuals is adopted to extend the stability limit in terms of maximum CFL value. In addition, that operation enhances the basic scheme robustness. The implementation on the Runge-Kutta stepping scheme for viscous calculations has been proven to be robust and reliable even for highly-stretched computational grids [141], [142], [134], [135].

The concept of the multigrid technique [143], [131], [142] concerns the introduction of coarse grids obtained by removing mesh lines from the finest grid in every coordinate direction. The coarse meshes allow speeding up the propagation of the fine grid corrections so that the disturbance elimination turns out to be faster. The procedure is repeated on a series of coarse grids: the corrections assessed on each coarse grid are transferred back to the finer ones up to the finest mesh through bilinear interpolations. Even if the number of adopted grid levels is arbitrary, the multigrid method is usually carried out via a V-cycle on three grids: coarse ($4h$), medium ($2h$) and fine (h).

The coupling of the multigrid technique together with a grid refinement strategy is commonly referred to as Full Multigrid (FMG) procedure. In particular, at the simulation start, the grid refinement is performed to achieve a cost-effective initialization of the fine grid solution. The solution initialized on the coarsest grid level and iterated for a prescribed number of multigrid cycles is loaded onto a finer grid via bilinear interpolations. That

process is repeated until the finest grid level is not reached. It is worth noting that the convergence level assessment is performed through the check on the residual (R):

$$R = \frac{1}{N} \sum_{n=1}^{N} \left(\sum_{i=1}^{5} R_i^2 \right)^{1/2} \qquad 3.3$$

where $N = nx \times ny \times nz$ is the number of cells of the mesh.

Finally, the convergence target is half-order higher than the machine accuracy in single precision.

3.1.4 Boundary Conditions

The most common types of Boundary Conditions (BCs) used in the turbomachinery field refer to the inlet, outlet, solid walls, periodicity, and the interface between adjacent rows.

Radial distributions of flow angles, total temperature and total pressure may be prescribed at the computational domain inlet while the outgoing Riemann invariant is taken from the interior. At the domain outlet section, either span-wise distributions of static pressure or radial equilibrium may be imposed. The latter is enforced starting from a static pressure value prescribed at the casing. By contrast, density and momentum components are extrapolated. Likewise, the pressure is extrapolated from the interior grid nodes on solid walls whereas no-slip and temperature conditions are used to assess the values for density and total energy. In particular, the adiabatic wall and prescribed

constant wall temperature are the available options for the temperature conditions.

The periodicity in the circumferential direction to model the adjacent blade passages is imposed by setting periodic values for the phantom cells. Indeed, the code has been implemented by adopting one phantom-cell layer for each mesh boundary. If the grids at the tangential boundaries of a blade passage do not match, the dependent variables in phantom cells are set via linear interpolation. Although this approach cannot guarantee complete conservation of mass, momentum and energy, the evaluated reduction in solution accuracy is negligible in most applications. It is not the case for strong gradients occurring along non-periodic grid boundaries where high differences in cell sizes are present.

It is worth noting that the circumferential periodicity may be used even in unsteady analyses. Since the full-annulus approach is very demanding from a computational point of view, the computational domain can be reduced by taking advantage of a geometrical periodicity among rows whenever it exists. For example, if all the considered rows in a simulation had the number 3 as the greatest common divisor, the calculation of one-third of each row would be sufficient to analyze the full-annulus flow-field. Indeed, the latter would be built by rotating the computed solution by a proper angle. Thus, if the angle of the analyzed machine sector measures 360/3=120°, the solutions related to the non-computed sectors would be obtained by rotating the computed one by 120° and 2x120=240°, respectively. Such a strategy involves the adoption of boundary conditions of instantaneous periodicity on the circumferential edges of the computed machine sector. By contrast, at the circumferential interfaces of the blocks within the computed

sector, the exchange of information is performed via linear interpolations in both the tangential and the radial direction.

As far as the interfaces between consecutive rows are concerned, their modelization depends on the type of performed simulation: steady or time-accurate.

For steady simulations, a mixing-plane is introduced to handle the coupling between adjacent rows. The data exchange through the common interface plane is obtained via the calculation of phantom cell values: the span-wise distribution is directly provided while an averaging operation is carried out in the pitch-wise direction. Two mixing-plane models are available in the code: reflective and non-reflective. The first concerns a robust approach: the values related to a phantom cell on one side of the interface are evaluated by averaging in the pitch-wise direction the governing conservative variables of the grid cells at the same span located on the other side of the interface. The interpolation of pitch-wise averaged values is carried out for non-matching interfaces. It is worth noting that this model is able to handle even flow reversals across the interface. However, reflections of the main quantities may occur close to the interface due to the imposition of a constant value for the conservative governing variables along the blade gap for a given span height. These spurious effects may become relevant in presence of short axial gaps between consecutive rows or when shocks occur. Therefore, the non-reflecting model [26], [27], [28] has been implemented to simulate flow-fields where those features may arise.

For unsteady analyses, the coupling between consecutive rows is handled through sliding interface planes. The necessary matching is provided via the use of phantom cell values, which

are evaluated by linearly interpolating the flow variables of overlapped cells.

It is worth noting that all the code features introduced so far are available even for linear geometries. In those cases, the rotational motion of rotor rows is replaced by the translational one, and the cylindrical coordinates are translated into cartesian ones. That setup is used to model LPT linear cascades.

3.1.5 Fluid Models

As far as gases are concerned, two different models have been implemented in the code: the perfect gas and the real one. The latter [144] models a real gas (or a gas mixture or steam) by replacing the analytic relationship concerning the perfect gas with local interpolations of gas data from property tables.

Moreover, the incompressible fluid model is available. The implementation remarkably differs than before since the artificial compressibility method has been implemented. It allows transforming the mixed elliptic/hyperbolic type equations of the unsteady Euler system for incompressible flows into a system of hyperbolic equations in time. The latter can be numerically integrated via the same methods adopted for compressible flows. That advantage concerns the implementation of the artificial compressibility model. Instead, from the numerical point of view, the exclusion of the energy equation from the system of governing equations guarantees a relevant benefit in terms of computational requirements [145].

3.1.6 Parallelization

A multi-level hybrid strategy for parallelization is implemented in the code [146] so that clusters and high-performance computing platforms may be used to perform high-requirement calculations. In details, the hybrid scheme is obtained by coupling the OpenMP and MPI parallelisms. Both strategies can also be used independently.

The shared memory standard OpenMP is an implementation of multithreading: the master thread forks a specified number of slave threads, and the considered task is divided among them. The code has two levels of OpenMP parallelism: the first concerns computational blocks (blade passages) while the second level is nested and involves the span-wise direction of the computational blocks.

Conversely, the Message Passing Interface (MPI) standard has been adopted to handle communications for distributed memory systems. The MPI parallelization allows handling very-large domains by splitting them among different nodes. In that way, even the computational domains associated with memory requirements exceeding the resources of one single node may be simulated.

3.1.7 Computational Grids

The code has been implemented to deal with structured grids of H- and O-types, and they are generated via in-house

developed tools. Examples of blade-to-blade grids of both types are shown in Figure 3.1 and Figure 3.2.

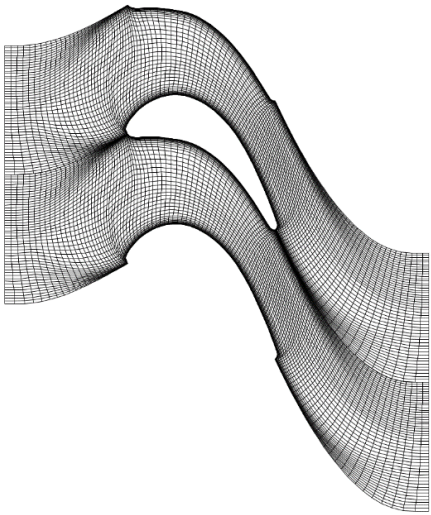

Figure 3.1 Blade-to-blade H-type grid

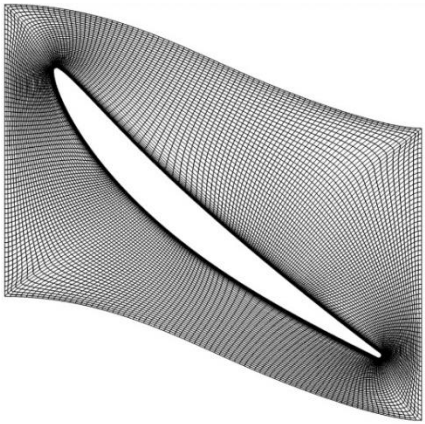

Figure 3.2 Blade-to-blade O-type grid

The 2D meshes are generated via elliptic procedures that solve the discretized Poisson equations using a point relaxation scheme. Specific forcing functions are used to control the grid spacing and the orientation at the wall [147]. Furthermore, viscous grids are generated by introducing additional lines near the wall into the inviscid mesh.

As far as 3D grids are concerned, they are built by stacking 2D grids in the span-wise direction. An example of a 3D H-type mesh is plotted in Figure 3.3.

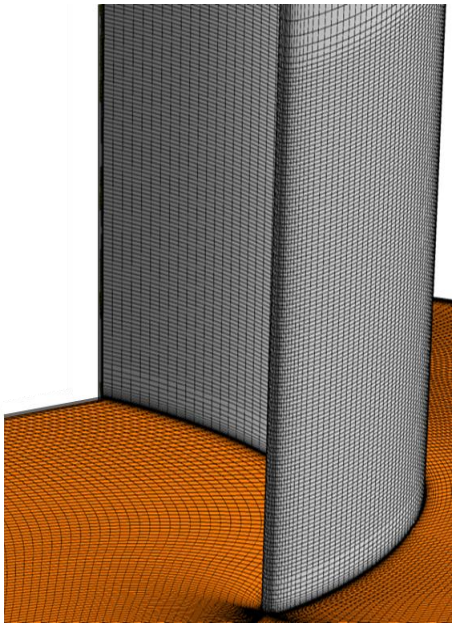

Figure 3.3 Detail of a H-type 3D mesh

3.2 Machine Learning

Machine Learning is a subset of Artificial Intelligence (AI) that concerns computer algorithms that automatically learn and improve through experience [148]. They build mathematical models that are based on the training data and are able to make predictions without being explicitly programmed for any specific task. A macro-classification of machine learning methods based on the algorithm target is shown below:

- Supervised learning algorithm
- Semi-supervised learning algorithm
- Unsupervised learning algorithm
- Reinforcement learning algorithm

The first mathematical model is trained via a dataset that contains both the inputs and the outputs of the considered problem. As the training convergence becomes satisfactory, the algorithm succeeds in predicting the outputs for any new inputs. The prediction efficiency is commonly assessed by testing the model on an independent subset of the database, which has not been used for the training.

Semi-supervised learning algorithms are able to build mathematical models from incomplete datasets, and thus they are generally used when the amount of labeled data is small.

Unsupervised learning algorithms are used to find hidden patterns in datasets in which the outputs are unknown. Such a process is performed by clustering or grouping data points. Indeed, commonalities are found in the data sample, and these aspects allow the classification of new inputs by assessing the presence or absence with respect to the unsupervised dataset.

Finally, the reinforcement algorithms interact with the environment and act to maximize some approaches of cumulative reward.

3.2.1 The Artificial Neural Network

Among the multiple approaches concerning machine learning, the one used throughout the present work is referred to as Artificial Neural Network (ANN). It is a dynamic system based on mathematical models that reproduce the interconnections among elements, which are referred to as "artificial neurons". More in details, they are mathematical constructs inspired by the behavior of biological neurons. Indeed, the inputs and outputs of the artificial units correspond to the dendrites and the axons of a biological one. The action potential, which is the mode a neuron uses to transport electrical signals, is represented by an activation value (commonly a real number). Moreover, the discharge mechanism is modelled through a transfer function that returns unit outputs from the activation values. Finally, the synapses are assimilated to the concept of weight.

The schematic in Figure 3.4 shows the basic unit of the ANN: the artificial neuron, or perceptron. This unit receives some inputs and produces an output. More in detail, a different weight (w_i) is associated with each input $[x_1,x_2,\ldots,x_n]$, and the output (y) is assessed via the activation function (f), which is applied to the weighted sum of inputs:

$$y = f(a) = f\left(\sum_{i=1}^{n} w_i x_i\right) \qquad 3.4$$

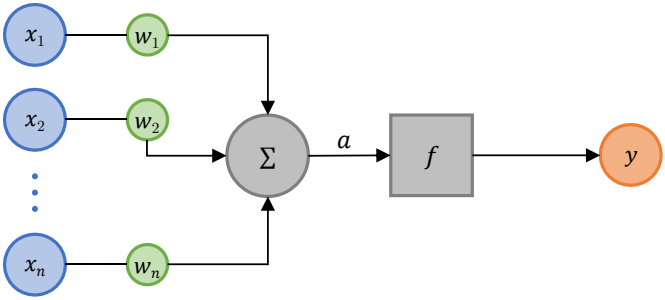

Figure 3.4: Schematic of an artificial neuron

The main types of activation functions are listed below:

Threshold (or binary step). It determines the activation or deactivation of a neuron by comparing a with the adopted threshold. Therefore, a Boolean output is generated.

$$f(a) = \begin{cases} 1\,, & a > b \\ -1\,, & a \leq -b \end{cases} \qquad 3.5$$

where b is the threshold.

Linear. It determines an output signal that is proportional to the input one. In this case, multi-value outputs are allowed.

$$f(a) = \beta a \qquad 3.6$$

where $\beta > 0$ represents the function slope.

Non-Linear. Modern ANNs adopt this type of activation functions since they allow generating complex mappings between inputs and outputs so that complex data may be analyzed. This mathematical formulation allows adopting the backpropagation technique that improves the model prediction accuracy. Indeed, the weights in the input units are iteratively

updated, and the outputs recalculated. Many non-linear functions have been defined to increase the model computational efficiency or suit specific applications. The one adopted in the present work is referred to as:

Sigmoidal function. It is characterized by smooth gradient and normalized outputs. The model prediction proves to be accurate unless input values are too low or too high.

$$f(a) = \frac{1}{1 + e^{(-\sigma a)}} \quad \in (0,1) \qquad 3.7$$

where $\sigma > 0$.

A multitude of basic units generates an ANN that is organized in interconnected layers of neurons: an input layer, an output layer and, possibly, some hidden layers, which are placed in between to improve the model accuracy.

The ANN carries out the forward pass process. The input layer neurons receive the model source data and feed their outputs to the following layer units. In the hidden layers, the units accept the inputs from the previous layer neurons. Then, the former ones transfer their outputs to the neurons of the following layer. Finally, received the inputs from the previous layer units, the output layer neurons generate the outputs that coincide with the model prediction.

The ANN used throughout the present work is based on the feed-forward backpropagation method with two hidden layers. The schematic is reported in Figure 3.5.

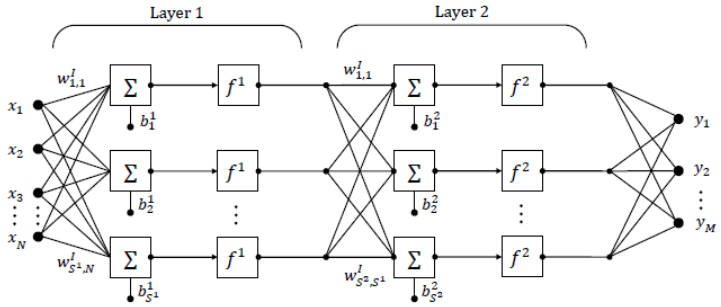

Figure 3.5: Two-layer Artificial Neural Network [149]

The ANN requires a training process to optimize the weights and thus to improve the meta-model prediction accuracy. Therefore, a training set of input quantities, for which the outputs are known, is fed to the ANN. First, the weights are randomly initialized so that the meta-model generates the initial outputs. Then, an error function is assessed by evaluating the least mean squared error between the M outputs provided by the ANN model and the M target values (t_i):

$$e = \frac{1}{2}\sum_{i=1}^{M}(t_i - y_i)^2 \qquad 3.8$$

The backpropagation method allows determining the impact of each weight on the outputs. Indeed, the algorithm can go back from the error function to any neuron and the related weight. In this way, the ANN may iteratively update the weights to minimize the error function.

In particular, at each iteration, the weights are calculated via the equation below:

$$w_{ij(s+1)} = w_{ij(s)} + \Delta w_{ij(s)} \tag{3.9}$$

where

$$\Delta w_{ij(s)} = -\eta \frac{\partial e}{\partial w_{ij}} \tag{3.10}$$

and the parameter η is referred to as learning rate.

The explained process is aimed at minimizing the so-called training error (or bias). However, it does not provide any information about the capability of the ANN to generate accurate outputs for new inputs, i.e., input quantities that are not present in the training set. Therefore, a set of data, which are independent of those of the training set, is used to validate the meta-model. At each iteration, after the weight update, the data of the so-called validation set are fed to the ANN, which provides the corresponding outputs. These are compared to the actual values to assess the validation error (or variance). The predictive model may be considered reliable if both the training and the validation error become lower than a prescribed tolerance value [150].

Figure 3.6 shows two examples of ANN training. In case (a) the process proves to be successful since both the training and the validation errors converge. In other words, the adopted ANN setup, which mainly depends on database size, input/output choice and network structure, provides a reliable model to predict the outputs related to new inputs. By contrast, in case (b) the training error converges while the validation one does not. As a consequence, the model cannot be considered reliable,

and the training process must be performed again after changing the ANN structure parameters. If the latter operation was not sufficient to achieve an accurate ANN model, the database extension by adding new inputs/outputs would be necessary.

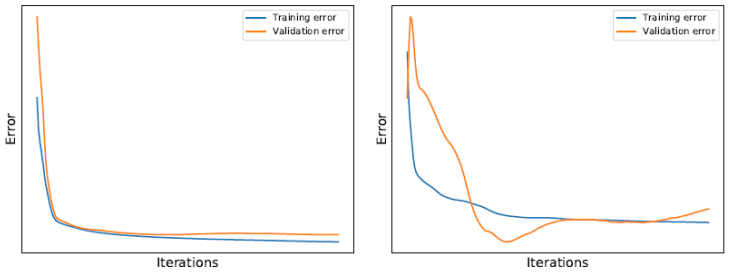

(a) ANN converged errors (b) ANN uncorverged errors

Figure 3.6: Training and validation errors [149]

In light of this, the dimension of the training set plays a key role in the meta-model generation. That dimension is closely related to the design space dimension, which, in turn, depends on the number of design parameters and the admitted variability of each. Indeed, as the design space dimension increases, the number of allowable configurations rises. Simultaneously, the amount of data to effectively sample the design space dramatically rises. Therefore, its dimension must be commensurate to the problem complexity. Besides, the generation of a high-quality training set requires a homogeneous sampling of the design space. To this end, an effective method involves the use of Sobol sequences since they allow generating a quasi-random dataset that prevents sample clustering from occurring.

Figure 3.7 compares the design space samplings obtained via a quasi-random sequence and a fully-random one, respectively. In the latter, many clusters are observable, and, in turn, regions characterized by low sampling occur. By contrast, the plot on the left shows a uniform sampling distribution [149].

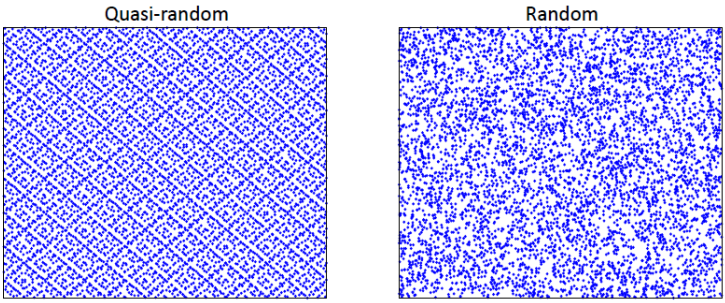

Figure 3.7: Quasi-random and random sequences for design space sampling [149]

4 A Lean Model for Optimizing Airfoils in a Multi-Row Environment

The current standards of aeronautical design are mostly based on steady calculations which usually provide satisfactory results in terms of global performance. However, it cannot happen in some specific applications, like ultra-high-lift blades or off-design operating conditions, since the unsteady effects are relevant and cannot be neglected. Therefore, the design trend concerning shorter and shorter engines with fewer stages and more loaded profiles imposes the consideration of unsteady flows in order to provide accurate results, which are necessary to understand how to improve the engine efficiency and reduce its emissions. Indeed, several studies (for example [108], [107]) have shown that a deeper understanding of unsteady phenomena, in particular the wake-blade interaction, makes new design strategies available.

Anyway, many different design concepts of LPT airfoil have already been investigated in literature to enhance the aerodynamic performance. Some relevant examples are reported below.

First, the concept of laminar profiles was introduced as laminar boundary layers generate a low amount of loss because of the related low-level of skin friction. However, as the diffusion must be limited to prevent flow separation over the rear part of the suction side, the generated lift of each blade turns out to be low.

As a result, many stages with many blades each would be necessary, and the engine weight would severely increase. In conclusion, laminar profiles cannot be adopted in aeronautical LPT turbines.

On the other hand, the increase in blade lift for LPTs allows a reduction in blade count: not only the weight but also the manufacturing cost decreases. Moreover, the lower the number of engine components, the lower the overall risk of failure. With respect to the engine performance, the variation of blade loading is obtained by changing the concept behind the pressure distribution, which is significantly influenced by two parameters: the position of its minimum on the suction side and the diffusion between the peak and the trailing edge [151].

The diffusion over the rear part of the suction side is usually determined via two parameters: the diffusion factor (DF) and the diffusion rate (DR). The first quantifies the entity of the fall in velocity between the peak and the trailing edge suction side.

$$DF = \frac{Ma_{is,MAX} - Ma_{is,TE}}{Ma_{is,TE}} \tag{4.1}$$

The second parameter, instead, evaluates the velocity drop with respect to the length of the diffusive part.

$$DR = \frac{DF}{\frac{(s_{TE} - s_{MAX})}{s_{TE}}} \tag{4.2}$$

The standard approach of LPT design considers a trade-off between the lift increase and loss limitation. In particular, the shape of the front part of the airfoil causes the flow to accelerate so that the boundary layer remains laminar and the loss generation is low. The wall shear stress gradually reduces while

moving towards the suction peak because the boundary layer thickens and, consequently, velocity gradients at the wall become lower. Conversely, between the suction peak and the trailing edge, the flow decelerates and thus the pressure gradient becomes adverse. Since separation may occur under the LPT operating conditions, high-lift blades are designed by adopting the concept of controlled diffusion [152] so that the blade loading increases, and open separations are prevented from occurring. As a consequence, the constraints on diffusion in this frame are less restrictive than those for the laminar design. However, by adopting steady approaches for LPT design, it is not possible to increase the blade loading without increasing losses since the flow separation occurs in the rear part of the profile. If the separation bubble is short, the laminar boundary layer undergoes the transition, and the skin friction losses increase. On the other hand, if the separation bubble does not reattach, the profile is stalled, and the aerodynamic performance dramatically drops. It is worth noting that losses do not linearly increase with the rate of diffusion: they are quite constant over a wide range of low-level diffusion, then they quickly grow as the diffusion further rises. Therefore, if the rate of diffusion is such that the saving in blade counts is worth more than the loss increase, the high-lift design becomes competitive even by considering steady environments [94]. The controlled diffusion determines a relatively large distance between the suction peak and the trailing edge, and thus the accelerating region results to be shorter. In other words, if the DF is kept constant, the DR is lowered in accordance with the controlled diffusion concept. As explained above, a large diffusive region is detrimental for the performance [153], [154].

The understanding of unsteady phenomena in LPT design breaks new grounds since the interaction between wakes and

boundary layer is closely related to the generation of losses. Indeed, incoming wakes may trigger the transition process on the suction side and induce the early reattachment of the separated boundary layer. As the extent of the separation bubble reduces, the blade loading may be significantly increased without incurring profile stall. More in details, to maximize wake beneficial effects, the transition must occur close to the laminar separation point so that the increase in turbulent region size (and in related high-level skin friction) is limited as much as possible [101]. In light of this, the aft-loaded design strategy turns out to be highly beneficial for ultra-high-lift LPTs: the suction peak is pushed toward the trailing edge so that the accelerated region becomes larger and the turbulent one reduces. In addition, it is worth noting that both the high- and the ultra-high-lift LPTs must operate within specific (case-dependent) ranges of wake passing frequency in order to optimize the effect of incoming wakes. Indeed, the gap between two consecutive wakes is crucial to prevent the separation bubble from re-establishing.

A side effect of the lift increase concerns the unguided turning (UGT), or uncovered turning, that is the angle between the tangents at the throat and at the trailing edge and influences the curvature distribution over the blade suction side. As the blade loading rises, high values of the UGT are necessary to maintain a high velocity downstream of the throat. This aspect leads to the generation of a stronger potential field near the trailing edge, which induces the reorganization of streamlines so that the velocity at the trailing edge turns to be lower than that at the row exit plane. Therefore, the actual rate of diffusion turns out to be higher than that evaluated through the row exit plane velocity. As a consequence, this difference must be

considered in the design process to correctly predict the local state of the suction side boundary layer [155].

For low values of Reynolds number (Re), the extent of laminar separation bubbles may be larger and incoming wakes promote their reattachment so that the aerodynamic performance increases. On the contrary, for high values of Re, as separation bubbles are shorter, the loss reduction turns out to be lower. Furthermore, the wake-induced transition occurs earlier since the flow is more receptive to disturbances: the turbulent region grows as well as the level of skin friction rises [155]. It is worth noting that Re decreases from the inlet of turbines to their outlet, whereas the wake passing frequency increases since the number of wake segments rises moving toward the rear part of the machine. These fortuitous effects turn out to be beneficial for performance as the wake passing frequency becomes higher in the last stages, where Re is lower. Consequently, the wake-induced transition may yield higher benefits [156].

The first stages of an airfoil design concern the definition of its geometry at the midspan by applying design criteria that come from the theory and the industrial know-how. Besides, existing blade profiles may be optimized via numerical methods to gain better aerodynamic performance. The latter process is usually carried out under steady conditions to reduce the computational cost. Indeed, in this environment, the single blade is considered without any unsteady disturbances. However, such an approach neglects some of the aforementioned aspects that are crucial to improve the LPT performance and reduce engine weight.

The present work develops a lean model to include the unsteady effects in the airfoil optimization at low TRL, for example, that of a cascade test. The proposed model uses the CFD to analyze the aerodynamic performance of thousands of different

geometries and Artificial Neural Networks (ANNs) to find the design specifications of the optimal airfoil. Therefore, this approach is developed in a trade-off between two aspects: the level of the physical problem complexity (and completeness) and the computational requirements. Even though the former is often overlooked, both aspects are extremely relevant in the early phases of the blade design process.

4.1 Model Description

The present method is aimed at optimizing the midspan airfoil of a single blade in a modeled multi-row environment. The datum profile (colored in green in Figure 4.1) is replicated and mirrored in order to generate the two black airfoils, and consequently a 1.5 stage: the rotational velocity is imposed to the two copies, and thus they act as rotors. Such a configuration allows considering the main unsteady disturbances of LPTs, which are the wake-blade interaction and the potential effect (paragraph 2.2), from the early phases of the design process. This approach evidently intends to model a realistic multi-row environment. Indeed, it is characterized by a higher complexity caused by the three-dimensional blade shape and the differences between stators and rotors in terms of both blade count and blade shape. However, this configuration allows analyzing a multi-row environment at a design stage, in which isolated straight blades are usually considered. In other words, the three-dimensional shaping and the coupling of rows are issues that concern higher TRL levels since these design specifications are

the result of a trade-off among the constraints and the objectives of several disciplines.

Moreover, the proposed model is extremely easy to set up and lean from a computational point of view so that it may represent a feasible alternative to the standard steady optimization process of isolated blades.

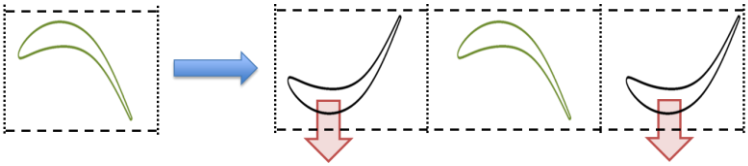

Figure 4.1: Schematic of the model concept

Finally, the present method needs as an input only an airfoil geometry and the related operating conditions. In this frame, the baseline profile has been designed ex novo through the know-how of the research group. In particular, the design concept concerns an aft-loaded, high-lift profile, which respects specific criteria to achieve good performance under unsteady conditions.

In Figure 4.2 the geometrical details of the model are reported. It is worth noting that the C_{ax}, the pitch and the blade axial gap are the same for all of the rows. First, it is obvious that the C_{ax} of the three blades is the same because of the adopted generation method. Second, the axial distance between the blades corresponds to a feasible value for actual LPTs and is equal to the half of the C_{ax}. Finally, the pitch is equal to that of the baseline profile. The reason for the latter choice comes from a numerical issue: it is the configuration associated with the

minimal computational costs under steady and, above all, unsteady conditions. Indeed, the computational requirements under steady conditions only depend on the grid size, i.e., the number of blocks and their size. On the other hand, under unsteady conditions, the computational cost also depends on the adopted time discretization since a time-marching approach is adopted in the present work. The computational requirements increase as different blade counts are adopted in the rows. For example, if the first and the third rows had had a pitch equal to the half of that of the second row, the computational domain would have been composed of 5 blocks. It is true because the circumferential gap of the sum of the modeled blades of each row must coincide. Then, the time-discretization would have been doubled since the highest blade passing frequency had doubled. In summary, the computational cost of the configuration adopted in this activity is 3/5 of that of the example under steady conditions and 3/10 of that under unsteady ones.

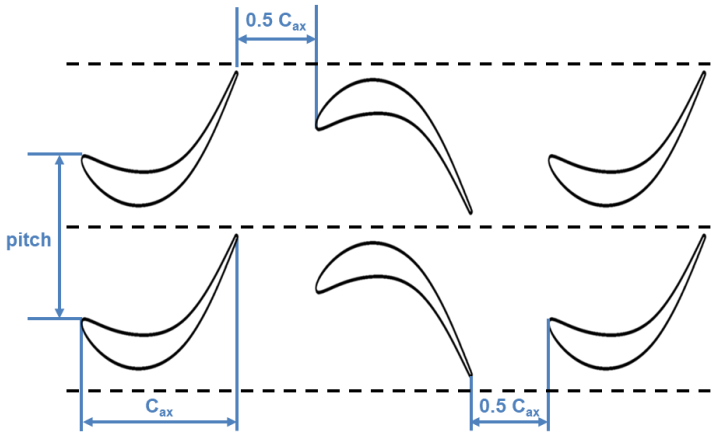

Figure 4.2: Geometry details of the model

The two-dimensional airfoil undergoes a parameterization through an in-house tool so that the geometry can be changed by perturbing the chosen Degrees of Freedom (DoFs) of the original one. This stage is necessary since thousands of different profiles must be generated throughout the activity, and thus an automatic procedure is needed to manage each phase.

The described setup is the starting point for the optimization process of the stator blade in the multi-row environment. Indeed, it is worth recalling that the stator is the blade of interest, while the rotors may be thought of as unsteady disturbance generators. They are representative of LPT blades so that the induced perturbations are realistic. In light of this, the problem considers 10 DoFs and 7 of them are related to the stator.

With respect to Figure 4.3 and Figure 4.4, the DoFs concerning the stator are:

- Inlet blade metal angle α_1'
- Outlet blade metal angle α_2'
- Second control point position $\overline{ab}/\overline{ad}$
- Third control point position $\overline{cd}/\overline{ad}$
- Tangential chord C_t
- Normal thickness of the upper surface reference point
- Curvilinear abscissa of the upper surface reference point position

It is worth noting that the blade metal angles refer to the axial direction. Moreover, the first 5 parameters determine the shape of the blade Pseudo-Camber Line (PCL). On the other hand, the last two DoFs are related to the reference control point of the B-spline, which determines the upper surface semi-thickness that is applied over the PCL. The lower surface semi-thickness

is not altered for three reasons. First, to limit the number of DoFs. Second, the suction side pressure distribution affects the flow-field much more than that over the pressure side. Third, the variation of blade thickness, which is a parameter of interest, may be obtained by changing only the upper surface semi-thickness.

Moving forward, the rotor has 2 DoFs even though its profile does not undergo any optimization process. It is worth underlining that the overall number of DoFs concerning the rotors are 2 and not 4 since the two blades are the same in each configuration. Indeed, the original geometry is perturbed, and then the obtained airfoil is replicated to generate the second rotor. In details, the DoFs concerning the rotor blade are:

- Inlet blade metal angle α_1'
- Second control point position $\overline{ab}/\overline{ad}$

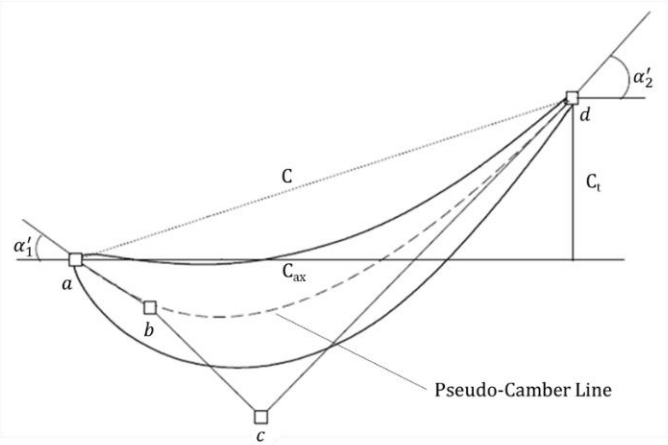

Figure 4.3: Parameters of the PCL

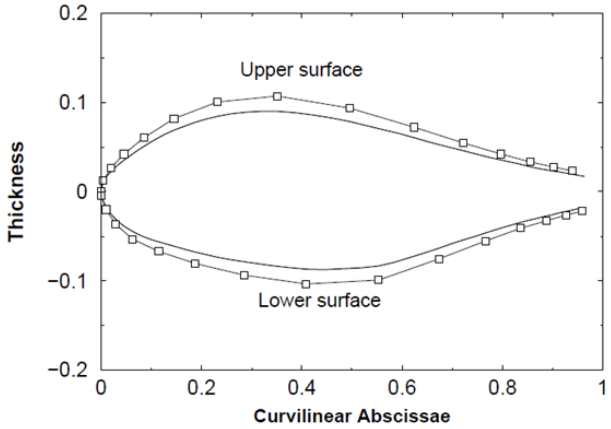

Figure 4.4: Airfoil thickness distributions

The rotor DoFs are necessary to restore the blade deflection to the baseline value as the pitch changes. The use of the singular form for the latter parameter is not casual. Indeed, although it changes with respect to the baseline value, it is always the same for the three rows. As a consequence, the pitch accounts for (only) one more DoF.

It is worth noting that the C_{ax} is kept constant throughout the entire optimization process as it is considered a design datum. By contrast, the stator blade chord (C) may vary since the C_t is one of the DoFs.

As explained in paragraph 3.2.1, a relevant step of the optimization process concerns the generation of the training set for the ANNs. For this reason, 5000 geometries are generated, and their performance is assessed via CFD analyses.

In particular, the generation of the geometries is carried out through the following workflow:

- Determination of the investigated range of each DoF
- Creation of the perturbation files via a Sobol sequence to guarantee a representative sampling of the considered design-space
- Generation of the new airfoils by applying the perturbations to the baseline geometry

The geometries are then meshed, and the rotors are mirrored. It is worth underlining that the latter operation is directly performed on the computational grid.

In this frame, the CFD analysis of each configuration is carried out under steady and unsteady conditions. In the steady simulations, the disturbance due to the upstream blades is modeled via the mixing-plane (paragraph 3.1.4). By contrast, the unsteady analyses consider the time evolution of physical phenomena and the instantaneous interaction between the blades and the unsteady perturbations.

The operating conditions adopted in the analyses are feasible for a test in a low-speed cascade. In particular, Re is chosen equal to 300k that may be considered representative of the nominal condition of this kind of tests.

The first relevant difference between the steady and the unsteady setups concerns the convergence ratio of the analyses. It is equal to 66.8% for the former and 95.2% for the latter. Since the data concerning the non-converged simulations are excluded from the databases, the training set of the steady approach turns out to be almost 2/3 of the unsteady one.

After the training process, the exploration of the design space is performed via ANNs. They allow building a response-surface for each constraint and each objective function. Since ANNs are able to instantaneously predict the performance of any new geometry generated by altering the considered DoFs, the optimization process is carried out by assessing the performance of thousands of configurations via ANNs and selecting the best ones. The used approach is similar to that described in [157].

In particular, the adopted constraints are:

- ϕ equal to the baseline value to preserve the original operating condition
- Thickness (reference point) not smaller than the baseline value for mechanical reasons
- The absolute flow angle at the stator exit (α_2) equal to the baseline homologue to preserve the original blade deflection

It is worth noting that the adopted DoFs and constraints guarantee that the absolute flow angle at the stator inlet (α_1) is the same for all the considered configurations. For this reason, the statement above about the preservation of the baseline blade deflection is valid although α_1 is not explicitly constrained.

The present optimization problem is a single-objective one as the adopted target is the minimization of the stator total pressure loss coefficient (cpt), which is defined as:

$$cpt = \frac{p_{0,in} - p_{0,out}}{p_{0,in} - p_{out}} \tag{4.3}$$

To summarize, the ANNs analyze thousands of geometries and determine the one that generates the lowest amount of loss and simultaneously satisfies all the adopted constraints.

4.2 Numerical setup

The CFD analyses are performed via the TRAF code, an in-house RANS/URANS flow solver. The used turbulence model is the standard Wilcox's k-ω in conjunction with the transition-sensitive model γ-$Re_{\theta,t}$ [127] as LPTs are usually characterized by wide laminar and transitional regions. The consideration of operating conditions feasible for low-speed cascades allows the adoption of the incompressible fluid model so that the number of solved equations reduces from 9 to 8. Consequently, the required computational time diminishes.

The schematic of the 3-blocks domain with its boundary conditions is shown in Figure 4.5. At the inlet, the total pressure (p_0) and the absolute flow angle (α) are enforced. In addition, the turbulence intensity (Tu) is set to 3.5%, while the turbulence length scale (TLS) is equal to 1.5e-03C_{ax}.

Besides, periodicity conditions are imposed onto the tangential boundaries of each row. Finally, at the outlet boundary, the static pressure is enforced. This value as well as the rotational velocity are determined in order to satisfy the kinematic similitude with the isolated baseline blade.

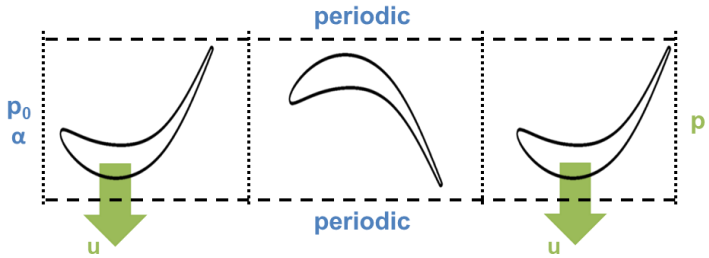

Figure 4.5: Boundary conditions

The computational grid size is the same for the three blocks. The O-type is selected since it guarantees a better discretization around the blade wall. The boundary layer description is crucial for this activity since the transition mechanism and the profile losses are closely related. A Mesh sensitivity analysis has been performed to select the best trade-off between the solution accuracy and the computational domain size. It has resulted in a two-dimensional grid of about 30.5k cells.

As far as the steady simulations are concerned, at the inter-row interface, the pitch-wise average is performed in analogy with the operations performed by the reflecting mixing plane in 3D analyses. By contrast, in the unsteady simulations, any consecutive rows exchange information at the interface every time-step, and thus no averaging operations are performed. Moreover, the unsteady analyses are carried out via the dual-time stepping method: 50 divisions per blade passage and the time-step switch after 15 iterations. The latter value guarantees the residual convergence of each time-step. Since hundreds of calculations simultaneously run, a convergence criterion is necessary to automate their management. In particular, both the residual value and the cpt are checked at the end of the selected number of iterations. In the unsteady calculations, the latter is equal to those forming a blade passing period, while in the steady computations that count is arbitrarily chosen equal to 200. If the residual value is smaller than the adopted threshold and the difference between three consecutive values of cpt is smaller than 0.01%, the calculation is stopped, and its result is considered converged. The steady simulations took less time to reach the convergence than the unsteady ones: about 1/4.

4.2.1 Unsteady Effects

The impact of the wake-blade interaction and the potential effect is assessed for the baseline case by performing two analyses with just two rows in the computational domain. In the first one, the first rotor is omitted, while in the second one, the second rotor is not modeled. Then, the obtained results are compared to those of the configuration with 3 rows (baseline), where the unsteady disturbances are simultaneously present. More in details, the BCs for the configurations with 2 rows are extrapolated from the analysis of the baseline case: the mean values at the row interfaces are used. For example, the mean values between the first rotor and the stator are collected in the baseline configuration. Then, they are enforced at the inlet of the configuration without the first rotor.

Figure 4.6 shows the space-time plots of skin friction coefficient (cf) for the three cases. The left and right graphs look very similar even if the transition mechanism slightly changes as the potential effect acts on the flow-field over the rear part of the blade suction side. Indeed, the inflectional boundary layer associated with the region of low-level cf becomes more robust to transition (paragraph 2.2) than in the configuration without the downstream rotor. On the other hand, the graph in the middle shows minor disturbances on the rear part of the pressure side, whereas a periodic pattern is well observable over most of the suction side.

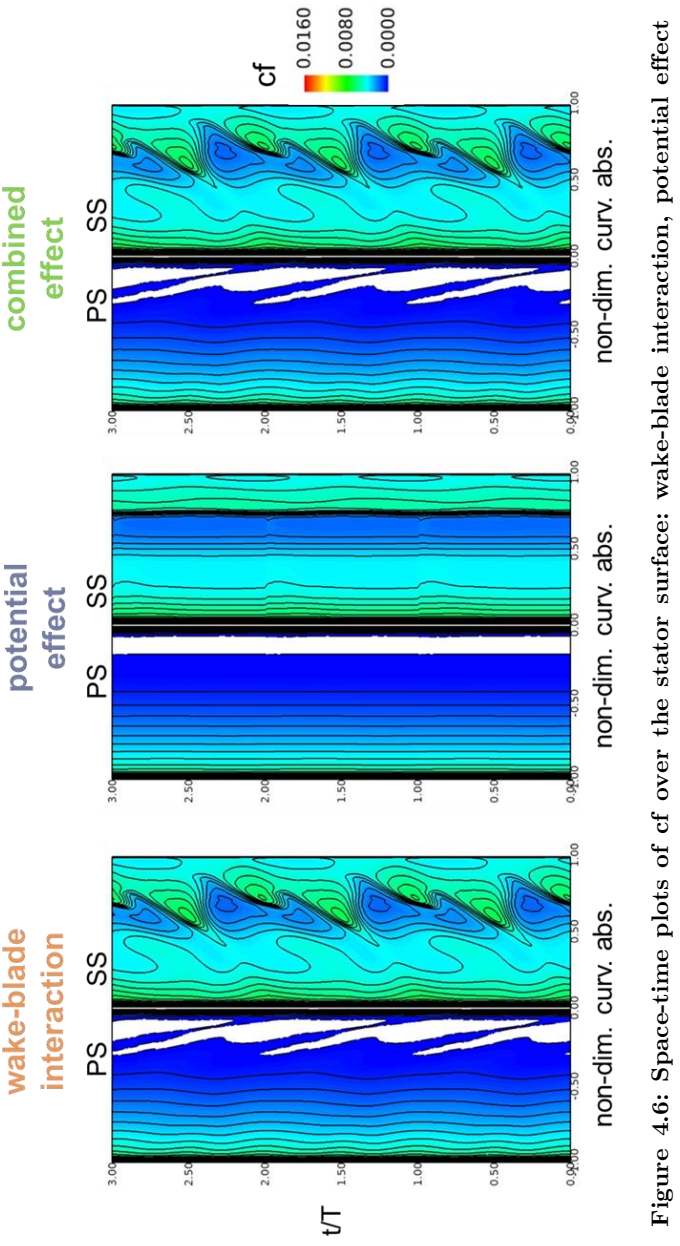

Figure 4.6: Space-time plots of cf over the stator surface: wake-blade interaction, potential effect and their combined effect

To better visualize the impact of the unsteady disturbances on the transition mechanism, the cf distributions over the stator suction side for the three cases are reported in Figure 4.7. The thickest lines represent the time-averaged values, while the thinner ones are the instantaneous distributions: one for each time-step.

The blue distributions show that the potential effect marginally affects the transition mechanism, and its onset does not remarkably displace over the blade passing period. Moreover, the effect is limited to the rear part of the stator suction side. By contrast, the impact of incoming wakes on the transition is apparently dominant. Over the time-period, the onset location significantly varies, and the friction losses are altered even on the front part.

The comparison between the orange and the green distributions shows the interaction between the two unsteady perturbations. Noticeable differences are observable over the second half of the suction side. The minimum and maximum values of cf are essentially the same, but the transition location is altered by the potential effect. This aspect remarkably influences the loss generation. Indeed, the stator cpt for the configuration with only the upstream row turns out to be higher than that of the baseline (+0.04%). This aspect is due to the beneficial effect of the downstream blade on the suction boundary layer that becomes more resistant to transition since the local pressure field is altered. In terms of cpt, the positive effect due to the potential effect accounts for almost 40% of the detrimental one due to the interaction between wake and blade boundary layer. Indeed, the stator cpt related to the configuration without the incoming wake is equal to -0.11% with respect to the baseline.

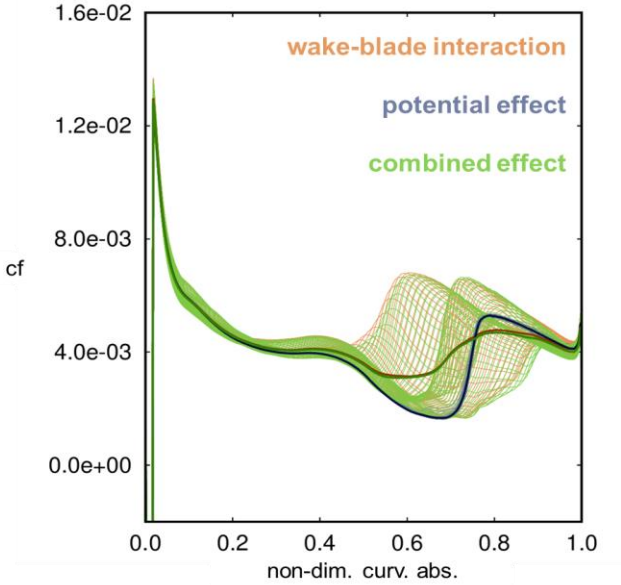

Figure 4.7: time-averaged and instantaneous distributions of cf over the stator suction side length

After highlighting the impact of each unsteady disturbance separately, the aerodynamic performance for the baseline configuration is analyzed in-depth. First, the variation of the blade loading over a blade passing period is reported in Figure 4.8. The incoming wakes determine the blade incidence change over time, and consequently, the pressure distribution varies along the suction and pressure surface. The suction peak changes in terms of both position and magnitude. By contrast, the last 20% of the suction side shows steady behavior.

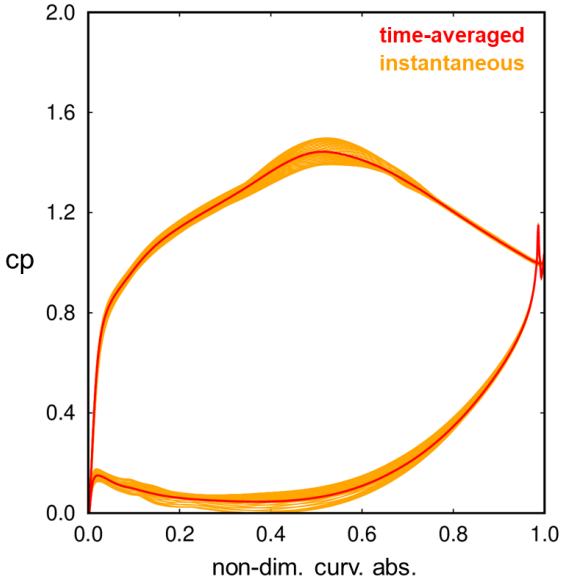

Figure 4.8: Baseline: time-averaged and instantaneous distributions of cp over the stator blade length

Besides, a separation bubble is observable around the 15% of the pressure side length in Figure 4.9, where cf turns negative. The combined effect of the incidence variation and the bubble development causes the pressure distribution to change over time up to the 90% of the pressure side length. However, the unsteady disturbances induce small effects on the pressure side cf, and they are gathered near the separation bubble. On the other hand, the impact on suction side losses is apparent since it alters the transition mechanism.

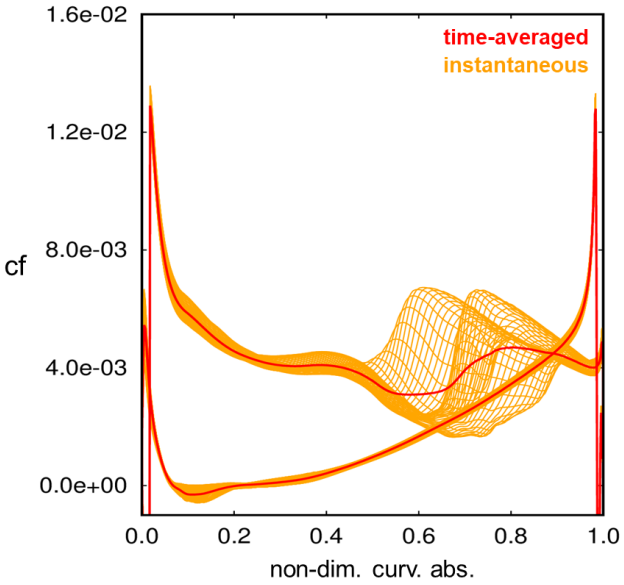

Figure 4.9: Baseline: time-averaged and instantaneous distributions of cf over the stator blade length

The unsteady behavior of the flow-field properties is clearly observable in Figure 4.10, where two space-time (s-t) plots are reported: one considers the $Re_{\theta,t}$, while the other the cf. In the former graph, the wake-induced transition pattern is apparent: each wake triggers the transition, which occurs over the green wedged regions. These are followed by the calmed regions and the regions of incipient separation (colored in red). Indeed, in the path between the wakes, the flow transition does not start before the 75-80% of the suction side length, and thus the laminar flow is more and more unstable under the increasing diffusion intensity. However, the separation does not occur in the rear part of the suction side as the flow transitions via natural mode before any bubble can originate.

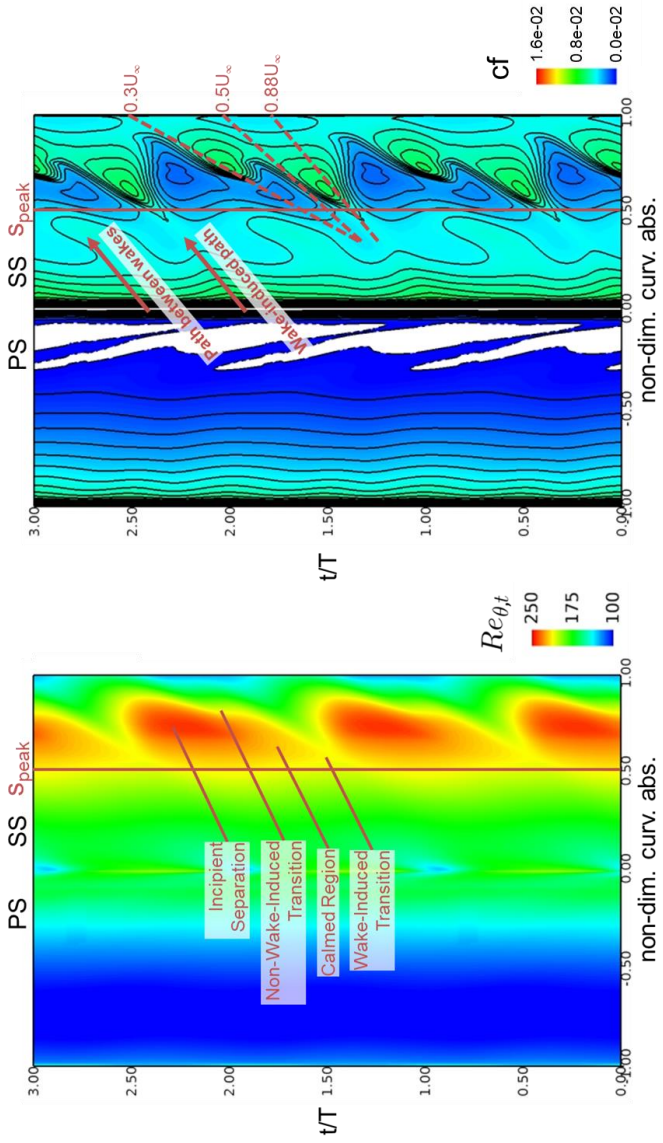

Figure 4.10: Space-time plots for the baseline stator blade. Left: $Re_{\theta,t}$. Right: cf

These aspects are confirmed through the cf plot, where the two paths are highlighted. Likewise, the development of the turbulent spots and the calmed region is marked by three lines: their slopes coincide with the theoretical propagation velocity of the considered phenomena (paragraph 2.3). The calmed regions convect downstream slower than the turbulent spots so that the size of the former increases more than that of the latter moving towards the trailing edge. Besides, the periodic behavior of the separation bubble over the pressure side is clearly observable: it is temporarily suppressed, then generates again and grows in size. Anyway, its impact on the aerodynamic performance might be even beneficial: it may be thought of as a blade part with negligible weight. In other words, it induces additional guidance to the flow without increasing neither the losses nor the LPT weight.

Four equally spaced instants of time within a blade passing period are considered below to highlight the different boundary layer behavior with respect to the wake position in the blade vane. The latter is observable in Figure 4.11 where the contour plots of TKE, divided by the average velocity (U_{ref}), are shown. Moreover, the numerical labels refer to the considered quarter of the period. The development and distortion of the wake within the blade passage (paragraph 2.5.1) are observable. Likewise, the turbulent region over the suction side is noticeable by tracking the red region close to the wall. The transition mechanism analysis may be performed by observing Figure 4.12 which shows the near-wall distributions of TKE/U_{ref}: the time-averaged and the instantaneous ones.

Figure 4.11: baseline configuration: contour plots of TKE/U_{ref} at 4 equally spaced instants within a blade passing period

At instant 1 (the end of the first quarter of the period), one wake segment has just entered the vane and interacts with the separation bubble on the pressure side so that the bubble is suppressed near the leading edge. On the other hand, two traces of the preceding wake segment are detectable near the trailing edge on both the pressure and the suction sides. They are almost parallel to the blade due to the experienced distortions. Although the suction side leg has a high turbulent intensity, the wake-induced mechanism is not triggered yet. Indeed, the transition starts at about the 70% of the suction surface in the natural mode as the local cf level points out (i.e., it is intermediate between those related to the calmed region and the wake-induced transition, respectively).

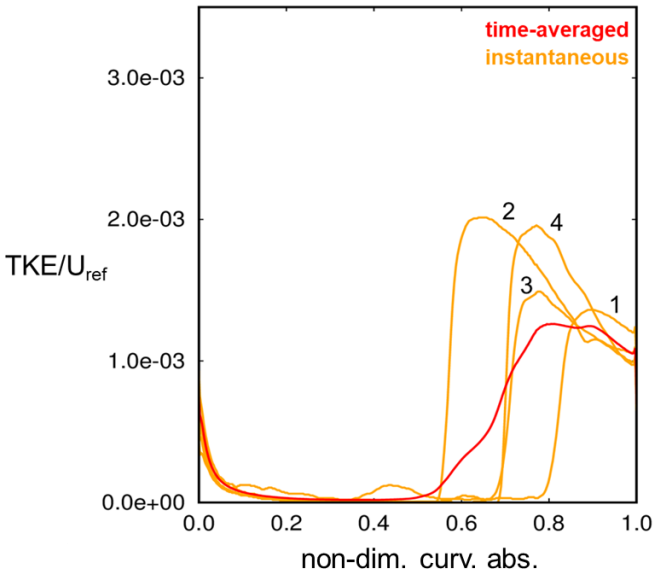

Figure 4.12: Baseline: time-averaged and instantaneous distributions of TKE/U_{ref} over the stator suction side length

It is worth recalling that the wake fluid in the freestream moves downstream faster than that of the boundary layer so that a lag occurs between the wake segment position in the middle of the vane and the flow behavior close to the wall. At instant 2, only one wake segment is present within the vane and is closer to the suction side. The transition over the latter starts much more upstream than before since the turbulence of the previous wake segment has diffused within a wider part of the boundary layer.

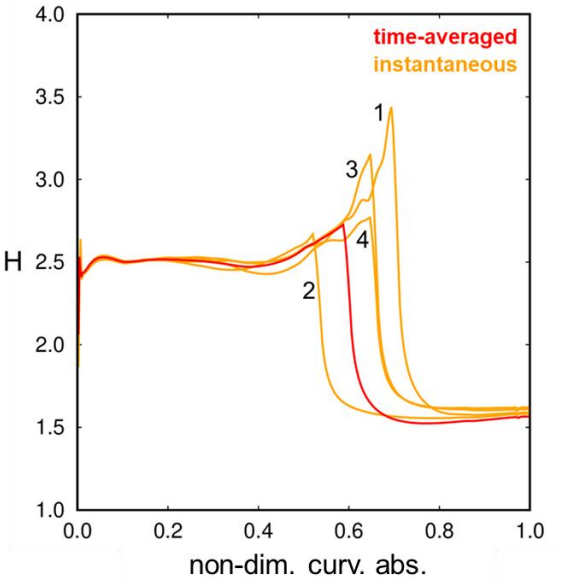

Figure 4.13: Baseline: time-averaged and instantaneous distributions of H over the stator suction side length

The transition onset is located at about the 55% of the suction side length. Moreover, the TKE magnitude is almost double than that at instant 1.

At instant 3, the suction leg of the wake segment reaches the blade wall near the leading edge and shows a much higher turbulence intensity than before. By contrast, the turbulent region over the blade is smaller since the calmed region is present between the 50% and the 70% of the suction side length. Therefore, the transition starts downstream of it, and the TKE peak is similar to that of instant 1. At instant 4, the wake segment elbow is close to the exit plane, and the turbulence intensity of the suction leg has furtherly increased.

The transition onset is located at about the same position of instant 3, but the peak magnitude is much higher since the calmed effect progressively diminishes. The time-averaged distribution does not show a well-defined peak, but rather a plateau that ranges from the 75% to the 95% of the blade suction side. Moving upstream, the time-averaged TKE/U_{ref} gradually reduces and is about zero at the 50% of the suction side. This latter part of the curve is only due to the wake passage that causes the transition onset to move back and forth within the blade passing period as well as the TKE peak changes its location. The average effect of such a displacement reflects on the low slope of the red line.

Figure 4.13 shows the time-averaged and instantaneous distributions of the shape factor (H) over the suction side. It is useful to visualize the boundary layer state at the considered instants. It is apparent the incipient separation at instant 1. Besides, at instant 3 the trend is similar to that of instant 1 before the transition occurs. By contrast, it becomes equal to that at instant 4, thereafter. This behavior is due to the different intensity of the calmed region, and thus it is related to its effectiveness in reducing losses.

It is worth noting that H is evaluated through a lean in-house tool. In particular, the latter solves the Von Karman integral momentum equation via the Thwaites' method for laminar boundary layers and the Head's closure for the turbulent ones. The transition onset (that is the switch from the former method to the latter one) is determined through the TKE distributions over the suction side length.

4.3 Steady Approach

The steady approach corresponds to the standard during the design process as it guarantees satisfactory accuracy in most cases and, above all, its computational cost is lower than that required by the unsteady CFD methods. Since the first design steps involve a large number of calculations to promptly test many different geometries, the steady approach is still the most widespread, especially in the industrial sector.

Differently from a steady analysis of an isolated airfoil, a steady calculation of a multi-row configuration allows evaluating the disturbances of the adjacent blades although they are modeled via the mixing-plane approach. Indeed, the flow-field properties are averaged at the inter-row interfaces in the circumferential direction. Moreover, any temporal evolution of the flow-field is obviously neglected.

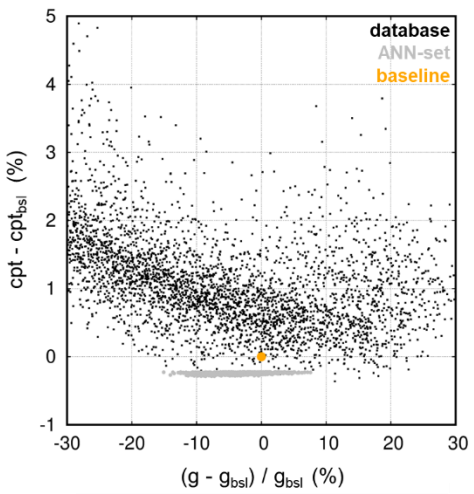

Figure 4.14: Steady approach. Computational cloud and ANN optimal set: cpt vs. blade pitch with respect to the baseline

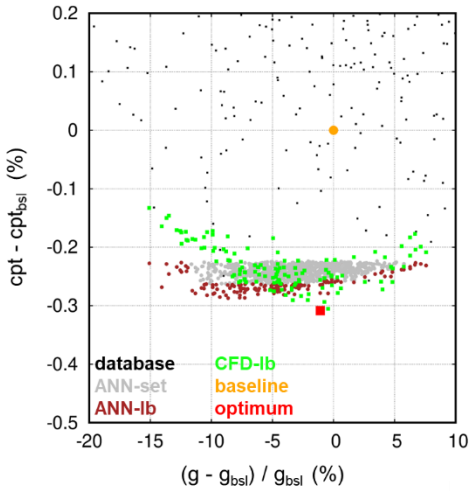

Figure 4.15: Steady approach. Detail of the ANN optimal set: cpt vs. blade pitch with respect to the baseline. Comparison between ANN and CFD results

The results of the CFD steady analyses in terms of cpt are reported in Figure 4.14, where each black dot corresponds to a converged simulation. Likewise, the baseline value (orange dot) is calculated through a CFD steady analysis. By contrast, the grey dots represent the ANN optimal set (ANN-set), which is the result of the design space investigation. In particular, ANN-set collects the geometries associated with the 1000 lowest cpt values among all those generated and assessed by the ANN meta-model. However, the presence of some black dots associated with lower cpt values than those related to the ANN-set may be misleading. Therefore, it must be stressed that such an occurrence is due to the non-application of the constraints listed in paragraph 4.1 when generating the database geometries. Indeed, those constraints are directly applied when the ANN meta-model investigates the design space. In other words, the database geometries associated with cpt values that are lower than those of ANN-set do not respect the adopted constraints. Finally, it is worth highlighting that the present ANN meta-model is trained on the steady result database only.

Figure 4.15 is a zoom of Figure 4.14 in the region of ANN-set, but the geometries on its lower boundary are here colored in brown and labeled ANN-lb. In particular, the entire blade pitch range of ANN-set is considered; however, a higher number of geometries is selected near the ANN cpt minimum. The geometries composing ANN-lb are analyzed via CFD steady calculations, and the corresponding results, referred to as CFD-lb, are superimposed. In other words, the brown dots and the green ones refer to the same geometries, but the method to assess the associated cpt differs: ANN-lb collects the ANN predictions while CFD-lb collects the CFD steady results.

It is apparent that both the cpt trends of the ANN and the CFD results show the presence of a minimum, but its position differs. Indeed, the ANN minimum corresponds to a pitch that is equal to about -8% with respect to the baseline value. By contrast, the CFD optimum (red square) has a pitch that is equal to -1% with respect to the baseline one. It must be stressed that in all the shown geometries, all the DoFs described in paragraph 4.1 can vary, and consequently, the cpt variation is not due to the pitch change only.

In addition, the comparison between ANN and CFD results allows assessing the accuracy of the former model. It is apparent that the ANN error is minimum in the region close to the CFD optimum, while it increases up to 0.09% at the left edge of ANN-set.

Moving forward, it is worth noting that in the present configuration, the pitch variation corresponds to the change of the widespread parameter referred to as Zweifel number. It is the ratio between the actual blade loading and the ideal one, defined for incompressible flows by:

$$Z = \frac{Y}{Y_{id}} = \frac{\dot{m}(c_{y1} + c_{y2})}{(p_{01} - p_2)C_{ax}H} = \frac{\rho g c_x^2(\tan\alpha_1 + \tan\alpha_2)}{(p_{01} - p_2)C_{ax}} \qquad 4.4$$

where c_y is the absolute tangential velocity, C_{ax} is the axial chord, H is the blade height, and c_x is the axial velocity. Since all these parameters are kept constant except for the blade pitch, any variation of g may be translated into a change of Z.

The stator airfoils corresponding to all the simulated geometries are shown on the left side of Figure 4.16. Besides, the baseline blade profile and those of CFD-lb (which coincide with those of ANN-lb) are reported. On the right side, the optimal geometry

is superimposed to the baseline one. It is worth noting that the blade front part of the optimum airfoil is very similar to that of the baseline geometry, while they remarkably differ in the portion after the 30% of C_{ax}.

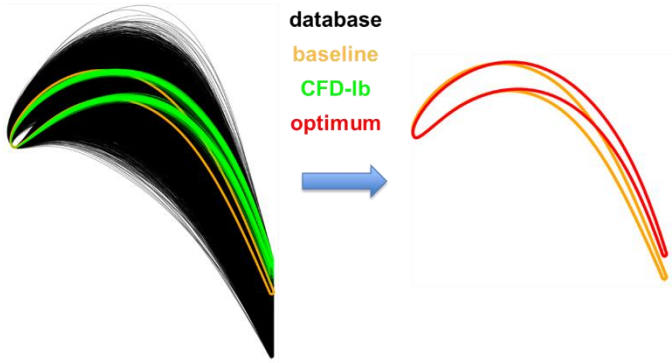

Figure 4.16: Steady approach: stator blade airfoils of the investigated geometries

Moving forward, Figure 4.17 shows the comparison between the aerodynamic blade loading for the baseline and the optimum. It is apparent that the concepts behind these pressure distributions are significantly different: the controlled diffusion of the baseline geometry is overcome by an extreme aft-loading in the optimum. Moreover, the optimum is characterized by a fuller pressure side in order to become more similar to the ideal blade loading of the Zweifel criterion theory.

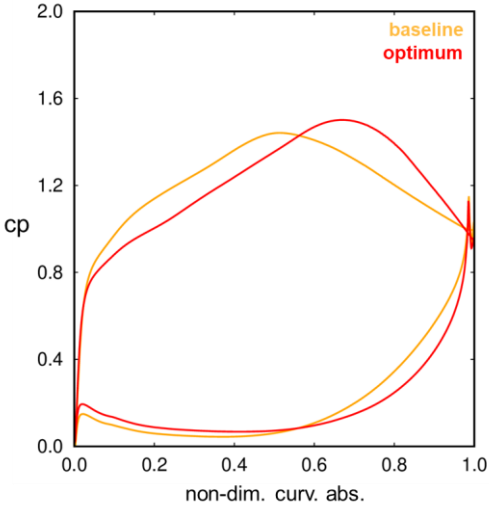

Figure 4.17: Steady approach: cp distribution over the stator blade length

4.3.1 Design Specifications

A more detailed description of the two geometries requires the use of the most widespread design parameters. Moreover, the computational clouds allow visualizing the influence on cpt of the different parameters over a wide range of values so that some general trends may be observed.

The first computational cloud (Figure 4.18) concerns the impact of the pitch-to-chord ratio (g/C). It is a fundamental parameter since it is closely related to the profile losses and the blade count of a row. Indeed, the flow has more guidance from the blades

when their spacing is low, but the skin friction losses increase. By contrast, large values of g/C determine a higher risk of incurring separation, but the blade wetted surface reduces.

The CFD-lb geometries (green dots) cluster in the region of the baseline case. Indeed, the optimum g/C is about 2% larger than that of the baseline. Since the ANN suggests the reduction in blade pitch, the increase in optimal g/C with respect to the baseline implies the blade chord decrease, which is clearly observable in Figure 4.16.

The second (Figure 4.19) and the third (Figure 4.20) computational clouds show the influence of the diffusion on the cpt in terms of diffusion factor (DF) and diffusion rate (DR). It is apparent that the DR increase (+74%) is much higher than that of DF (+18%). This difference is due to the extreme aft-loading concept behind the optimum blade loading. Indeed, the suction peak position (Figure 4.21) is significantly pushed towards the blade trailing edge (+29%), and consequently, the length of the diffusive region over the suction side is considerably reduced. Since this length coincides with the DR denominator, the value of DR significantly rises despite the DF increase is moderate.

These aspects may also be visualized in Figure 4.22 that shows the computational cloud of DF against the suction peak position. The CFD-lb geometries are clustered at a DF value, which is moderately increased with respect to the baseline. By contrast, the associated suction peak positions build up around the 70% of the suction length. These values of diffusion and suction peak position are feasible as they do not determine the boundary layer separation under these operating conditions.

In this frame, the extreme aft-loading of the blade profile guarantees a great benefit in terms of cpt reduction as the extent of the turbulent region over the suction surface reduces, and consequently, the profile losses decrease. Contrarily, for a given DF, the suction peak displacement towards the leading edge would have been beneficial in presence of separation bubbles if the related mixing losses had overcome the profile ones [158].

It is worth noting that the difference between the peak of the optimum and that of the baseline is not large enough to generate by itself the reported DF discrepancy. Indeed, that value is caused by the remarkable increase in the unguided turning (UGT) (+55%) for the optimum geometry that is observable in Figure 4.23.

As explained above, an increase in UGT determines a strong potential field around the blade trailing edge, and thus the local velocity becomes lower than that at the row exit plane. As a consequence, for a given value of minimum pressure over the suction side, the DF increases as the UGT rises.

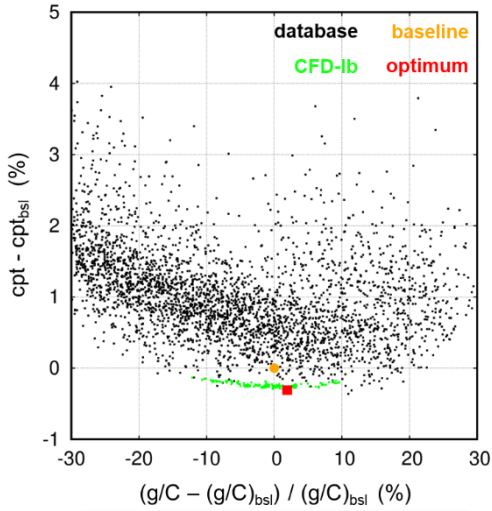

Figure 4.18: Steady approach: cpt vs. g/C with respect to the baseline

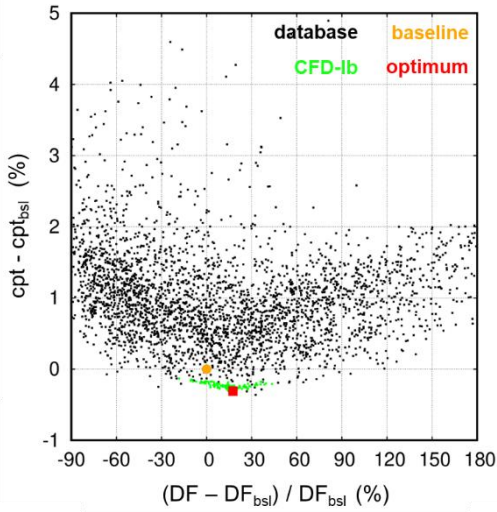

Figure 4.19: Steady approach: cpt vs. DF with respect to the baseline

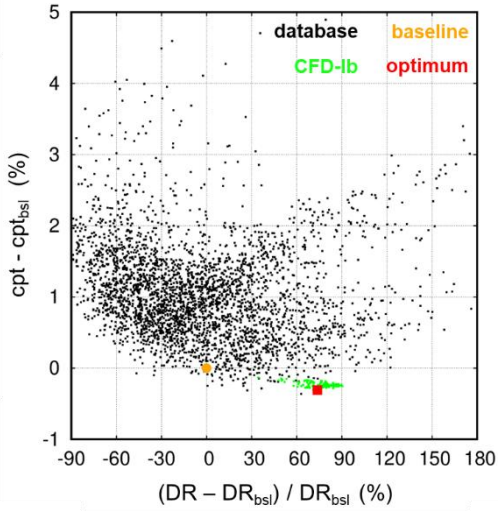

Figure 4.20: Steady approach: cpt vs. DR with respect to the baseline case

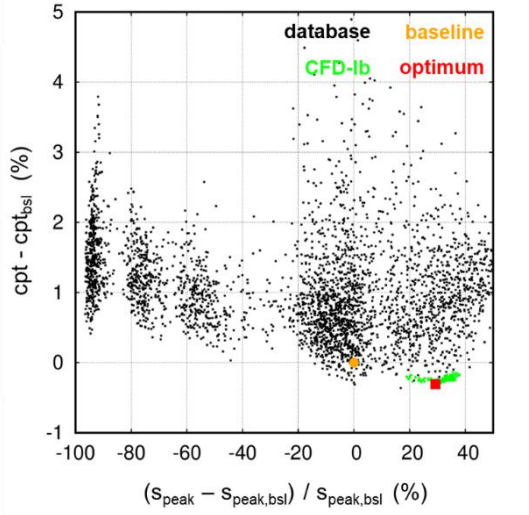

Figure 4.21: Steady approach: cpt vs. s_{peak} with respect to the baseline

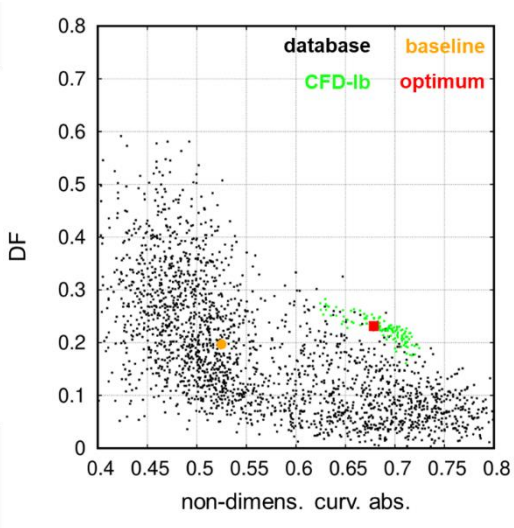

Figure 4.22: Steady approach: DF vs. non-dimensional s_{peak}

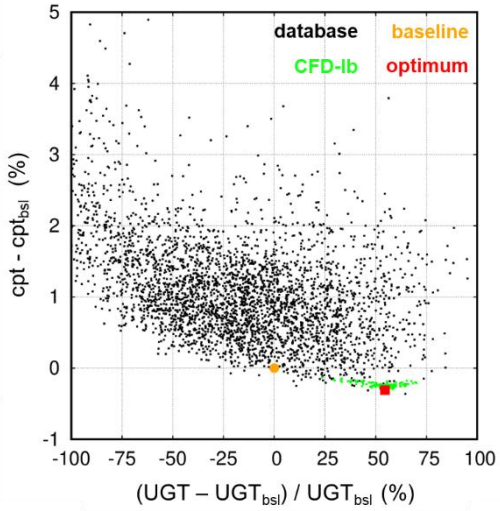

Figure 4.23: Steady approach: cpt vs. UGT with respect to the baseline

4.3.2 Flow-Field Analysis

The design specifications of the optimum cause relevant variations in the flow-field with respect to the baseline. In particular, the wake-blade interaction, and thus the transition mechanism shows the main differences. Therefore, the unsteady analysis of the optimum obtained through the steady approach (OPT-S) is performed, and the related results are reported herein.

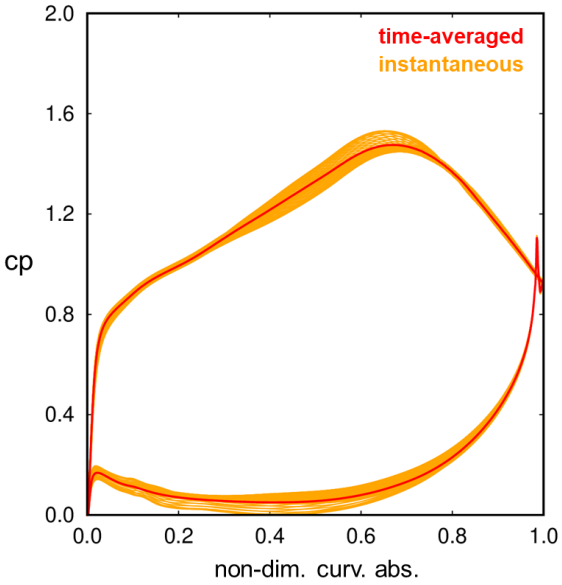

Figure 4.24: OPT-S: time-averaged and instantaneous distributions of cp over the stator blade length

Figure 4.24 shows the time-averaged and the instantaneous cp for the optimum case. The displacement of the suction peak towards the blade trailing edge results in a wider extent of the

region affected by the unsteady disturbances. However, the traces of the unsteadiness nearly disappear after the suction peak, differently from the baseline case (Figure 4.8).

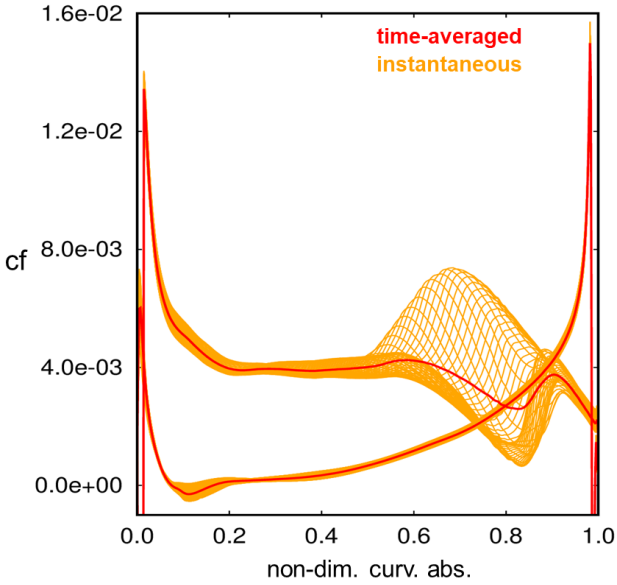

Figure 4.25: OPT-S: time-averaged and instantaneous distributions of cf over the stator blade length

This aspect is due to the velocity distribution over the suction side: a significant acceleration over the first 68% of its length that keeps the boundary layer under laminar conditions and well attached to the wall. The peak is very pronounced since it connects a region characterized by high-level acceleration to one, in which the diffusion is even more severe.

The effect of the diffusion is apparent in Figure 4.25, where the time-averaged and the instantaneous distributions of cf are reported. It is clear that the curves associated with the

instantaneous distributions cluster at a skin friction level that is close to the lowest one. This proves that a wide laminar region is present most of the time. Moreover, the transition onset location does not significantly vary in the time-lapse between two consecutive wakes. By contrast, the transition triggered by the wake turbulence starts much earlier: at some instants even at the 50% of the suction side length. On the other hand, the main part of the pressure side (85% of the length) is affected by unsteady effects even though their impact causes a lower aerodynamic penalty. Moreover, they are mainly connected to the development of the short separation bubble located between the 5% and the 20% of the pressure side length itself (Figure 4.25).

The transition mechanism may be further analyzed by observing Figure 4.26 that shows the space-time plots of $Re_{\theta,t}$ and cf. On the left side of the figure, the most apparent difference with respect to the baseline homologue is the size and the intensity of the red regions between the wakes. Indeed, they start before the suction peak and cover the entire diffusive region except for the wake-connected structures: the yellow narrow region between the area of incipient separation (intense red) on the one side and the calmed region (orange) on the other one. After the suction peak, the turbulent region (wedged green area) is clearly observable. On the right side of the figure, the non-wake-induced transition is recognizable in the path between wakes. It covers a much smaller region than that in the baseline. Likewise, the wedged shape area is much narrower and elongated for the optimum. Above all, the skin-friction level is significantly lower than that of the baseline over the entire blade surface. Indeed, this is valid for the pressure side too. Besides, the separation bubble extent significantly reduces.

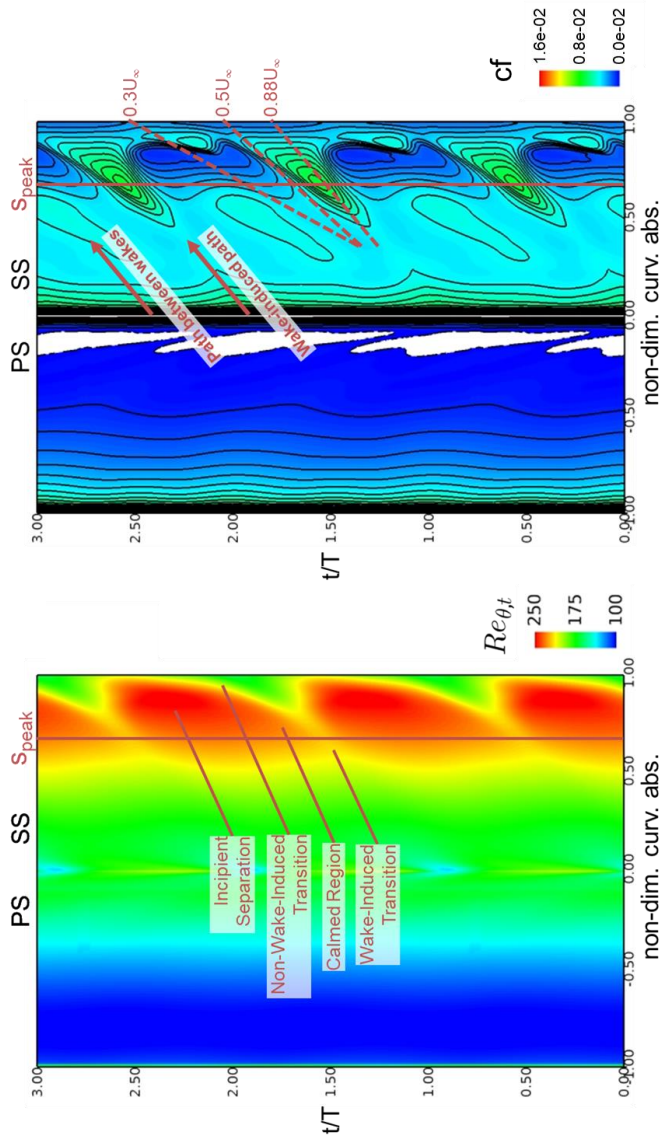

Figure 4.26: OPT-S: s-t plots for the stator blade. Left: $Re_{\theta,t}$. Right: cf

Moving forward, four equally spaced instantaneous contour plots of TKE/U_{ref} are reported in Figure 4.27. The evolution of the wake within the blade passage is similar to that of the baseline case since the pitch variation is small. However, some minor differences are observable. First, the TKE intensity of the wake region is lower in the optimum configuration at every phase. Then, the interaction between the pressure leg of the wake and the pressure side boundary layer looks weaker than that in the baseline case. Finally, it is worth noting that the TKE level near the pressure side is noticeable lower for the optimum, especially over the first 60% in length.

The TKE/U_{ref} evolution over the blade suction side is reported in Figure 4.28 for the same instants of the contour plots. At instant 1, the rear part of the suction side is covered by the incipient separation region. Indeed, the turbulence is nearly zero up to the 82% of the suction side length, then the flow transitions. Besides, the local TKE peak, which is observable at about the 45% of the blade length, is the trace of the incoming wake that cannot trigger the transition at that location due to the high local acceleration. At instant 2, two consecutive TKE peaks are present at the 65% and the 90% of the suction side length, respectively. The first, which is the absolute maximum, is due to the wake-induced transition, while the second is related to the non-wake-induced transition triggered in between two consecutive wakes. At instant 3, the calmed region induces the transition delay with respect to instant 2, and thus it starts at about the 72% of the suction side length. However, the related TKE peak reaches the highest value as the wake turbulence is present over the rear part of the blade.

Figure 4.27: OPT-S: contour plots of TKE/U_{ref} at 4 equally spaced instants within a blade passing period

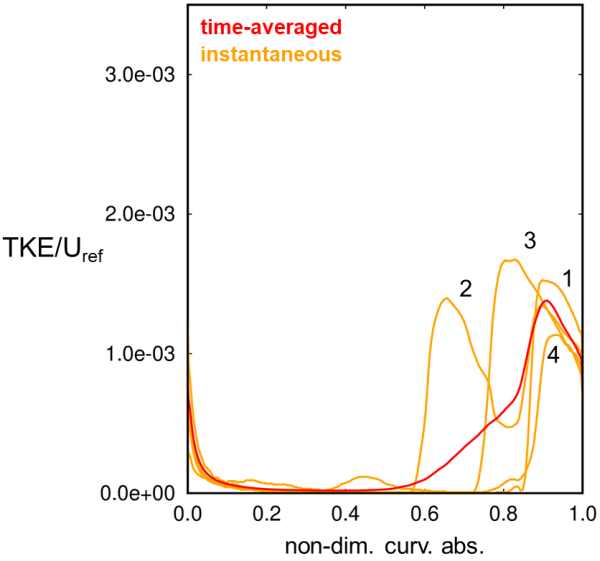

Figure 4.28: OPT-S: time-averaged and instantaneous distributions of TKE/U_{ref} over the stator suction side length

The TKE distribution at instant 4 shows a trend, which is similar to that of instant 1. The onset is moderately displaced towards the leading edge and the flow separation is slightly less incipient so that the TKE growth rate has a different slope, and above all, the peak is lower. In other words, the transition mechanism is less sudden.

The time-averaged distribution well summarizes the aforementioned aspects. The TKE growth starts downstream with respect to that of the baseline case, and the slope remarkably increases at about the 80% of the suction side length. This shape is due to the wake effect, which induces an early transition, while between two consecutive wakes, the onset

is pushed towards the trailing edge. In other words, the instantaneous TKE peaks always occur in the last 15-20% of the blade in between two wake passages. As a consequence, the time-averaged absolute maximum is higher than that of the baseline.

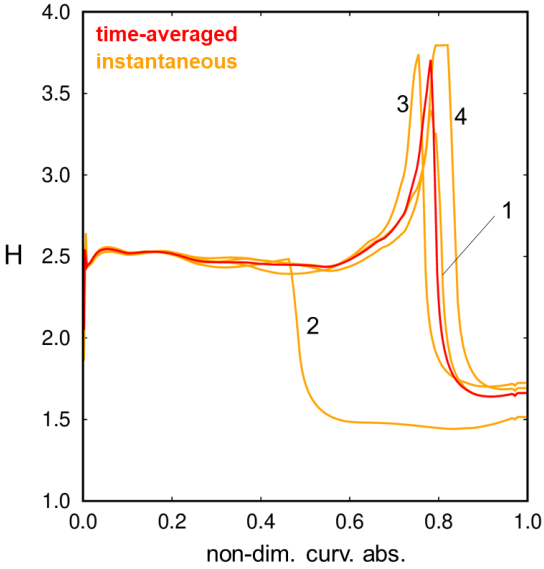

Figure 4.29: OPT-S: time-averaged and instantaneous distributions of H over the stator suction side length

The time-averaged and instantaneous distributions of H over the suction side are reported in Figure 4.29. It is apparent that away from the wake-induced transition (instant 2), the laminar region is remarkably large. Simultaneously, the boundary layer is very close to separate on the rear part of the blade. At instant

4, a small plateau is observable at about the 80% of the suction side length. It is due to the local critical state of the boundary layer: the transition is incipient, but it has not started yet. As a consequence, the correlations (paragraph 4.2.1) used to determine H locally fail since the flow is already non-laminar even if the transition onset (Figure 4.28) is located slightly downstream (i.e., at the end of the plateau towards the trailing edge).

In conclusion, OPT-S shows an extreme design concept: the performance benefits are mainly due to the suction peak dislocation and the related extension of the laminar region. It is worth noting that the adopted increase in DR does not determine the development of any separation bubbles. However, this fact is valid under the considered nominal conditions: operating point and turbulence level. Also, it is true for this reduced frequency. In other words, the aerodynamic performance of OPT-S, which tends to the feasible limits in terms of design parameters, must be double-checked in all the engine operating points, especially far from the design condition.

4.4 Unsteady Approach

The research in the LPT field has been focused on the transition mechanism for decades as its detailed knowledge is the key to succeed in maximizing the aerodynamic performance and, more specifically, minimizing the profile losses. The phenomenon of transition is closely related to the unsteady effects in LPTs as the wake-blade interaction is crucial at such operating

conditions. Therefore, this model is aimed at including the unsteady effects in the design process from the earliest phases. The proposed method is meant to be lean from a technical point of view and in terms of computational costs. Furthermore, the comparison with the steady approach is necessary to detect and assess the different design specifications due to the consideration of unsteady disturbances. Consequently, the results concerning the unsteady approach are reported herein in analogy with those of the steady method.

Figure 4.30 shows the computational cloud of cpt against the blade pitch: both referred to the homologous baseline values (the cpt value results from an unsteady calculation). The highest convergence ratio associated with the URANS calculations determines a noticeably higher number of available data (black dots) in this database than in the steady approach one. This aspect is crucial for the ANN model accuracy as the following results prove. As in the steady approach, the geometries associated with non-converged analyses are not included in the database.

It is worth noting that the lower robustness of steady calculations is not due to code drawbacks, but rather, it is caused by specific flow characteristics that occur in some regions of the investigated design space. In other words, the steady approach is not feasible to model the significantly unsteady flow-fields, which may arise from the choice of the design specifications. Therefore, this obstacle cannot be overcome by increasing the number of considered geometries. Indeed, the steady calculations of the airfoils, which belong to some specific regions of the design space, would keep on failing. As a consequence, the difference in accuracy between steady and unsteady approaches is not uniformly distributed over the entire

design space, but clusters in those regions where the unsteady phenomena are more relevant. Moreover, the local accuracy of the steady ANN model is not known a priori.

In light of this, only the ANN response surface built via the use of the unsteady database may correctly estimate the aerodynamic performance over the entire design space.

As already mentioned in paragraph 4.3, the presence of lower cpt values in the database than in ANN-set is due to the non-application of the constraints in the generation of the database geometries (paragraph 4.1). Indeed, such constraints are applied directly when the ANN meta-model investigates the design space.

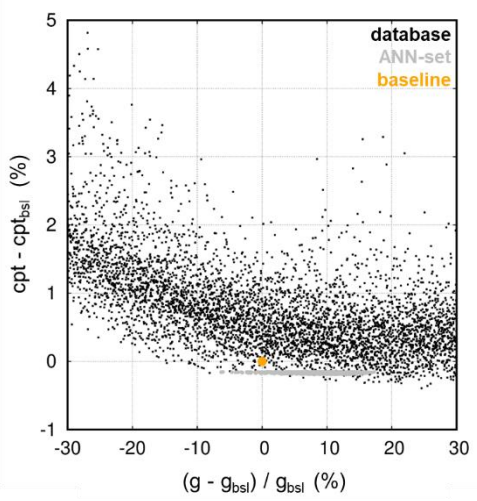

Figure 4.30: Unsteady approach: Computational cloud and ANN optimal set: cpt vs. blade pitch with respect to the baseline

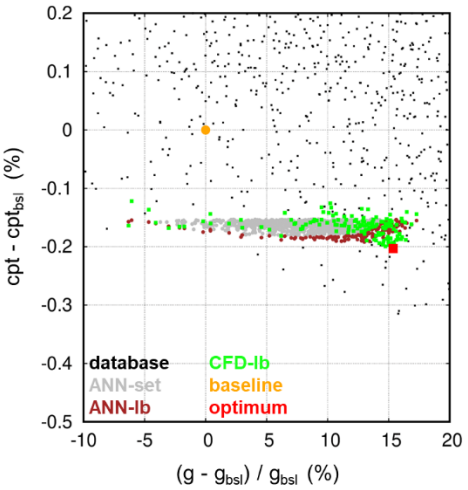

Figure 4.31: Unsteady approach: detail of the ANN optimal set: cpt vs. blade pitch with respect to the baseline. Comparison between ANN and CFD results

In Figure 4.31, ANN-lb collects the geometries of ANN-set located on its lower boundary. In other words, ANN-lb is a subset of ANN-set and includes the geometries associated with the lowest cpt over the entire blade pitch range of ANN-set; however, a higher number of geometries is considered near the ANN-set cpt minimum. In conclusion, the brown and green dots refer to the same geometries, and they are the ANN and URANS results, respectively.

The analysis of ANN-lb and CFD-lb clearly shows that in both cases, the cpt minimum is pushed towards higher values of row pitch than that of the baseline value. In particular, the CFD optimum (red square) has a pitch equal to +15% with respect to the baseline one. The comparison between ANN and CFD

results highlights a better agreement with respect to that for the steady approach: the maximum error in cpt assessment is equal to 0.05%. Likewise, the error about the optimal pitch is lower, i.e., less than 3%.

Figure 4.32 shows all the investigated stator geometries on the left, while on the right the optimum (for the unsteady approach) is superimposed to the baseline airfoil. It is apparent that the optimum blade chord is almost unchanged with respect to the baseline one.

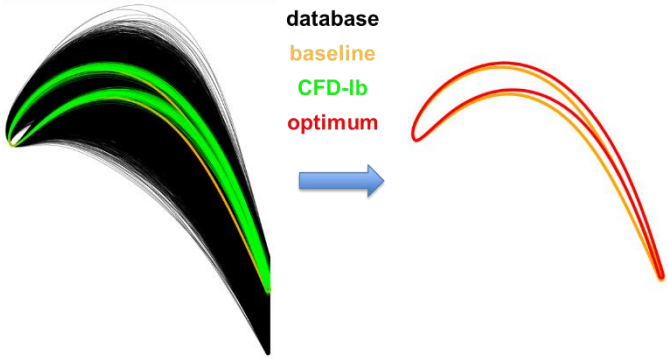

Figure 4.32: Unsteady approach: stator blade airfoils of the investigated geometries

The larger pitch and similar chord length determine the increased blade loading that is observable in Figure 4.33. The geometry is more aft-loaded than the baseline one. Furthermore, the maximum cp region is flatter with a wide plateau, rather than a peak. As for OPT-S, the diagram is fuller in the second half of the pressure side to become more similar to the ideal pressure distribution of the Zweifel criterion.

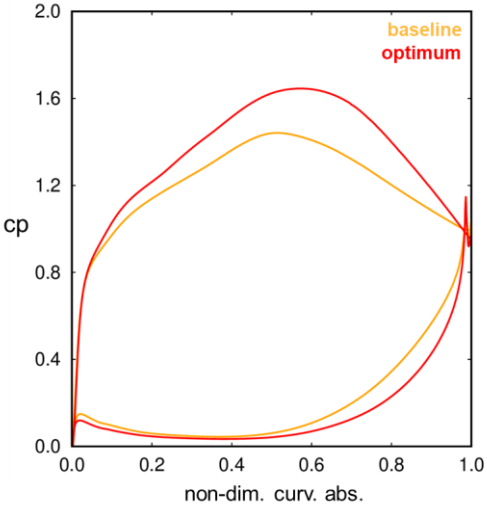

Figure 4.33: Unsteady approach: time-averaged cp distribution over the stator blade length

4.4.1 Design Specifications

The computational clouds of the main design parameters for the optimum obtained via the unsteady approach are reported herein.

The CFD-lb of Figure 4.34, which shows the cpt against the pitch-to-chord ratio, is very stretched, and some geometries have a pitch even smaller than the baseline. However, the latter ones are isolated cases, and, above all, their performance is lower than that of the cluster around the optimum. Besides, even if the performance had been equal, the configurations associated

with larger values of g/C would have been better since it is linked to a lower blade count for the considered row. Consequently, the LPT weight would have lowered, and such aspect is beneficial in terms of specific fuel consumption of the engine. A remarkable difference between the database results in Figure 4.30 and Figure 4.34 concerns the trend of cpt. In the latter, the presence of a region of minimal values is clearly observable and corresponds to the optimum location. By contrast, the losses show a linear trend in that region by merely increasing the pitch.

The data about the diffusion are in contrast with those obtained through the steady approach, except for DR (Figure 4.36). Indeed, both the methods suggest a remarkable increase in that parameter, even if the value related to the optimum of the unsteady approach (+64%) is lower than that of the steady one. However, the main difference between the two methods is in the adopted strategy to enhance DR. Indeed, in the current approach it is obtained via the increase in DF (+47% with respect to the baseline, Figure 4.35) rather than the displacement of the suction peak position (just +9% with respect to the baseline, Figure 4.37). By contrast, in the steady method, the suction peak variation is even greater than that of DF. In addition, the increase in g/C causes DF to rise as the blade loading, and thus the suction peak increases. The solution offered by the present approach is more conservative since the diffusion region over the suction side is larger. This aspect is clearly beneficial for the boundary layer robustness against separation, especially under off-design operating conditions. On the other hand, the turbulent region after the suction peak may be wider and the related losses rise. However, the overall cpt value guarantees that this effect is balanced by other characteristics of the blade. Indeed, the OPT-U cpt is lower

than that of OPT-S obtained via the CFD unsteady simulation. Figure 4.38 shows the DF against the suction peak position and confirms the considerations above. Most of the optimal geometries concern a moderate increase in blade aft-loading, while their DF is kept around the value of 0.3.

The unsteady ANN data about the UGT confirms the trend observed in the steady approach that corresponds to a severe increase in that parameter with respect to the baseline case: the variation of the optimum geometry is equal to +65% (Figure 4.39).

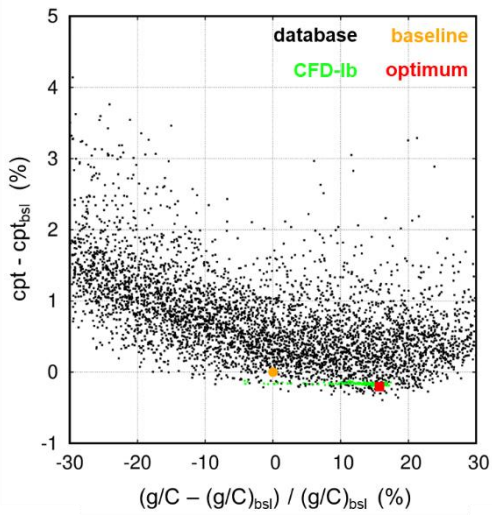

Figure 4.34: Unsteady approach: cpt vs. g/C with respect to the baseline

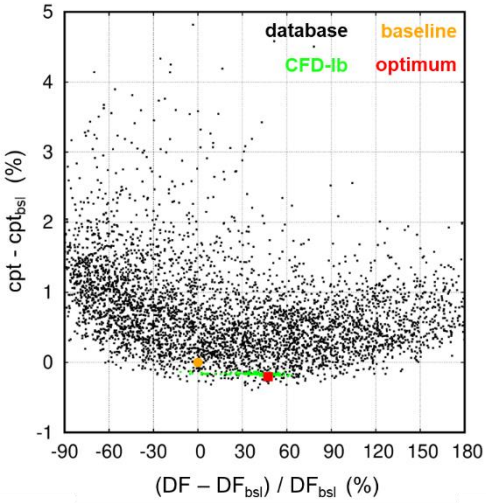

Figure 4.35: Unsteady approach: cpt vs. DF with respect to the baseline

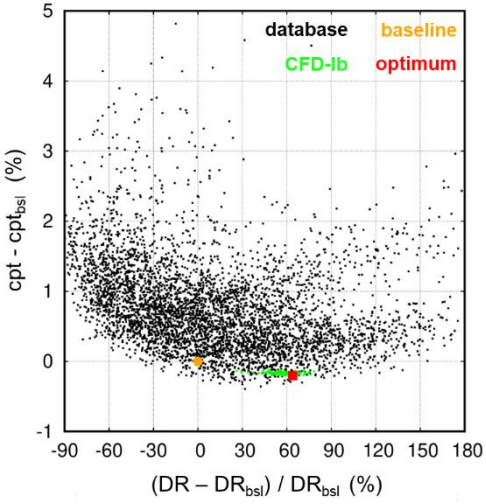

Figure 4.36: Unsteady approach: cpt vs. DR with respect to the baseline

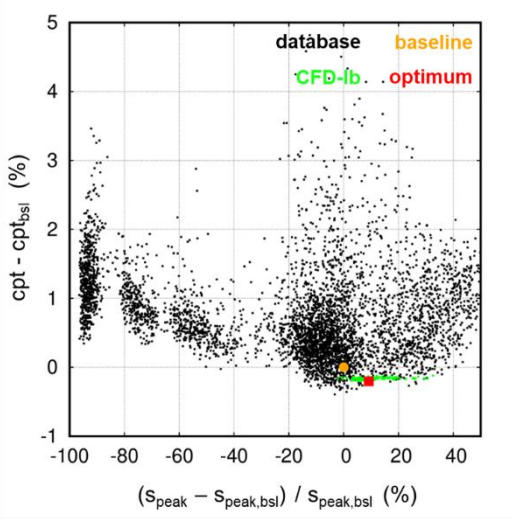

Figure 4.37: Unsteady approach: cpt vs. s_{peak} with respect to the baseline

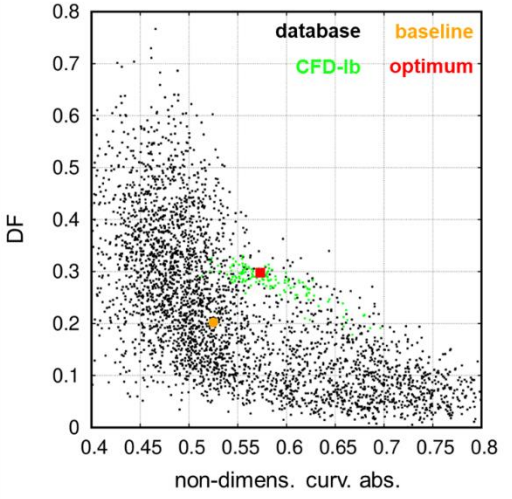

Figure 4.38: Unsteady approach: DF vs. non-dimensional s_{peak}

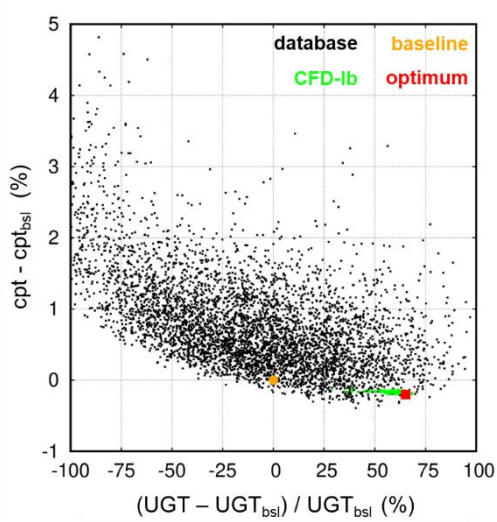

Figure 4.39: Unsteady approach: cpt vs. UGT with respect to the baseline

4.4.2 Flow-Field Analysis

The optimum for the unsteady approach (OPT-U) is analyzed herein by focusing on the development over time of the main physical phenomena. Figure 4.40 shows the time-averaged and the instantaneous distributions of blade loading. The incidence variation looks moderate while the change in pressure distribution, especially near the pressure peak is remarkable. The unsteady effects on the diffusive part of the suction side are much less intense with a steep decay after the maximum. This aspect is a characteristic of both the optima obtained via the steady and the unsteady approach, respectively. By contrast,

the cp distribution over the pressure side is affected by unsteady effects up to 95% of its length.

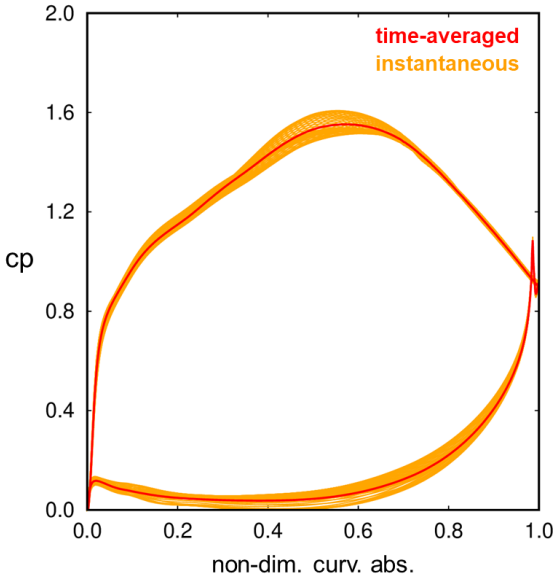

Figure 4.40: OPT-U: time-averaged and instantaneous distributions of cp over the stator blade length

The time-averaged and the instantaneous cf distributions are reported in Figure 4.41. The transition impact on the cf distribution is similar to that of the baseline, especially as far as the wake-induced mode is concerned. However, the transition averagely occurs downstream, at about the 70% of the suction side length, and this aspect is crucial in determining the turbulent region size and thus the magnitude of the profile loss. Moreover, a remarkable difference is observable in the rear part

of the blade, where the cf steeply decreases, while the baseline geometry guarantees a constant cf value in that region.

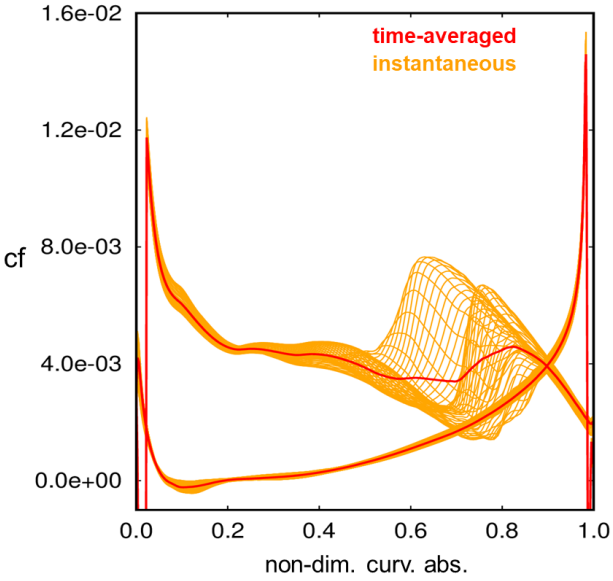

Figure 4.41: OPT-U: time-averaged and instantaneous distributions of cf over the stator blade length

On the pressure side, a separation bubble is observable near the leading edge. Not only it is small, but also its evolution over time is limited.

The detailed analysis of the transition mechanism may be performed by observing Figure 4.42, which shows the space-time plots of $Re_{\theta,t}$ (left) and cf (right).

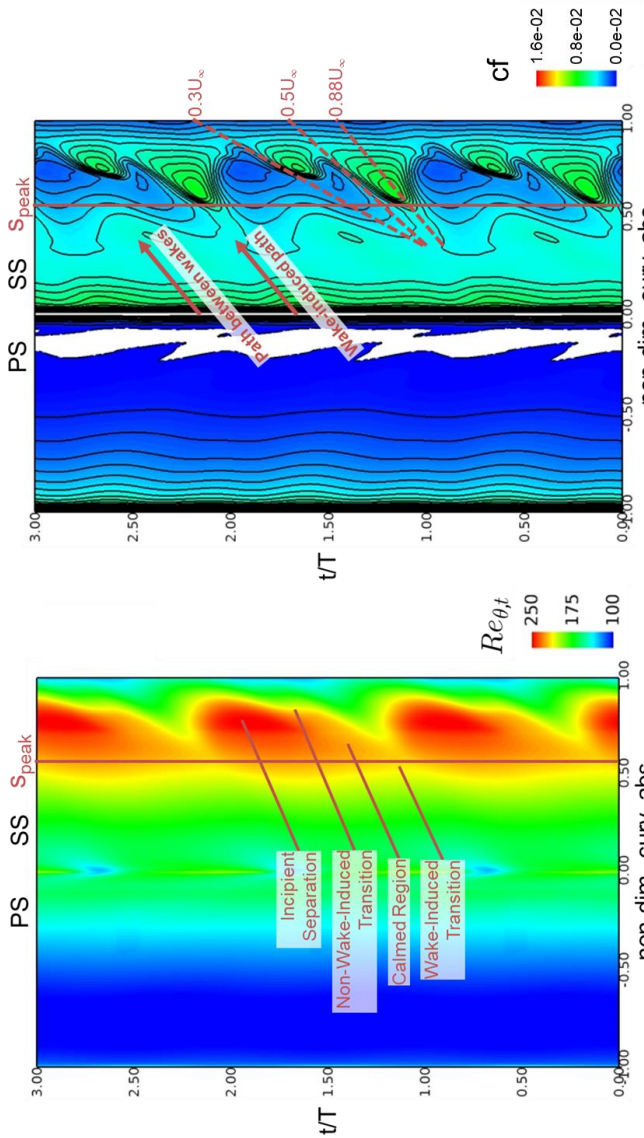

Figure 4.42: OPT-U: s-t plots for the stator blade. Left: $Re_{\theta,t}$. Right: cf

The former graph highlights the presence of wide regions where the flow is predominantly laminar, and the transition occurs via the natural mode immediately before the 80% of the suction side length. Between the incipient separation region and the wake, the calmed region is clearly observable (colored in orange). It is characterized by the low skin friction level enclosed by the dashed lines on the right side of the figure. In the calmed region trajectory towards the trailing edge, the transition occurs upstream with respect to the natural transition onset as the skin friction level is in between that of the wake and that of the laminar region. As far as the pressure side separation is concerned, it never disappears over the blade passing period, and its extent is nearly constant over time.

Moving forward, the wake evolution within the blade passage is observable in Figure 4.43 at four equally spaced instants of one blade passing period. It is worth noting that the relative position between the incoming wakes and the blade is not in phase with the homologous figures for the baseline and OPT-S. It is due to the different pitch since the reduced frequency is not preserved in the present model. In other words, the reduced frequency only depends on the stator pitch since the flow coefficient and the rotor chord are kept constant while the pitch varies in accordance with the stator one. Besides, the increase in pitch determines a higher TKE level in the wake region with respect to the previous cases. The wake width immediately downstream of the trailing edge is also noticeably larger. Contrarily, the TKE level near the pressure side is moderate as well as the interaction with the pressure side leg of the wake is.

The TKE distributions over the suction side surface at these instants are reported in Figure 4.44, where the time-averaged distribution is also shown.

Figure 4.43: OPT-U: contour plots of TKE/U_{ref} at 4 equally spaced instants within a blade passing period

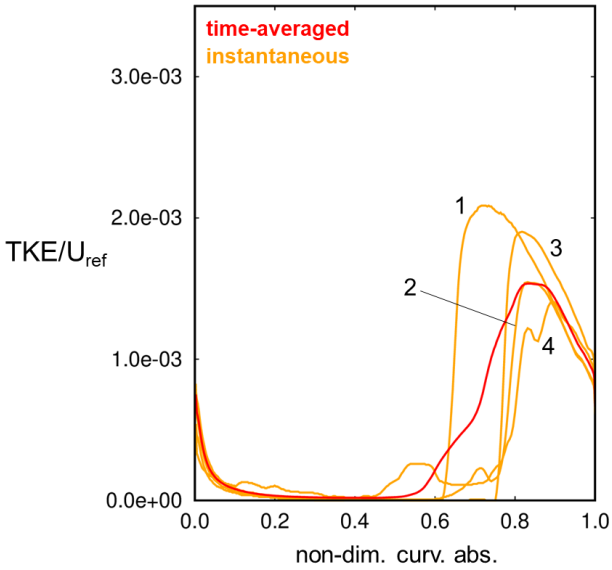

Figure 4.44: OPT-U: time-averaged and instantaneous distributions of TKE/U_{ref} over the stator suction side length

At instant 1, the wake turbulence triggers the transition at the 60% of the blade, and then the TKE reaches the maximum value. The distribution related to instant 2 intersects the calmed region as the low TKE region between the 60% and the 75% of the suction length proves. Downstream of that location, the TKE steeply rises since the non-wake induced transition occurs.

At instant 3, the turbulence is equal to zero up to the 75% of the blade, where the natural transition is triggered immediately downstream of the region characterized by the incipient separation. Finally, the TKE distribution related to instant 4 has the trace of the incoming wake over around 55% of the blade length. Then, the flow transitions over the last 20% of the blade.

The current curve describes a border region between the wake and the incipient separation, and therefore it looks perturbed.

In conclusion, Figure 4.45 shows the time-averaged and the instantaneous distributions of H. The curves concerning instants 1 and 3 describe a similar behavior of the boundary layer, even if the transition is delayed in the latter.

By contrast, at instants 2 and 4, the shape factor reaches high values which are in accordance with the condition of incipient separation. Moreover, at instant 2, the correlations adopted to evaluate H (paragraph 4.2.1) fail where the curve shows a plateau as the flow is in a critical state even if the transition onset (Figure 4.44) is located slightly downstream.

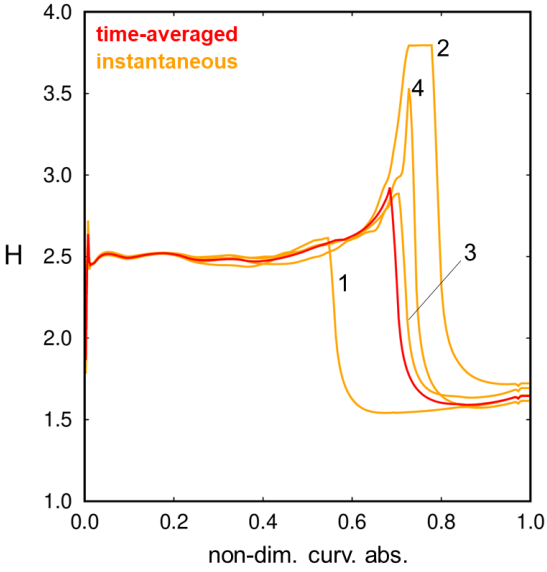

Figure 4.45: OPT-U: time-averaged and instantaneous distributions of H over the stator suction side length

4.5 Comparison between Steady and Unsteady Optima

The cpt values reported in Figure 4.14 and Figure 4.30 refer to different numerical setups since they are evaluated via steady and unsteady simulations, respectively. Therefore, a fair comparison must be performed by adopting the same setup, which corresponds, in this case, to the unsteady one as it is the most accurate.

Figure 4.46 shows the computational cloud concerning the unsteady database with the related ANN optimal set (set-U) and the OPT-U. Besides, the most promising geometries obtained through the steady approach (i.e., a subset of ANN-lb in Figure 4.15) are simulated via URANS calculations. The related results denoted by the blue (set-S) and violet (OPT-S) triangles are superimposed to the present graph. In this frame, the benefit guaranteed by the latter geometries turns out to be smaller than that gained in the steady analyses. In particular, the cpt difference between the OPT-S and the baseline is around -0.16% for the URANS calculation and -0.31% for the RANS one. However, the performance of the set-S geometries is still higher than that of the baseline, and the relative gain for OPT-S is about 3/4 of that for OPT-U. In other words, set-S is a kind of extension of set-U in a design space region where the values of g are smaller.

On the other hand, this plot shows the intrinsic limit of the optimization based on the steady approach: it is not able to detect the optimal configurations at higher values of g. This fact depends essentially on two reasons. The first one concerns the number of non-converged simulations that is noticeably higher

for RANS in the considered design space region. The second one, instead, regards the performance evaluation. Since steady calculations do not solve unsteady phenomena, their positive effects on performance, which are assessed by URANS simulations, are neglected this time. Therefore, at higher values of g, the steady database has a lower amount of data, and the losses related to these geometries are higher than the actual values. As a consequence, the ANN trained on the steady database does not locate the optimal set close to OPT-U.

Indeed, it is worth noting that the RANS simulation of OPT-U assesses a cpt value equal to -0.13% with respect to the (steady) baseline one. Such a cpt reduction is about 40% of that guaranteed by OPT-S under steady conditions (Figure 4.15), and consequently, the geometry of OPT-U is not detected by the ANN in the steady approach. The same explanation may be applied to the other set-U geometries.

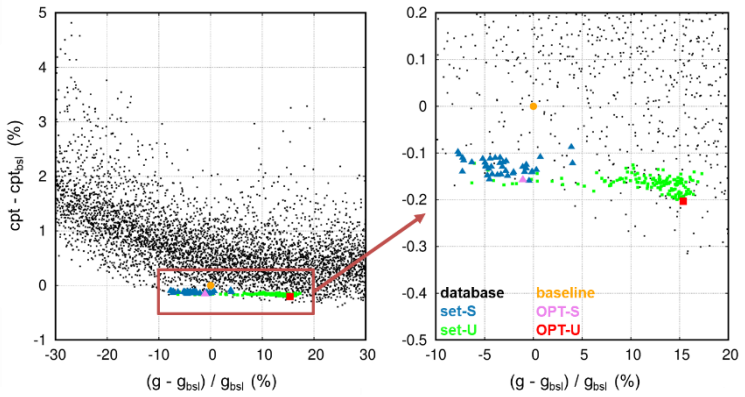

Figure 4.46: Unsteady calculations. Computational cloud and optimal set: cpt vs. g with respect to the baseline

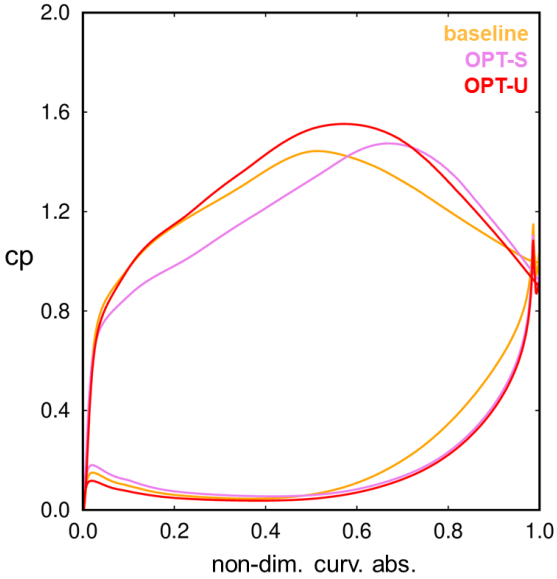

Figure 4.47: Unsteady calculations. Comparison of time-averaged cp distributions over the stator blade length

Moving forward, Figure 4.47 shows the cp for the three geometries. Differently from above, the cp is evaluated by considering the static pressure at the stator row exit instead of its value at the blade trailing edge. As a consequence, the cp value is not equal to 1 at the right edge of this graph. This choice allows observing the effect of the UGT increase for both the optimum geometries. Likewise, the differences about the diffusion region are directly comparable: the suction peak position for OPT-S induces a steep deceleration over a distance, which is much shorter than that for OPT-U. As far as the pressure side is concerned, the cp distributions over the two

optimum airfoils are nearly superimposed in the second half while some differences are observable in the first 30% of its length.

4.5.1 Reduced Frequency Effects

The other aspect, which must be addressed to perform a fair comparison between the two optimum geometries, concerns the reduced frequency ($\bar{f}$). As explained in paragraph 2.2, this parameter is fundamental to characterize the unsteady effects. Therefore, the decision of excluding it from the optimization DoFs might seem illogical. However, it is due to practical reasons concerning the industrial design process. Indeed, the present method is developed for the earliest phases of the design, while the blade count of rows depends on several multi-disciplinary constraints and specifications. As a consequence, any of the feasible values of $\bar{f}$ might be adopted for this analysis since the actual one is unknown at the considered design stage.

In this frame, the adopted configuration, in which $\bar{f}$ changes as g varies, has been chosen by pursuing the lowest level of computational cost. In particular, as the rotor pitch is always equal to that of the stator and the flow coefficient and the rotor chord are kept constant, the $\bar{f}$ turns out to be a function of g, only. As a result, the unsteady analysis of OPT-U is performed at a lower $\bar{f}$ than those for the baseline and OPT-S, which essentially have the same values of g and consequently $\bar{f}$.

The adopted strategy to vary $\bar{f}$ concerns the change of the blade gap of the rotor rows, while the stator pitch is kept constant in

accordance with the value obtained via the optimization process. The ANN is used to generate rotor profiles that guarantee the original deflection at the required gap. To do this, the setup described in paragraph 4.1 is adopted with the additional constraint about the pitch size. It is worth noting that this method is extremely lean in the frame of this work. However, it does not allow investigating the effects of much lower or much greater values of $\bar{f}$ since they would require g values that are out of the considered design space or even unfeasible. Moreover, URANS analyses would not accurately model the interaction between wakes that occurs out of the blade passage if $\bar{f}$ is sufficiently high. Such interaction results in increased background turbulence entering the vane rather than periodic incoming disturbances, and such mechanism proves to significantly affect the transition dynamics, and thus on the aerodynamic losses [20].

It is worth noting that the gap alteration would be sufficient to perform a steady analysis since the modeled rows are not required to have the same circumferential gap. By contrast, in full-annulus unsteady analyses, the entire rows must be simulated. Alternatively, row fractions characterized by the same gaps may be modeled to reduce the computational costs. Therefore, if the considered rows do not have the same blade pitch, a different blade count for each one must be included in the computational domain.

The details of the configurations adopted to evaluate the impact of $\bar{f}$ on the aerodynamic performance are reported in Table 1. For the three considered airfoils, the number of simulated blades for the rotor rows (ROT) and the stator one (STA) are listed as well as the related $\bar{f}$. It is worth noting that the two rotors have the same blade count. It allows maintaining the same

frequency for both the wake and the potential disturbance as the pitch changes. Moreover, the name of the reported conditions refers to the baseline case. Consequently, while the design conditions for the baseline and OPT-S coincide with that condition labeled as nominal in the present analysis, the design condition for OPT-U is referred to as low. The original configurations associated with the pitch ratio equal to 1 are colored in red for the sake of simplicity.

	CONDITION	$\bar{f}$	ROT	STA
BASELINE	low	1.05	7	8
	nominal	1.20	1	1
	high	1.43	6	5
OPT-S	low	1.04	6	7
	nominal	1.21	1	1
	high	1.45	6	5
OPT-U	low	1.04	1	1
	nominal	1.18	8	7
	high	1.45	7	5

Table 1: Investigated configurations for the $\bar{f}$ sensitivity analysis. Blade number of ROT(=rotors) and STA(=stator)

The results of the CFD analyses in terms of cpt are reported in Figure 4.48. For all the three blade profiles, the increase in wake frequency induces a beneficial effect on the losses, which is larger by switching from the lowest $\bar{f}$ to the middle one than from the middle value to the highest one. However, the different sensitivity to $\bar{f}$ is clearly observable: OPT-S is severely affected by such a parameter, while the impact on OPT-U is almost

halved. The sensitivity to $\bar{f}$ for the baseline is similar to that of OPT-U.

The physical reasons behind such performance trends are observable via the following s-t plots of cf and $Re_{\theta,t}$. Figure 4.49 and Figure 4.50 refer to the baseline blade profile. The different dynamic of the transition process is apparent for the three conditions. At the conditions labeled as low and nominal, the pattern is similar, while the magnitude of the wake-blade interaction remarkably changes. Indeed, the wake-induced transition starts upstream for the lowest $\bar{f}$, and the related turbulent region is wider. Likewise, along the path between the wakes, the non-induced transition occurs in the two cases with a slight difference in the extension of the turbulent area. That difference is limited by the greater effectiveness of the calmed region for the condition "low".

At high $\bar{f}$, the scenario remarkably changes: the boundary layer state becomes more and more uniform so that the trace of the wake-induced transition reduces. Indeed, it is triggered well downstream of the suction peak. In particular, the wake-induced transition onset is close to that of the non-wake-induced transition. The region of incipient separation becomes wider, while the extension of the calmed region decreases.

On the other hand, the $\bar{f}$ increase proves to be detrimental for the separation bubble on the pressure side, which grows in size and persists more in time. However, the flow-field over the remainder of the pressure surface becomes more uniform by increasing $\bar{f}$.

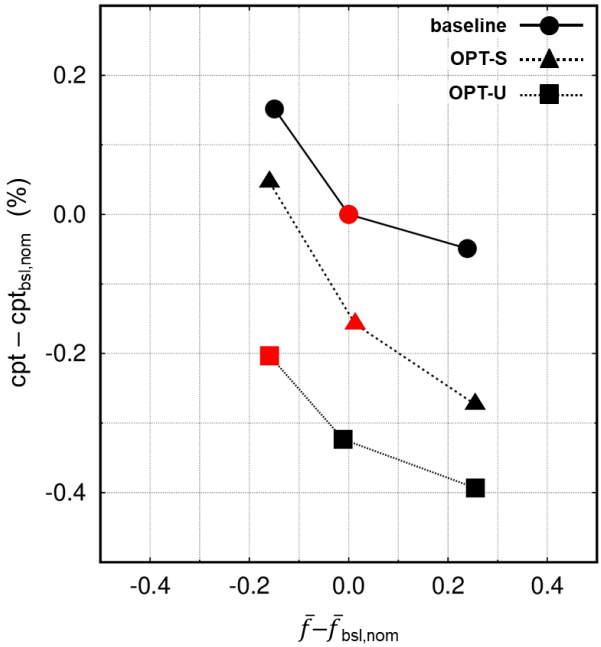

Figure 4.48: Reduced frequency effect on cpt. The red symbols mark the design configurations for each case

Analogous considerations are valid for OPT-S and OPT-U, even if the effect on the former is taken to extremes. At low $\bar{f}$, the wake-induced transition is absolutely predominant and influences a very large region: the wedged shape area in Figure 4.51 and Figure 4.52. The non-wake-induced transition starts far downstream on the rear part of the suction side. By contrast, at high $\bar{f}$, the boundary layer over the suction side is predominantly laminar. Indeed, the turbulent region occupies just the last 15-20% of its length. Moreover, a wide and

persistent region of incipient separation is observable over around the 75% of the suction side length.

Figure 4.53 and Figure 4.54 refer to OPT-U. The transition pattern turns out to be more similar to the baseline than to OPT-S. It is also proved by the similar sensitivity to $\bar{f}$ of their cpt (Figure 4.48). However, the cf level is lower, while that of $Re_{\theta,t}$ is higher. These aspects are in accordance with the considerably lower value of cpt and highlight that the flow-field has a larger laminar fraction.

The performance change with $\bar{f}$ is mostly due to the different extent of the turbulent regions over the suction side. In turn, it is mainly caused by the different wake-induced transition dynamic occurring at different $\bar{f}$. It is worth noting that the increase in pitch determines a higher TKE production within the wake segments along the blade passage. It results in more intense interaction with the blade boundary layer, which becomes thicker as well as the blade wake does. Moreover, the wake TKE level increases, and thus, the impact on the downstream blade is larger.

In conclusion, it is apparent that the influence of the $\bar{f}$ cannot be neglected for the purpose of comparing different geometries under the same operating conditions. Consequently, the following results about OPT-U refer to the condition of nominal $\bar{f}$, which is essentially equal to the design value for the baseline case.

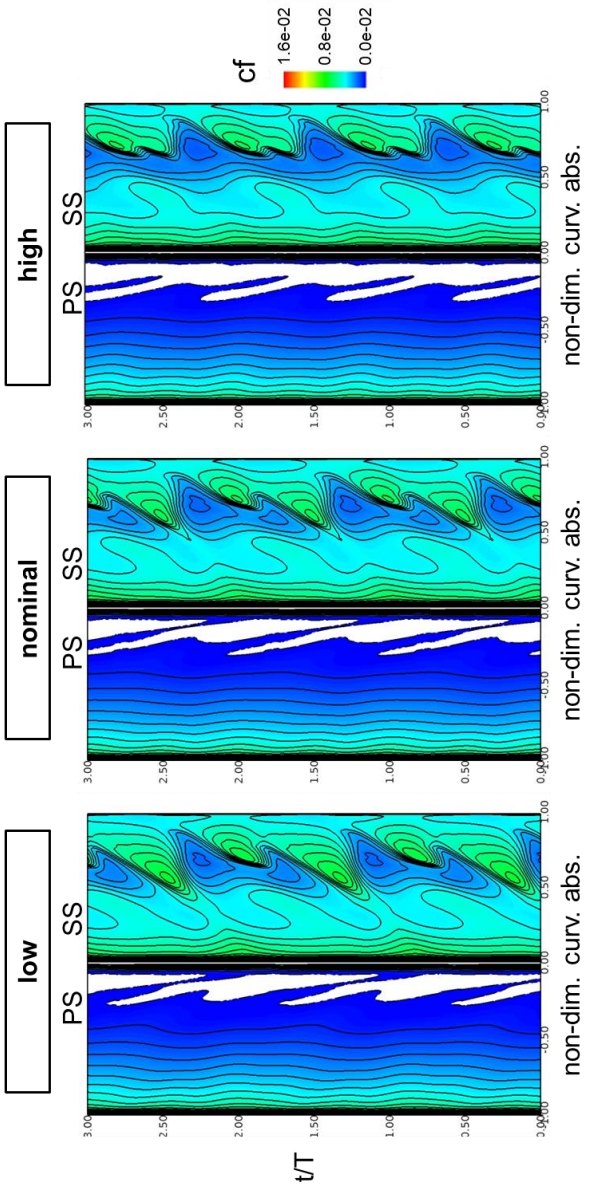

Figure 4.49: Baseline: Space-time plots of cf over the stator blade surface

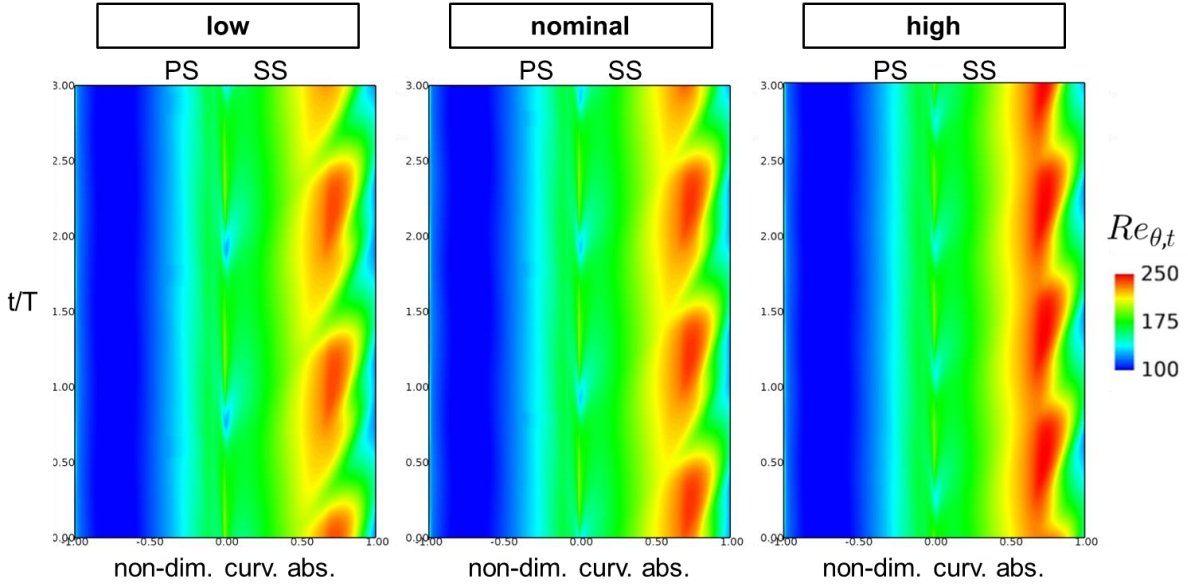

Figure 4.50: Baseline: Space-time plots of $Re_{\theta,t}$ over the stator blade surface

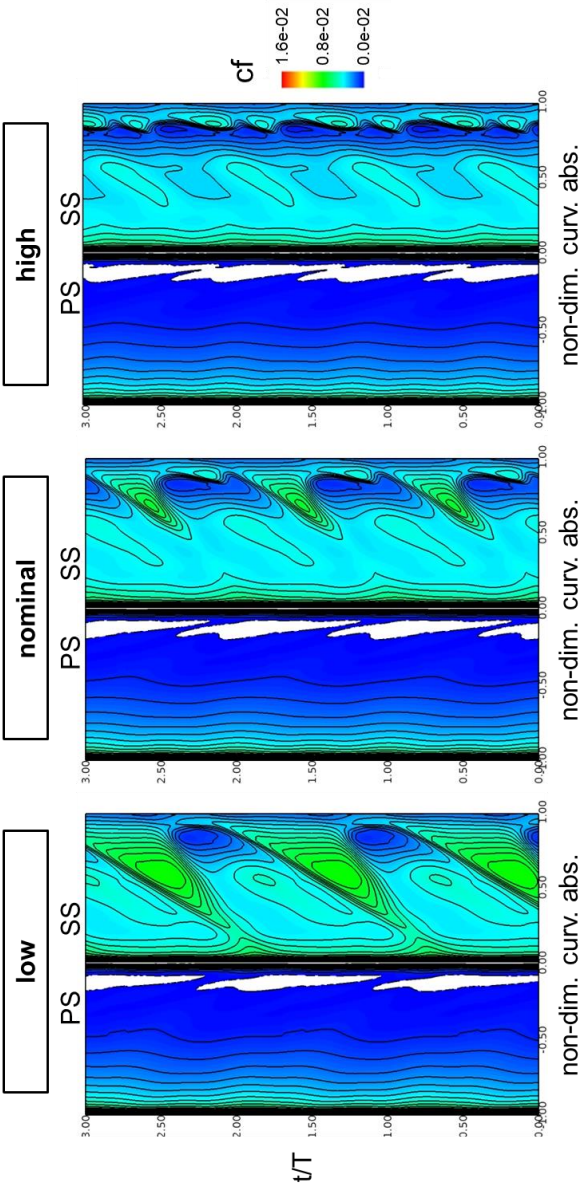

Figure 4.51: OPT-S: Space-time plots of cf over the stator blade surface

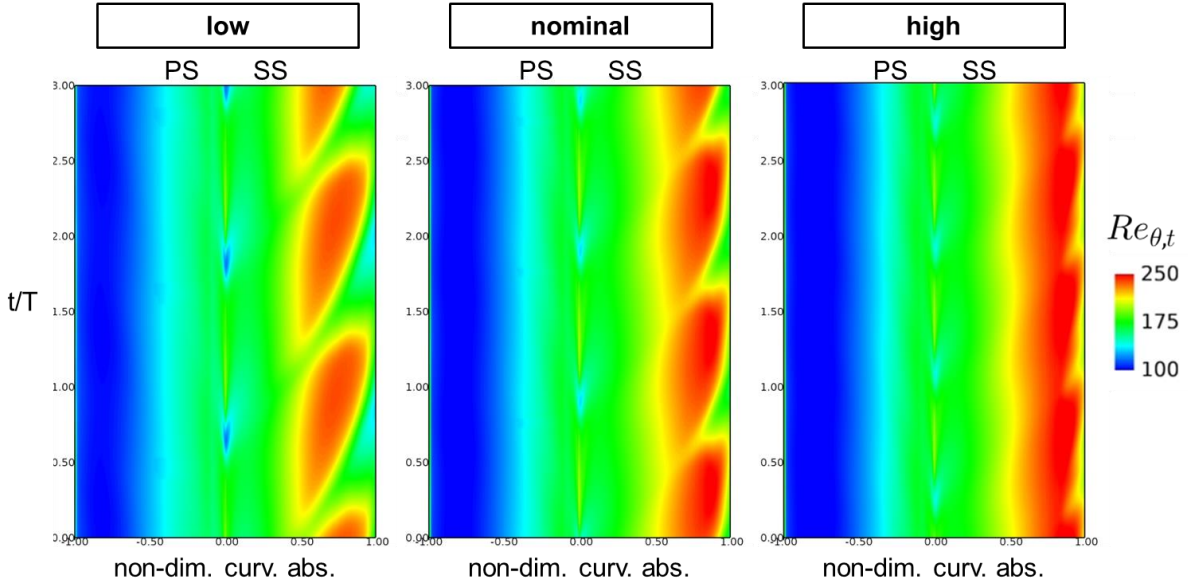

Figure 4.52: OPT-S: Space-time plots of $Re_{\theta,t}$ over the stator blade surface

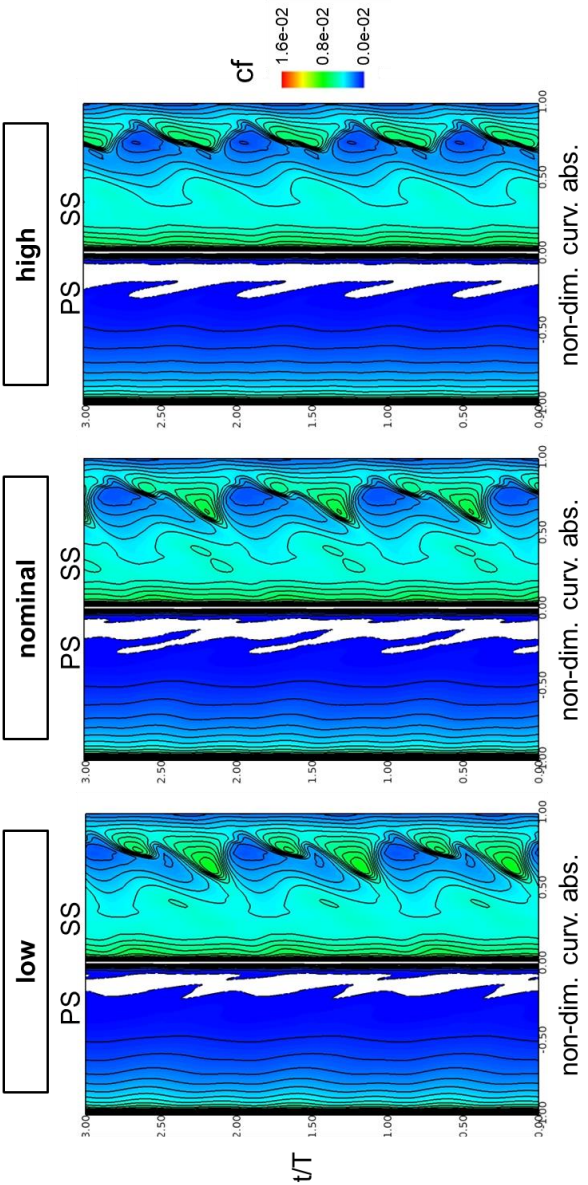

Figure 4.53: OPT-U: Space-time plots of cf over the stator blade surface

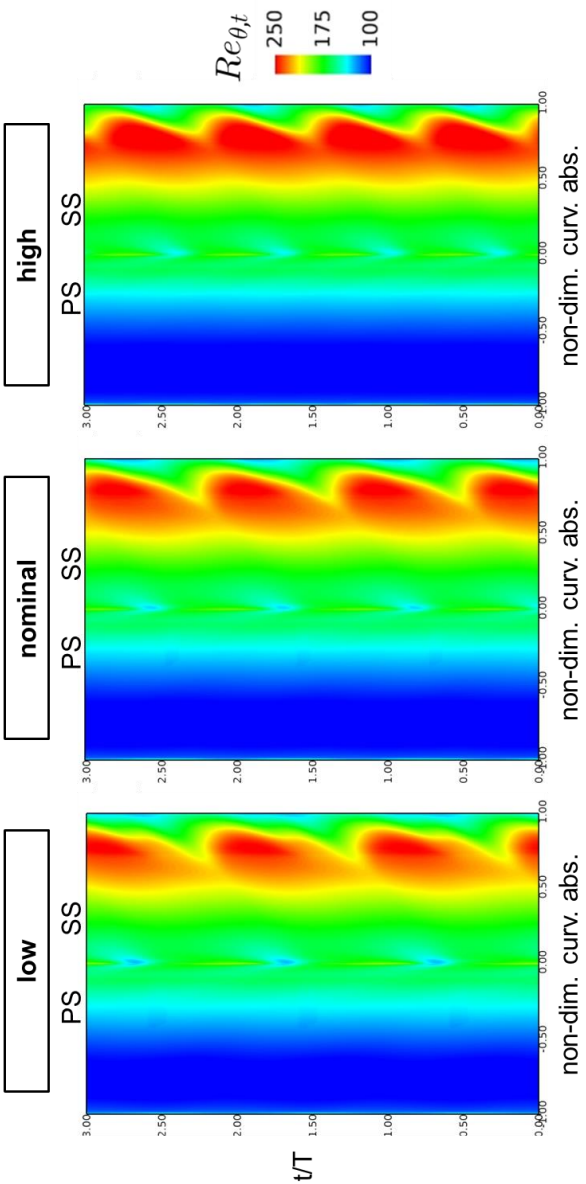

Figure 4.54: OPT-U: Space-time plots of $Re_{\theta,t}$ over the stator blade surface

4.5.2 Reynolds Number Effects

The last analysis carried out in the present work concerns the impact of Re on aerodynamic performance.

The considered range, which varies between 100k and 300k, corresponds to that in which cascade tests are usually performed. The cpt values for each of the three considered configurations are reported in Figure 4.55 with respect to the result of the baseline under nominal conditions. All the present CFD simulations are performed via the URANS method.

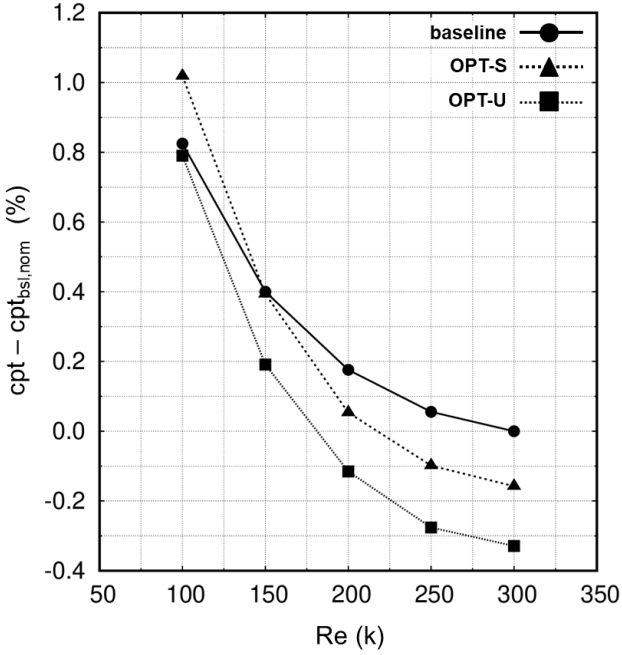

Figure 4.55: Unsteady calculations. Re effect on cpt

At high Re, the performance variation is essentially the same for the three blade profiles, while it changes under Re=250k: the baseline blade shows higher robustness than that of the others. Indeed, the change in curve slope is clearly observable at Re=200k for OPT-S and at Re=150k for OPT-U. As a consequence, the latter experiences a lower detrimental effect by reducing the Re than that of the former. Moreover, at the lower bound of the considered range, the cpt for OPT-U is essentially equal to that for the baseline case, despite the greater decay. In other words, the performance gain for OPT-U is preserved over most of the considered range of Re. On the other hand, the performance penalty for OPT-S at Re=100k turns out to be greater than the benefit at the upper bound of the considered range.

The Re effect may be observed in terms of blade loading in the following graphs. Figure 4.56 shows the time-averaged cp distributions over the baseline blade surface. No variations are noticeable between the curves at Re equal to 300k and 200k, while some alterations are observable around the 80% of the suction side length and at about the 20% of the pressure side one. Both are related to separation phenomena.

These effects are also observable in Figure 4.57, but their magnitude is much greater, especially over the suction side distribution. Indeed, the plateau corresponding to a short separation bubble is apparent, and its impact is observable even beyond the suction peak towards the leading edge. Moreover, a small cp alteration is already present at about the 80% of the suction side for Re=200k.

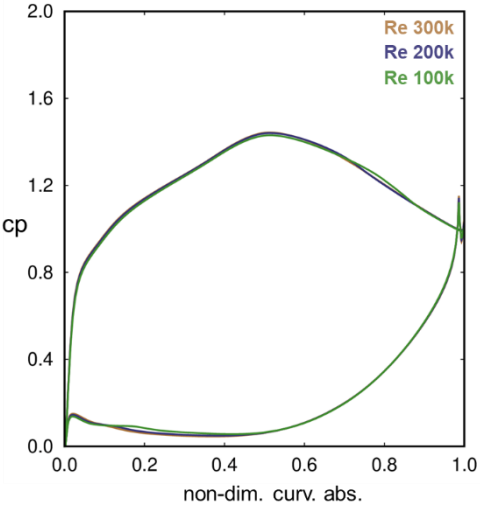

Figure 4.56: Baseline: Reynolds number effect. Time-averaged cp distribution over the stator blade length

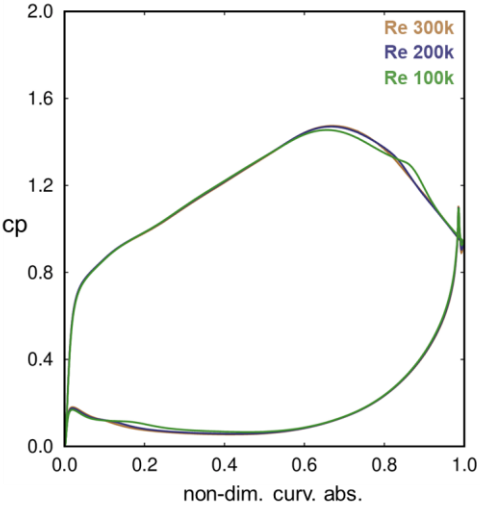

Figure 4.57: OPT-S: Reynolds number effect. Time-averaged cp distribution over the stator blade length

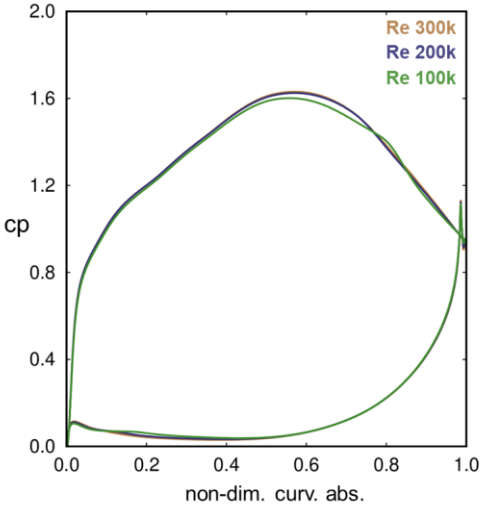

Figure 4.58: OPT-U: Reynolds number effect. Time-averaged cp distribution over the stator blade length

Finally, Figure 4.58 shows the time-averaged cp distributions for OPT-U. A short separation bubble is present at about the 70% of the suction side length, and the distribution is affected up to the 40% of it. Some minor effects are also detectable on the pressure side around the 20% of its length. By contrast, no effects are observable at Re=200k.

The flow-field evolution over time for the three blade profiles is observable in the following plots. At each considered value of Re, s-t plots of cf and intermittency (γ) are reported. It is worth noting that the latter is evaluated out of the laminar sublayer, at a distance from the wall, which is equal to half of the boundary layer thickness. γ allows promptly detecting the fully laminar and fully turbulent regions regardless of the adopted

Re. By contrast, $Re_{\theta,t}$ is significantly influenced by that value, and therefore it is not shown herein.

Figure 4.59 and Figure 4.60 refer to Re=300k, which corresponds to the nominal condition. The latter plot clearly shows that the turbulent region is larger for the baseline case. Besides, for OPT-S the wake influence is absolutely predominant as the difference between the path between the wakes and the wake-induced path is the most relevant. On the other hand, the extent of the turbulent region for OPT-U experiences a lower variation over the blade passing period. In summary, these considerations confirm the results of the analyses above.

The most apparent effect on the s-t plots of cf, caused by the reduction in Re, concerns the laminar boundary layer over the front part of the suction side. A lower Re determines higher viscous effects, and thus the cf locally increases.

The s-t plots in Figure 4.61 and Figure 4.62 refer to Re=200k. The patterns over the suction side for the baseline and OPT-U look similar, even if the latter experiences a lower level of cf, especially in the diffusive region. Consequently, the turbulent region is smaller, even if it is more persistent over time. The wake-induced and the non-wake-induced transitional modes are clearly observable in both cases. Likewise, the incipient separation area is present, and it is larger than that at nominal conditions. However, it is worth noting that the highest cf values are associated with the flow-field between the wakes. The situation is then overturned with respect to that at Re=300k. This change in the transitional mode hierarchy may be explained by considering the lower effectiveness of the incoming wake turbulence in perturbing the laminar boundary layer as Re lowers (paragraph 2.5.2). This fact causes the wake-induced

transition onset to move downstream. Besides, the calmed region effectiveness is closely related to the intermittency values in the wake-induced path. As the local turbulent spots are less developed, the intermittency decreases. Consequently, the calmed region effectiveness in stabilizing the boundary layer lowers. Therefore, two opposite effects act on the boundary layer transition mechanism between the wakes: the reduction in Re and the lower calmed region effectiveness.

Moving forward, the s-t plot of cf about OPT-S shows small separation bubbles over the diffusive part of the suction side. The considerations concerning the other two profiles are still valid as the size of the two separation regions proves. Indeed, the largest one is located where the wake-induced transition develops at Re=300k, while the smallest occurs in the region of incipient separation at nominal conditions. In other words, the separation bubble is suppressed as the wake turbulence triggers the transition process over its shear layer. Due to the adverse flow-field conditions, the bubble originates again and develops until it is suppressed again because of the potential effect. Indeed, when the leading edge of the downstream rotor is closer to the stator trailing edge (for example t/T=1), the inflectional boundary layer is altered so that the transition process starts on the bubble shear layer and the flow reattaches. As a consequence, the fully turbulent region shown in the figure develops.

The potential effect is even more apparent at Re=100k since the incoming wake impact furtherly decreases. The related graphs are reported in Figure 4.63 and Figure 4.64, which show the s-t plots of cf and γ, respectively. A separation bubble is observable in all the suction side distributions. However, its behavior is significantly different. In the baseline case, the boundary layer

separates after the wake passage and then reattaches in transitional state when the downstream rotor passes inducing the maximum potential effect. OPT-S experiences the presence of a steady bubble over the rear part of the suction side. The unsteady effects modulate its size, but the flow never reattaches. Besides, the potential effect looks much stronger than that due to the wakes. This consideration is also valid for OPT-U, in which the separation bubble is shorter so that the potential effect succeeds in suppressing it. However, it immediately originates again.

It is worth noting that under these conditions, the boundary layer state never becomes fully turbulent over the suction side of all the considered blade profiles. Moreover, it is quite far from that state in the baseline case.

Finally, the Re effect on the pressure side may be observed by comparing all these plots. Two aspects are particularly affected by the Re decrease: the increase in cf over the last 40% of the pressure side length and the development of the bubble separation over the front part of the blade.

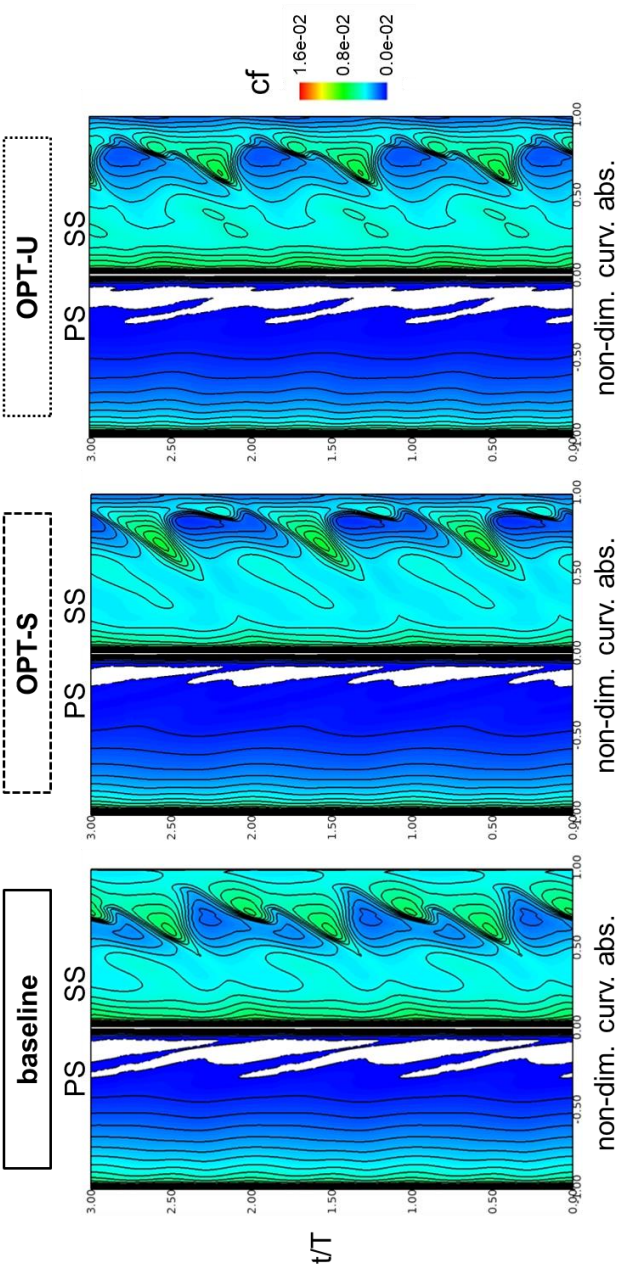

Figure 4.59: Re=300k. Space-time plots of cf over the stator blade surface

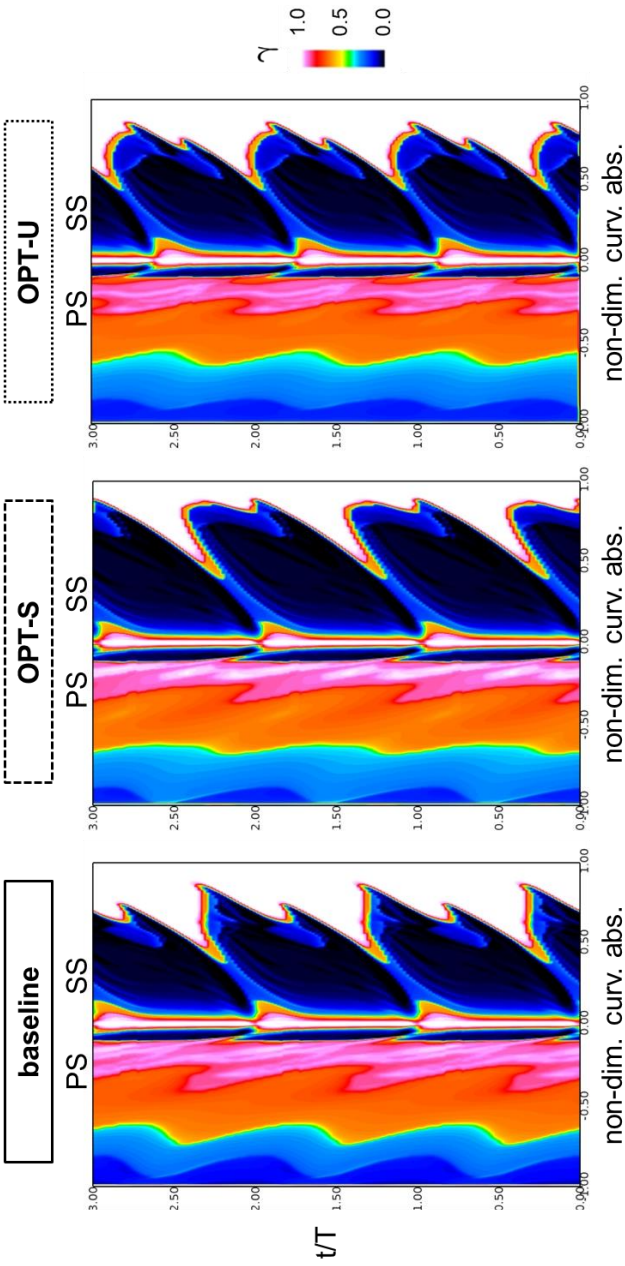

Figure 4.60: Re=300k. Space-time plots of γ over the stator blade surface

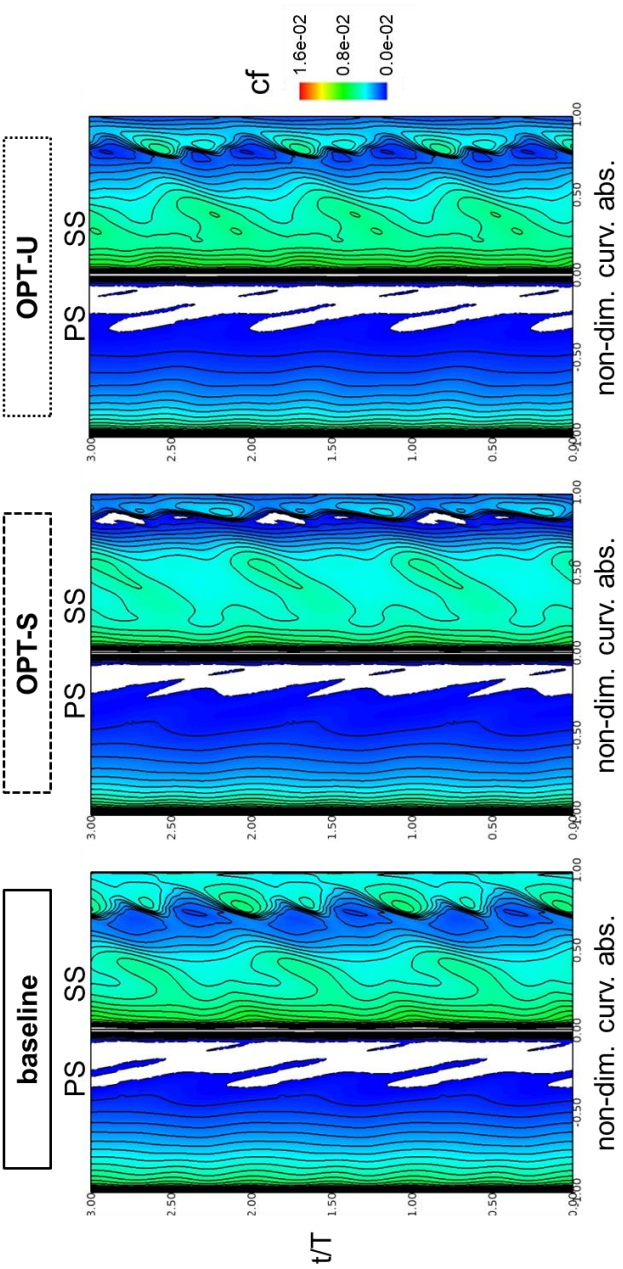

Figure 4.61: Re=200k. Space-time plots of cf over the stator blade surface

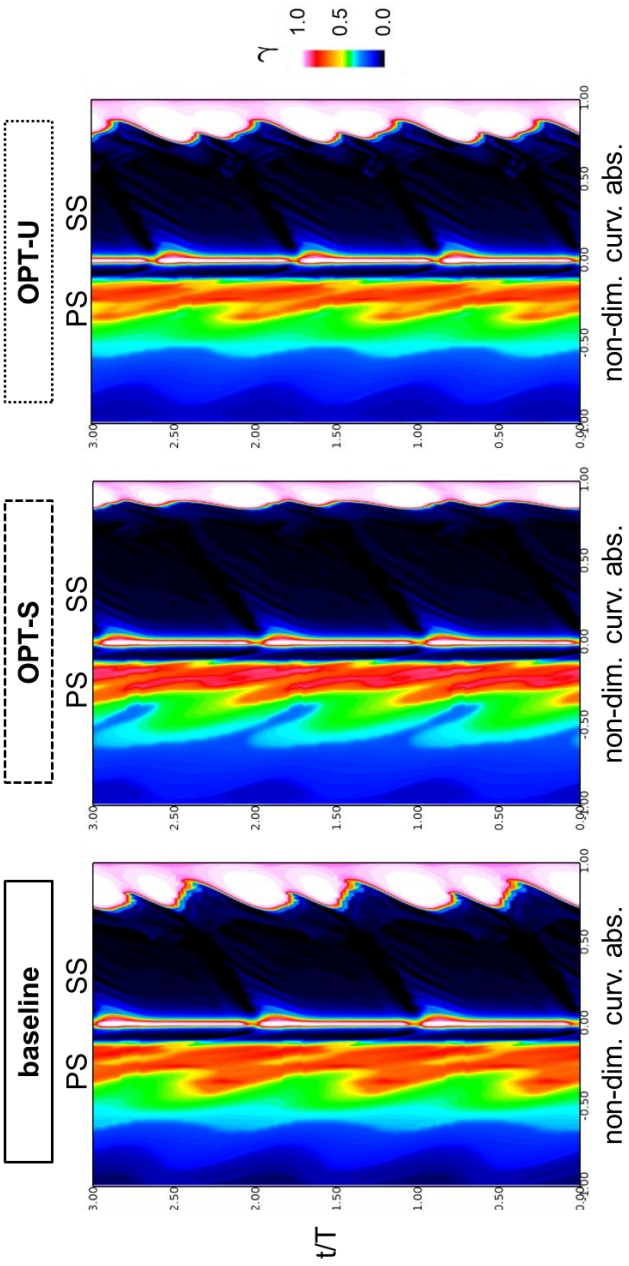

Figure 4.62: Re=200k. Space-time plots of γ over the stator blade surface

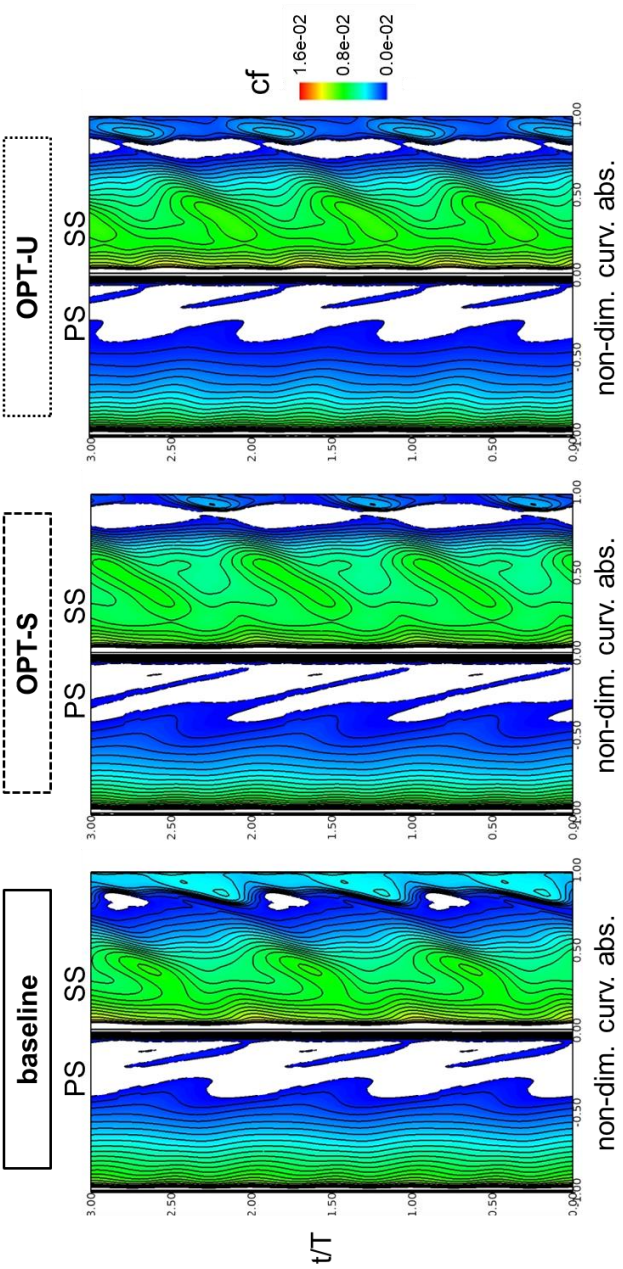

Figure 4.63: Re=100k. Space-time plots of cf over the stator blade surface

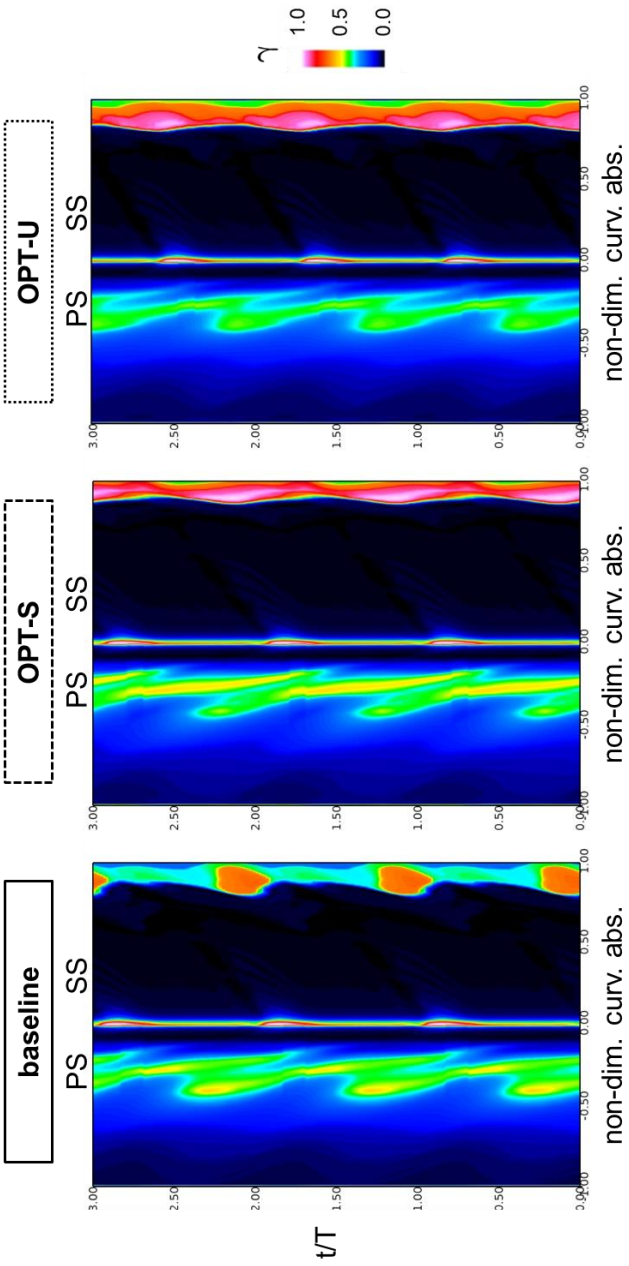

Figure 4.64: Re=100k. Space-time plots of γ over the stator blade surface

5 The Blade Fences

The secondary flow mitigation is a longstanding issue for Low-Pressure Turbines, and its importance is even rising due to the adoption of high-lift profiles that enhance the intensity of the endwall flows. Several strategies for reducing the secondary losses are proposed in literature as reviewed in [159]. Generally speaking, these strategies may be divided into two groups. The first concerns the three-dimensional design of blades [160] or endwalls [161] to hinder the secondary flow generation by undermining the driver mechanisms. By contrast, the second family includes the devices aimed at reducing the impact of the endwall flows on the aerodynamic performance [162].

However, the present chapter concerns a new type of passive device, referred to as blade fences (or just fences). They consist of shelf-like extrusions of the blade surface, located close to the endwall. This device does not belong to any of the aforementioned groups, but rather it is placed in between the two. Indeed, the blade fences are aimed at both hindering the secondary flow drivers and reducing the related aerodynamic loss. It is worth noting that the adoption of blade fences in a row not only induces the loss reduction of that row but also determines the performance improvement of the downstream row. This feature is called carry-over effect: the reduction in the flow under- and over-turning at the vane exit. Since the flow-field entering the downstream passage is more uniform, the aerodynamic performance of that row increases.

Even if similar devices have been already presented in literature [163], there are significant innovations in terms of geometry, objective and effects so that these blade fences have been recently covered by a patent of General Electric [164].

5.1 Design

The original design of blade fences is carried out in an embedded stage of a modern LPT of a large turbofan operating in conditions that are compatible with the "aero-design point" [9]. This choice comes from the necessity to represent the device effect on both the flow-field of the blade row where it is applied and the downstream one. Indeed, secondary flows not only reduce the aerodynamic performance of each row but also enhance the flow-field non-uniformity in the following passage. The secondary vorticity determines the increase of the mixing loss and alters the flow angles with respect to the design intent so that the downstream blades do not experience the optimal incidence along all the span, and their performance reduces (paragraph 2.4). Although the blade fences can be applied on both stator and rotor blades, the design process is carried out with the fences mounted on the stator blades only. This determines a lean framework for flow-field analysis and device optimization. In other words, this choice allows considering several degrees of freedom (DoFs) for the fence geometry and simultaneously limiting the computational costs.

The first step, preliminary with respect to the design process, concerns the parameterization of the fence geometry: it is

carried out via a lean in-house tool that describes a generic shape with 10 parameters (or DoFs).

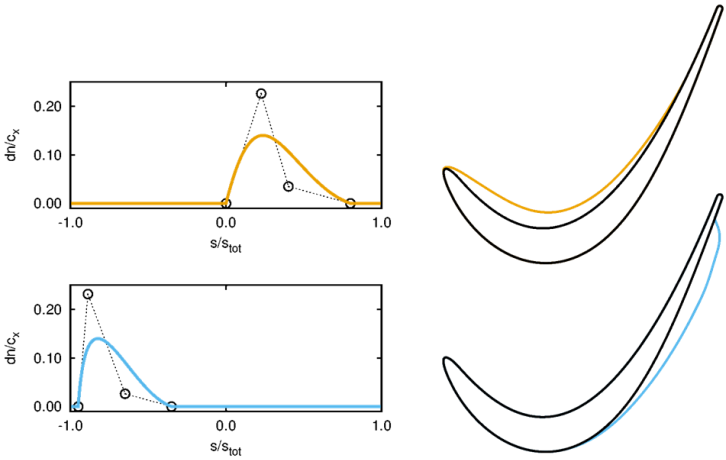

Figure 5.1: parameter space and B2B view of blades with fences over the pressure side (top) and fences over the suction side (bottom) [9]

The fence shape must be defined on both the B2B plane (Figure 5.1) and the meridian one (Figure 5.2). The geometry on the former is controlled through a B-spline with four control points that determine the starting and the ending points of the device on the airfoil perimeter and the thickness distribution: 7 DoFs act on these features. It is worth noting that the starting and the ending points are not constrained on the same blade side. Indeed, the design space also includes configurations that extend over the entire blade perimeter or others that start on the pressure side and end on the suction one (and vice versa). However, such configurations do not provide the best

performance in reducing secondary flows for the reasons explained in the following paragraph.

Differently, the fence geometry in the span-wise direction is controlled by 3 parameters, which are the distance of the first fence from the endwall, the number of fences and the overall width along the blade height. In other words, the latter is the distance in the span-wise direction between the starting point of the first fence and the ending point of the last one. In single-fence configurations, such overall width coincides with the fence height.

In light of this, the fence design is carried out via an optimization process over a 10 DoFs design space. Such a size makes the space exploration hard to perform without an effective strategy to select the most encouraging solutions. Therefore, Artificial Neural Networks (ANNs) are adopted for this task since they allow building a response-surface for each constraint and design objective. The adopted approach is similar to that described in [157]. In both the following optimization campaigns, two objective functions are considered. The vane total pressure loss coefficient (cpt) defined as:

$$cpt = \frac{p_{0,in} - p_{0,out}}{p_{0,in} - p_{out}} \tag{5.1}$$

and the stage total-to-total efficiency:

$$\eta_{tt} = \frac{h_{0,in} - h_{0,out}}{h_{0,in} - h_{out,is}} \tag{5.2}$$

It is worth noting that in the former equation, the subscripts *in* and *out* respectively refer to the inlet and outlet interfaces of the vane. By contrast, in the latter equation, such subscripts relate to the inlet and outlet interfaces of the stage.

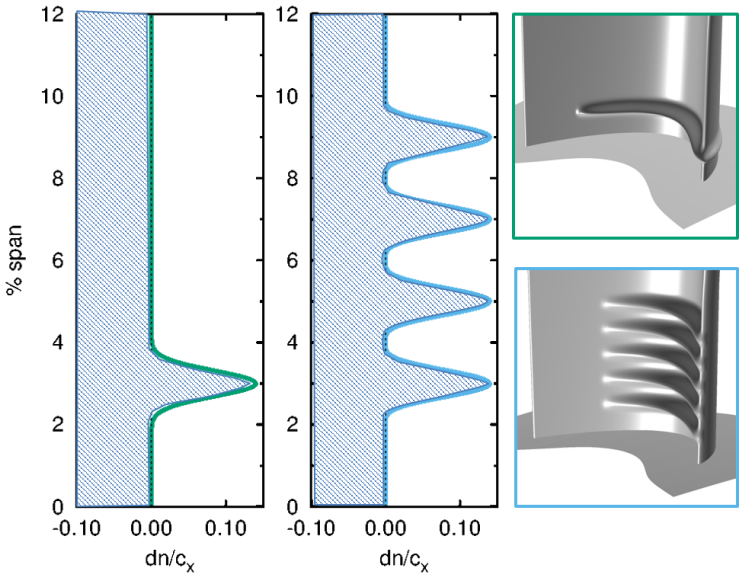

Figure 5.2: parameterization of span-wise blade surface [9]

First, a single fence is considered to select the optimal set of geometrical parameters. Then, the effect of a multiple-fence configuration is evaluated by varying the number of mounted devices.

For brevity, the computational setup adopted for the CFD analyses concerning the fence optimization process is not described herein; however, such information is available in [9].

5.1.1 Single-Fence Configuration

This optimization campaign is performed to determine the optimal value of 9 of the 10 parameters introduced before as the number of devices is kept equal to 1 at this stage.

Initially, the starting and ending points of the blade fence do not have constraints in the B2B plane. In other words, their location may occupy any point of the blade perimeter at the considered blade height. Since the configurations in which the device surrounds the entire blade or covers a large portion of it (in the B2B plane) provide worse performance than those in which the fence occupies a smaller perimeter fraction, some constraints are applied to make the design space leaner. In particular, two separate sub-campaigns are designed. In the first one, the blade fence is limited to the suction surface. While in the second one, the device is constrained to the pressure surface.

Figure 5.3 shows the related computational clouds: the left graph concerns the first sub-campaign, and the right one relates to the second one. Each grey dot corresponds to the CFD result for a given geometry, the black dot refers to the straight blade, and the coloured dots indicate the optimal configurations for the two sub-campaigns.

These graphs simultaneously allow evaluating the fence effect on the row where the device is applied and the impact on the downstream row. The latter aspect is assessed through the stage efficiency value. Both the η_{tt} and cpt are expressed with respect to the homologous values for the straight blade configuration.

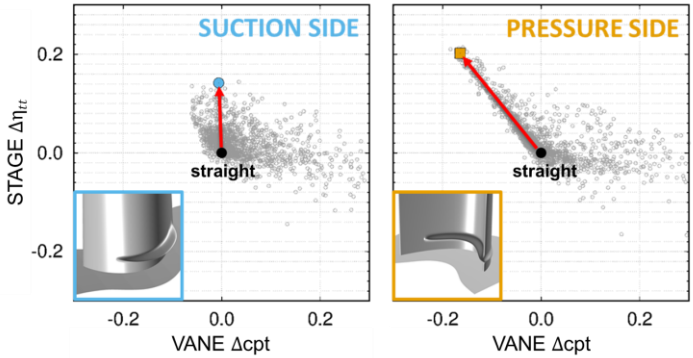

Figure 5.3: Stage efficiency vs. blade row loss: fences mounted over the a) suction surface, b) pressure surface [9]

It is apparent that the device applied on the suction surface determines a beneficial effect on the downstream row (i.e., the stage efficiency improves), but the vane loss remains constant. By contrast, the device onto the pressure side simultaneously leads to a reduction in stator loss and an increase in stage efficiency.

Indeed, the fence applied on the suction surface results in an obstacle for the radial flow migration, which causes the under- and over-turning mitigation. On the other hand, the device applied on the pressure side directly interacts with the secondary flow driver mechanisms. In particular, the streamline deflection towards the suction side reduces so that the passage vortex development is hindered. As a consequence, not only the flow-field at the downstream passage inlet becomes more uniform but also the vane loss decreases since a lower amount of low-momentum fluid is transported from the endwall

boundary layer towards the blade suction side. In addition, the presence of the fence around the leading edge determines a variation of the radial distribution of stagnation pressure and results in an obstacle for the radial flow migration. Since they are the driver mechanisms of the horseshoe vortex, its size and its negative effect diminish. As the device is present even in the front part of the pressure side, it also hinders the pressure-side-leg of the horseshoe vortex. Consequently, the low-momentum fluid migration reduces and the intensity of the vortical structures acting over the suction side (above all the horseshoe and the passage vortices) furtherly decreases. For this reason, the optimal fence shape in the B2B plane starts on the suction side close to the blade leading edge and develops along the pressure side.

It is worth noting that the device length does not depend on a specific constraint, but it is determined by the trade-off between two loss mechanisms: the viscous dissipation on the fence solid surface and the secondary loss. The optimization process determines the fence shape so that the local increase in viscous loss is overcome by the beneficial impact on the secondary loss. In other words, a longer fence would result in lower performance with respect to the optimum as the additional wetted surface would be placed in a region where it does not affect the secondary flows, and consequently, only the viscous loss would increase.

In light of this, only the configurations in which the fence is applied on the blade pressure side are considered in the following.

Figure 5.4 shows the remarkable influence of the blade fence thickness on the aerodynamic performance: three Pareto fronts are highlighted and represent the optima in the trade-off

between the vane loss lowering and the stage efficiency increasing for three considered device thickness. It is worth noting that the fence benefit is halved by reducing its thickness from the 15% (orange dots) to the 5% (light blue dots) of the blade axial chord (C_{ax}). However, a further increase in fence thickness (beyond the 15% of C_{ax}) causes a detrimental effect on the performance as implicitly proven by the fact that the optimum, denoted by the orange square, belongs to the device set of thickness equal to 15% C_{ax}.

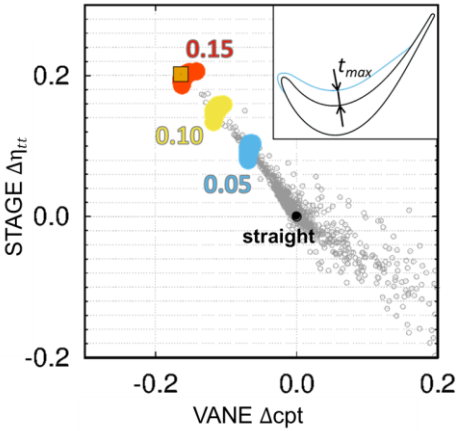

Figure 5.4: Impact of blade fence thickness [9]

5.1.2 Multiple-Fence Configuration

A second optimization campaign is carried out to investigate the effect of the number of fences. Therefore, the overall DoFs become 10 since the device count is added to the 9 parameters

of the previous campaign. However, the exploration range of those 9 DoFs is narrowed due to the assumption that the fence planform shape would not have remarkably changed from the first campaign optimum. In other words, this optimization campaign is mainly focused on determining the optimal number of devices and their span-wise location starting from the geometry of the first campaign optimum (i.e., that with the fence applied on the pressure side).

The optimization results are shown in Figure 5.5, where the coloured computational clouds refer to configurations with a different number of fences. The coloured labels allow connecting the number of devices with the corresponding set. Besides, the computational clouds are superimposed to the ANN results of the first campaign. The multiple-fence configuration looks beneficial with an additional 30% of stage efficiency gain with respect to the single-fence one (orange square). The optimum fence count is apparently 3 (red dots); however, the performance concerning the configurations with 2 (yellow dots) and 4 (light blue dots) devices is similar. A higher number of fences leads to the performance decreasing since there is no additional effect on the secondary loss while the profile loss furtherly increases. As a result, the optimal number of fences ranges from 2 to 4 depending on the blade geometry and the inlet boundary layer since they determine the flow-field in the near-endwall region. In addition, the geometrical parameters related to the planform shape do not remarkably change switching from the single-fence configuration to the multiple-fence one. That suggests that the adoption of independent DoFs for each device in the multiple-fence configuration would lead to a substantial increase in computational costs. By contrast, the advantage in terms of performance would be low.

Along the span-wise direction, the fences cover about the 10% of the blade height starting at about 1%. However, the number of fences and the peak position turn out to be much more relevant than the device shape in the span-wise direction. As a consequence, the latter may be selected following mechanical or manufacturing criteria.

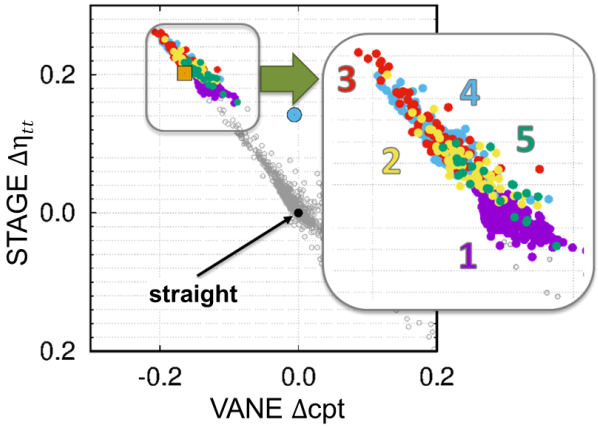

Figure 5.5: Multiple-fence configurations: impact of the number of devices [9]

In conclusion, the most relevant parameters and the related recommended values are summarized below. By considering the non-dimensional curvilinear abscissa normalized with the length of the blade pressure side, the optimal fence starts at -0.2 ÷ -0.1 and ends at 0.6 ÷ 0.9. The device thickness ranges between the 5% and the 15% of the blade axial chord. The number of fences may vary between 2 and 4.

5.2 Test-Case Description

The adopted blade referred to as "straight" in the following is selected in order to be representative of modern LPT high-lift profiles. Therefore, it is aft-loaded with smooth acceleration up to the throat and controlled diffusion downstream of it: high performance is guaranteed under unsteady conditions. Moreover, the pressure side is designed to limit the diffusion close to the leading edge and to determine proper acceleration towards the blade trailing edge. Indeed, the profile is the result of an optimization process aimed at minimizing profile losses. The main geometrical data and the blade loading are reported in Table 2 and Figure 5.6, respectively.

C_{ax} [mm]	AR	deflection [deg]	DF	Z	Re_{2is}
~100	3	100	0.7	1.3	300k

Table 2: Cascade data

More in detail, the latter shows the comparison of numerical and experimental data (provided by the Aerodynamic and Turbomachinery Laboratory of UniGE) about the distribution of pressure coefficient over the blade surface at the midspan. It is worth noting that the cascade is designed with 3D features: the blade chord increases near the endwall to locally increase the solidity, and consequently the loading decreases [165]. Moreover, the airfoil stacking (along the span-wise direction) is

realized by following the "snaked" pattern [162] to mitigate the under- and over-turning downstream of the blade TE.

In order to fit these cascade conditions, the blade fences are redesigned. Anyway, a new optimization process is not necessary since the parametric approach and the guidelines of paragraph 5.1 are sufficient to generate suitable devices for different applications. In particular, these fences are characterized by a smaller turning as the cascade constraints impose. A two-fence configuration is selected for two reasons. The first concerns the intensity of secondary flows, which is lower in the cascade environment than in the engine-like one. The second regards the manufacturing complexity, which obviously decreases as the number of devices reduces.

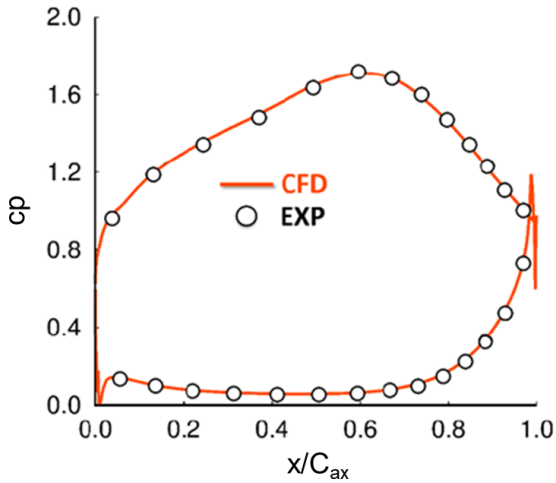

Figure 5.6: Blade loading

Figure 5.7 shows the blade geometry near the endwall, where the fillet with the hub surface is observable in addition to the two optimal blade fences. The geometrical details of the devices are quantitatively reported in Figure 5.8, which shows the parametric curves of the span-wise and the B2B shapes. In the span-wise direction, the fences are applied between the fillet and the 7% of the blade height. In the planform plane, instead, the devices start near the leading edge on the suction side ($s/s_{tot} = 0.2$), surround it and extend up to the 80% of the pressure side (negative values of the non-dimensional curvilinear abscissa).

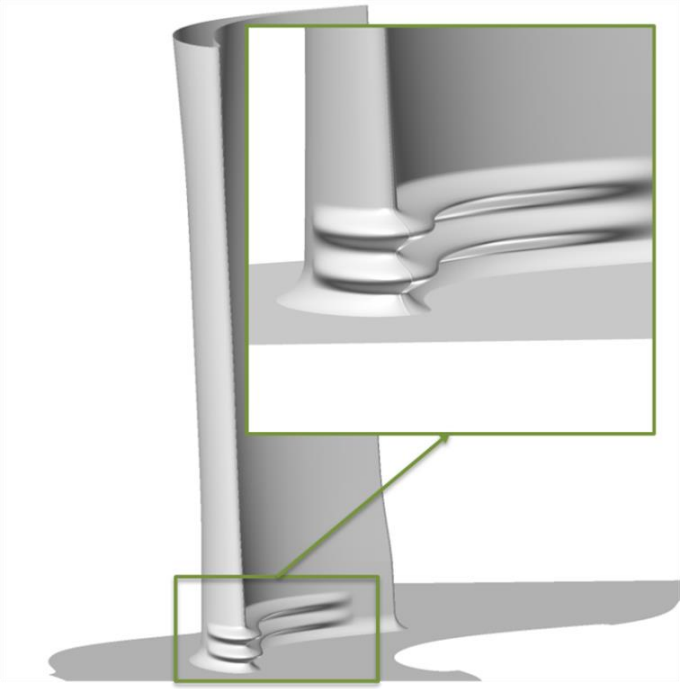

Figure 5.7: Geometry of the optimal blade fences

As already mentioned, the fence thickness plays a key role. It affects not only the aerodynamic performance but also the manufacturing, the weight, and mechanical properties of the devices. In light of this, two different configurations are built and tested. The "small fences" have a thickness equal to about 5% of the blade axial chord, while the "optimal fences" have a non-dimensional thickness of 15%. The latter value corresponds to the optimum obtained through the optimization process in the engine-like environment, and this explains the adopted label. The two configurations are displayed in Figure 5.9.

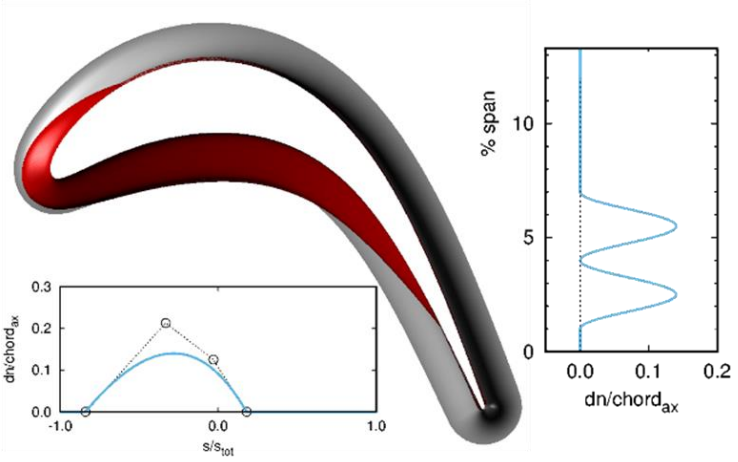

Figure 5.8: Details of the optimal blade fences

The procedure to manufacture the fences starts with the computational generation of the geometry: it is performed by morphing the straight blade (the process is furtherly explained in paragraph 5.3). Then, the obtained geometry is exported in

CAD format, where the fences are defined as additional volumes placed onto the straight blade surface (Figure 5.10, top left).

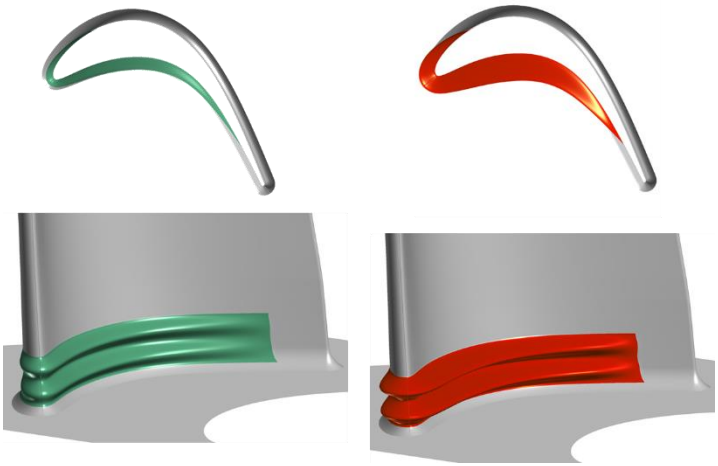

Figure 5.9: Visualizations of fenced blades: "small fences" on the left and "optimal fences" on the right.

The device manufacturing is carried out via rapid prototyping: six fences before the application onto the blade surface are shown in Figure 5.10, bottom left. Indeed, they are realized as an add-on for the straight blades. Such a decision allows reducing the costs of production and simplifying the experimental comparison between the straight and the fenced configurations with respect to the manufacturing of blades with built-in fences. In other words, the comparison is performed by testing the straight blade and then adding the devices to measure the properties of interest in the fenced configuration. This procedure improves the confidence of the comparison since

the rig setup and tuning are not altered, switching from one configuration to the other.

The experimental measurements are carried out at the Aerodynamic and Turbomachinery Laboratory of UniGE, where a large-scale linear cascade, composed of 7 vanes, is installed in the test section of an open-loop blow-down wind tunnel [166], [167]. More details about the experimental setup are reported in [10]. The experiments are performed at $Re_{2is} = 300k$ under steady conditions (since no wake-generators are included in the present tests).

A turbulence generator grid is located upstream of the inlet plane to generate a Tu equal to 4.2% at 15 mm upstream of the central blade leading edge. By contrast, the measurements at the exit plane are performed at a distance from TE equal to the 33% of the blade C_{ax}.

Figure 5.10: CAD representation of the fences, manufactured fences via rapid prototyping and the linear cascade with fenced blades

As explained in paragraph 2.4, the inlet boundary layer and especially its inner part plays a key role in the generation and development of secondary flows [85]. Therefore, the test-rig is realized so that the thickness and the close-to-the-wall shape of the incoming profile can be varied independently of one another. In particular, the thickness is controlled through the distance between the first rod of the turbulence grid and the endwall that is adjusted by inserting a calibrated step of 100/200 μm. Downstream of the grid the boundary layer develops over the flat endwall up to the wall slot located just upstream of the blade trailing edge: it allows changing the shape of the inner part of the boundary layer by blowing it off.

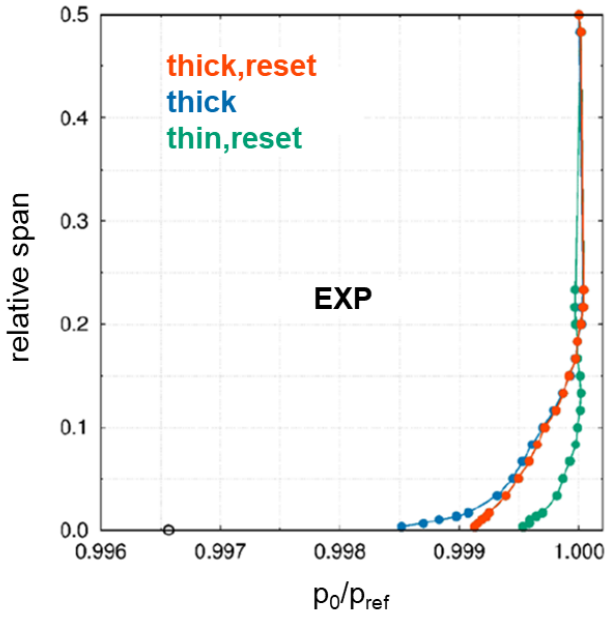

Figure 5.11: Span-wise profile of generated inlet boundary layers [85]

Figure 5.11 shows the span-wise total pressure distributions of the three boundary layers analysed in [85]:

- **thick,reset:** obtained without inserting the step and without closing the slot
- **thick:** the same shape of "thick,reset" in the outer part, close-to-the-endwall part changed by closing the slot
- **thin,reset:** the same shape of "thick,reset" close to the endwall, outer part varied by inserting the calibrated step

The profile "thick" not only induces the strongest system of secondary flows but also turns out to be similar to that observed in the engine environment in which the fences have been originally designed [9]. As a consequence, this is selected to validate the effect of the devices. However, an additional experimental investigation is carried out adopting the "thin,reset" profile as an inlet distribution in order to evaluate the impact of the fences on the aerodynamic performance when secondary flows are very weak.

5.3 Numerical Setup

All the CFD analyses reported in the following are carried out by using the TRAF code. In particular, the adopted turbulence model is the standard Wilcox's k-ω and it is coupled with the transition-sensitive model referred to as γ-$Re_{\theta,t}$ [127].

The computational domain (Figure 5.12) considers one single vane since periodicity is enforced onto the tangential boundaries. The experimental span-wise distributions of total pressure shown above are imposed at the inlet plane. The same operation is performed for the experimental distributions of the blade-to-blade flow angle (α) and the meridian (x-z plane) flow angle (β). Differently, the turbulence boundary conditions are uniformly enforced at the inlet plane: Tu is equal to the experimental value reported above, while the turbulent length scale (TLS) is about 1.5e-03 of the blade C_{ax}. That value is obtained for the present rig by matching the turbulent data at different axial positions of the turbulence grid via CFD simulations. At the exit plane, the static pressure distribution is established by the radial equilibrium starting from the imposed value at the hub.

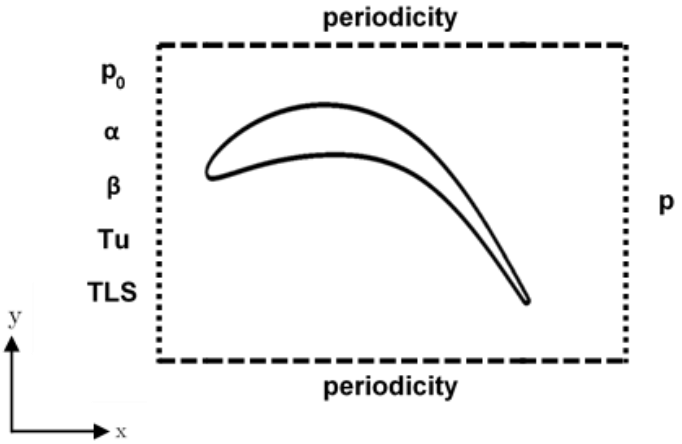

Figure 5.12: Schematic of the computational domain and boundary conditions

The computational grid of each blade passage consists of one elliptic H-type mesh block of about 6M cells: both the B2B mesh and the distribution of span-wise cells are the result of specific grid sensitivity analyses aimed at reaching the grid independence of the numerical solutions. In particular, as the focus of the present activity concerns the prediction of secondary flows, the grids are highly refined in the region of interest (i.e., about the 30% of the span from both the endwalls). Furthermore, the size of the first cells from the wall is selected in order to obtain a y^+ value of about 1 over all of the considered solid surfaces. More details about the criteria adopted to generate a proper mesh are reported in [85].

It is worth noting that the computational grid of the fenced blades is automatically generated by morphing the straight mesh (Figure 5.13): the baseline grid is altered via a perturbation approach which is based on algebraic relations to determine the local displacement of the grid nodes. In other words, the straight mesh is modified by matching the parametric description of the geometry of interest. Moreover, this method takes much less time than that needed by the mesh generation process, and consequently, it is particularly suitable for the optimization phases in which thousands of geometries must be generated.

The morphing process also determines the displacement of nodes within the blade passage at the considered span fraction: it is necessary to control the element skewness that occurs during the relaxation process.

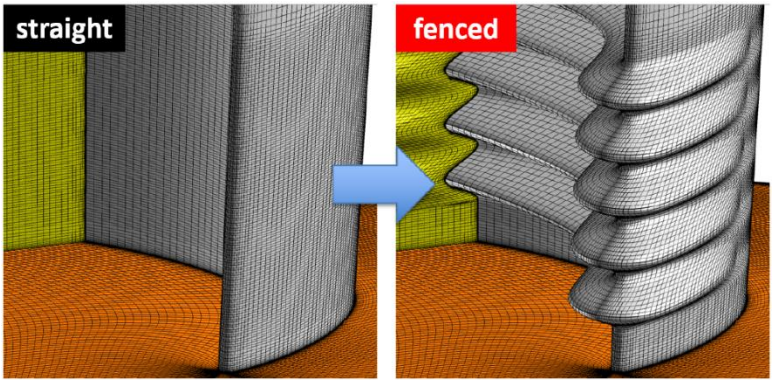

Figure 5.13: Mesh morphing: from straight to fenced [9]

5.3.1 Linear Stage Model

In this frame, the concept of the linear stage in Figure 5.14 is very useful since it allows approximately evaluating the carry-over effect due to the fences that cannot be measured in the cascade test rigs. The numerical solution concerning the stator may be validated via the comparison with the experimental data: both the straight and the fenced configurations are considered. Then, the linear stage model is built by mirroring the straight stator blade via a lean in-house tool. The adopted axial gap between stator and rotor is chosen close to the upper bound of the range of the LPT representative values in order to limit the potential interaction between stator and rotor as much as possible. Consequently, the stator flow-field would just slightly change with respect to the isolated blade setup.

All the boundary conditions imposed at the inlet are the same as those adopted in the experimental tests. By contrast, the rotor translational speed is selected by considering the kinematic similarity between stator and rotor in terms of velocity triangles. It is worth noting that no devices are applied on the rotor blade surface as the analyses focus on the secondary loss and carry-over effect assessment. In such configuration, the rotor loss is not altered by the presence of fences on the rotor itself. As a result, any benefit is entirely due to the carry-over effect.

The CFD calculations are performed under unsteady conditions adopting 100 divisions per blade passage and pursuing the residual convergence of each time-step.

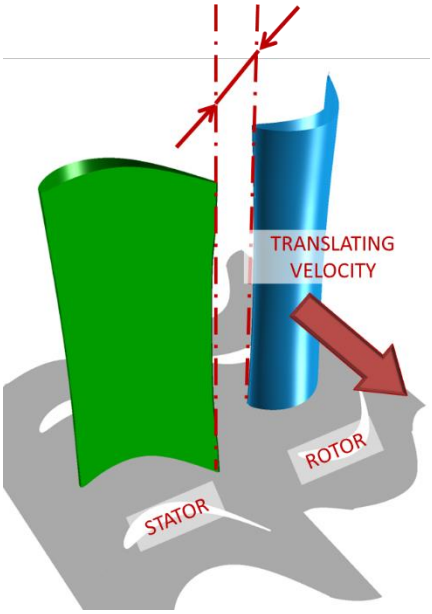

Figure 5.14: Schematic of the linear stage

In conclusion, since the fences have been originally designed in a stage of an engine-like environment, the comparison between the stage efficiency and the linear stage one is useful to verify the representativeness of the cascade design with respect to actual LPTs.

5.4 Numerical and Experimental Validation

The test-rig, described above, is used to measure the impact of fences on the performance and the flow-field. Therefore, both the integral values and the flow details are assessed and collected.

Three configurations are tested:

- straight: blade without devices (as a reference)
- small: blade with the small fences
- optimal: blade with the optimal fences

Figure 5.15 shows the comparison between experimental data and CFD results in terms of span-wise distributions of the exit flow angle and the total pressure loss coefficient. The CFD values are extracted at the same distance from the trailing edge of the measurement plane.

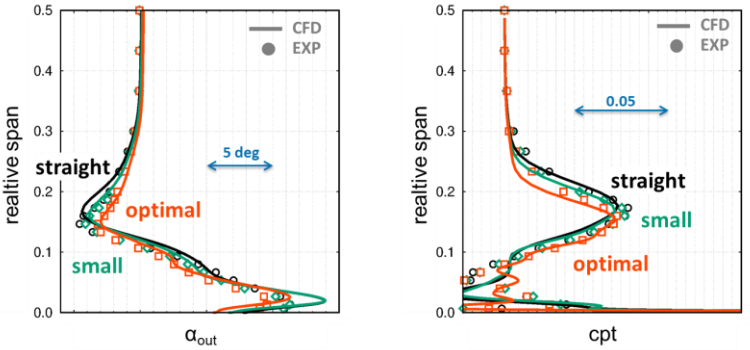

Figure 5.15: CFD vs. EXP: Span-wise distributions of flow angle and total pressure loss coefficient at the outlet plane

First, the agreement between the numerical and experimental data is good both near the midspan and in the secondary flow regions. Thus, the beneficial effects due to the fences are confirmed: the blade loss and the flow-field non-uniformity at the exit plane reduce. In other words, the carry-over effect is brought about by the devices that cause the smoothing of the exit flow angle distribution.

More in details, the effect of the fences on the loss distribution is apparent between the 15% and the 30% of the span. There, the peak reduces and moves towards the endwall. The latter aspect underlines a reduced penetration of the secondary flows. Besides, the importance of the device thickness is readily observable in the graph. Indeed, the optimal fences induce a remarkably larger impact than that of the small fences: it is almost double in loss reduction (Figure 5.16).

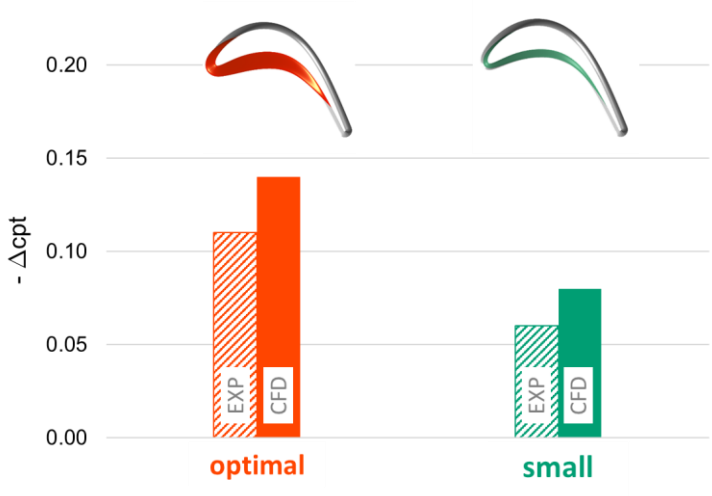

Figure 5.16: Total pressure loss coefficient: straight blade values minus fenced ones

It is worth noting that this beneficial effect is entirely due to the secondary loss reduction since the profile loss, which is approximately equal to the loss value at the midspan, is identical in all the analysed cases. As far as the flow angle is concerned, the under-turning is mitigated by both the type of fences, even if the optimal fences are more effective. In the latter configuration, the flow deviation is approximately halved with respect to the straight blade. In the near-endwall region, the small fences do not induce any noticeable benefit, while the optimal fences determine an over-turning reduction equal to about 2.5 degrees.

In the following, only the results concerning the optimal fences are reported. Therefore, the configuration with the optimal fences is simply referred to as fenced for the sake of brevity.

A more detailed analysis of the flow-field may be performed through the contour plots of Figure 5.17, where the total pressure loss coefficient at the measurement plane is reported. Also, the secondary velocity vectors are superimposed to readily visualize the locations of the main vortices associated with the secondary flows.

First, the impact of fences on the passage vortex is noticeable in both the experimental and numerical data. Moreover, the effects of the devices prove to be similar in the two environments.

Observing the contour plots, even if the peak value looks quite similar for the straight and the fenced configurations, the region associated with high-level loss is narrower in the latter. Indeed, the secondary velocity vectors confirm these effects: the reduction in the intensity of the two counterrotating vortices and the displacement of their cores towards the endwall and the adjacent blade suction side. The increased distance between the vortices determines the reduction in their interaction, and consequently of the related mixing loss. All this translates into the remarkable gain observed at about the 20% of the span in Figure 5.15.

Another effective way to evaluate the secondary flow intensity concerns the use of the secondary kinetic energy coefficient (C_{SKE}), which is commonly adopted in the analyses of the devices aimed at secondary loss reduction [168], [169]. The secondary velocity is the difference between the local velocity and that computed via CFD analyses with inviscid conditions

imposed at the endwalls and without inlet vorticity in order not to generate secondary flows within the blade passage. Then, this difference (c_{sec}) is normalized through the velocity magnitude at the exit plane:

$$C_{SKE} = \frac{c_{sec}^2}{c_{out}^2} \tag{5.3}$$

The contour plots in Figure 5.18 confirm the features described above: the secondary flow structures are less intense when the fences are applied. In addition, the impact of secondary flows on the near-endwall region is clearer in these graphs. The secondary structures that remain close to the endwall prove to be weaker in the fenced configuration inducing a lower over-turning on the downstream row.

In conclusion, the CFD slightly overestimates the beneficial effect of fences on the loss reduction: it is apparent comparing not only the integral values but also the C_{SKE} plots. However, the trends show a good agreement, and the two environments highlight the same flow-features. As a result, the overall agreement proves the reliability of the adopted CFD setup.

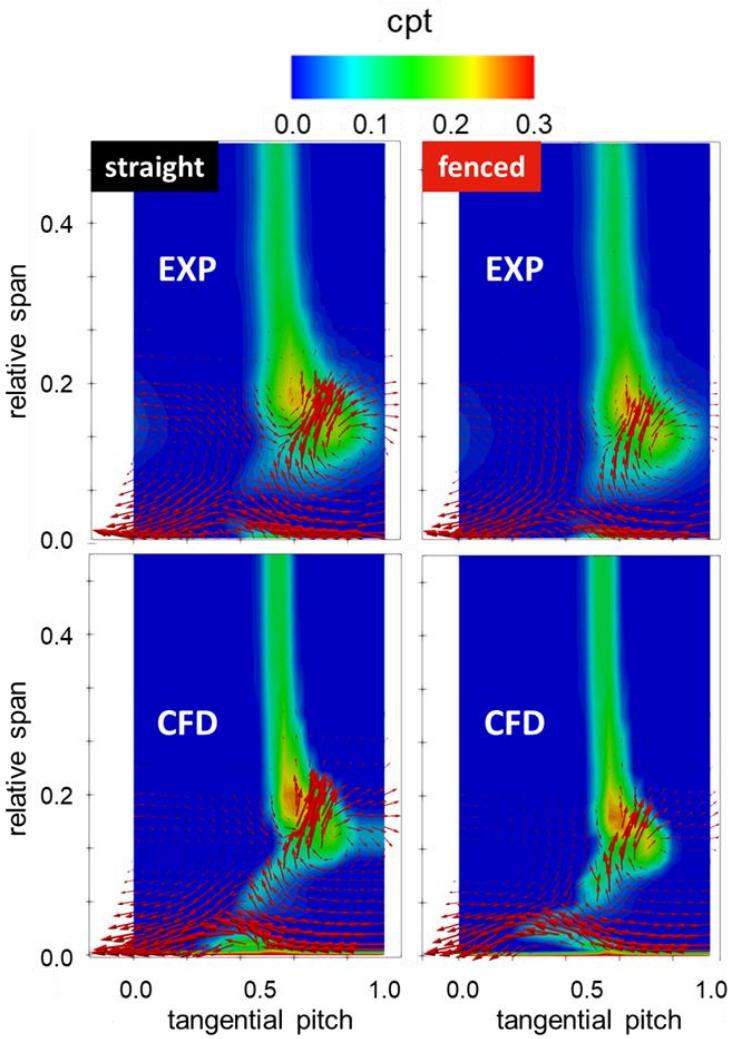

Figure 5.17: Contour plots of total pressure loss coefficient for straight (right) and fenced configurations (left) at the cascade exit plane and secondary velocity vectors: experimental data on the top and numerical data at the bottom

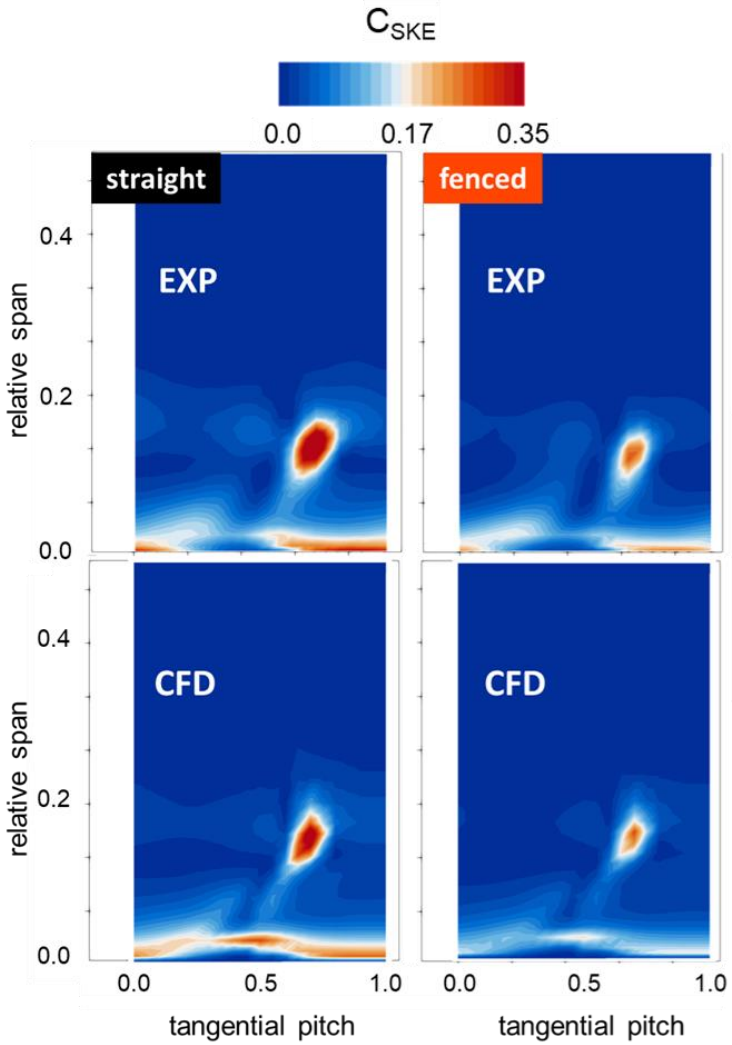

Figure 5.18: Contour plots of CSKE for straight (right) and fenced configurations (left) at the cascade exit plane: experimental data on the top and numerical data at the bottom

5.4.1 Design Robustness

Two additional experimental campaigns, and their numerical counterparts, are performed in order to test the design robustness of the blade fences. In particular, the inlet conditions are changed in terms of inlet boundary layer shape and incidence angle, separately.

First, the impact of the different inlet total pressure distribution is analysed. In this frame, the "thin,reset" profile (paragraph 5.2) is adopted in order to test the fences with milder secondary flows than those previously adopted. In other words, this analysis is aimed at verifying the fence impact in disadvantageous conditions for the devices themselves: both the secondary loss and the flow distortion are reduced. As a consequence, the value of the extra profile loss due to the additional fence wetted surface area must be compared to the lower benefit gained in secondary loss lowering.

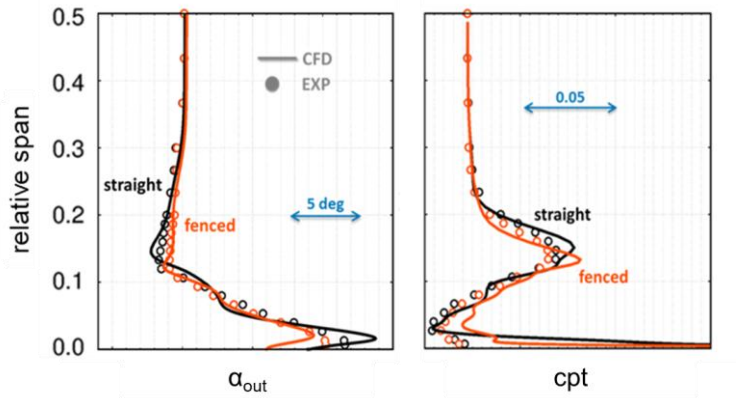

Figure 5.19: CFD vs. EXP: Impact of fences in presence of weak secondary flows. Span-wise distributions of exit flow angle and total pressure loss coefficient

Figure 5.19 shows the span-wise distributions of the flow angle and the total pressure loss coefficient at the cascade exit plane. The agreement between the CFD results and the experimental data is fairly good, even if some minor discrepancies are observable. In particular, the loss coefficient, the under- and over-turning are over-predicted by the CFD in both the configurations: straight and fenced. However, neither the measured impact of fences nor the predicted one turn out to be detrimental for the aerodynamic performance. In other words, the benefit due to the fences reduces as the secondary flow intensity decreases, but the overall loss does not increase.

The second experimental validation concerns the test of the fences in off-design conditions. The adopted incidence variation of ± 6 degrees coincides with the maximum variation available in the test-rig. Experimental and numerical data are compared in Figure 5.20, where the integral values of the total pressure loss coefficient are reported with respect to the nominal condition value of the straight configuration. It is apparent that the fence benefit is not altered at both negative and positive incidence. Therefore, the device effects are preserved not only in a more favorable condition (-6 degrees) but also in a more critical one (+6 degrees). Although some discrepancies are observable between CFD and measurements, the agreement is undoubtedly satisfactory.

Figure 5.21 shows the span-wise distributions of the exit flow angle for the different incidence conditions. The curves for the negative incidence and the nominal conditions are similar since the impact of the inlet angle reduction is lower than that of its increase. Furthermore, the fence effect looks essentially unaltered switching from the nominal conditions to the negative incidence ones.

By contrast, at higher incidence, the effect of the secondary flows, in terms of under- and over-turning, considerably increases. Likewise, the beneficial impact of the fences rises as it is apparent between the 10% and the 25% of the span. In other words, the carry-over effect due to the devices turns out to be larger at the positive incidence than at the negative one.

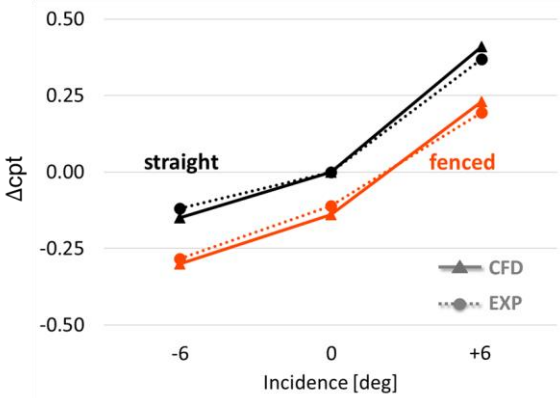

Figure 5.20: CFD vs. EXP: Total pressure loss coefficient variation against incidence angle (values expressed with respect to the nominal conditions for the straight blade)

In conclusion, the design robustness is proved both with weaker secondary flows and at different incidence conditions. The benefit due to the fences reduces as the secondary flow intensity decreases, but the effect never turns negative. Moreover, altering the incidence angle, the loss reduction due to the fences turns out to remain constant. By contrast, the device impact on the flow-field non-uniformity at the exit plane is larger at positive incidence. As a result, the fences should be applied anyhow on the turbine blades regardless of the specific inlet conditions.

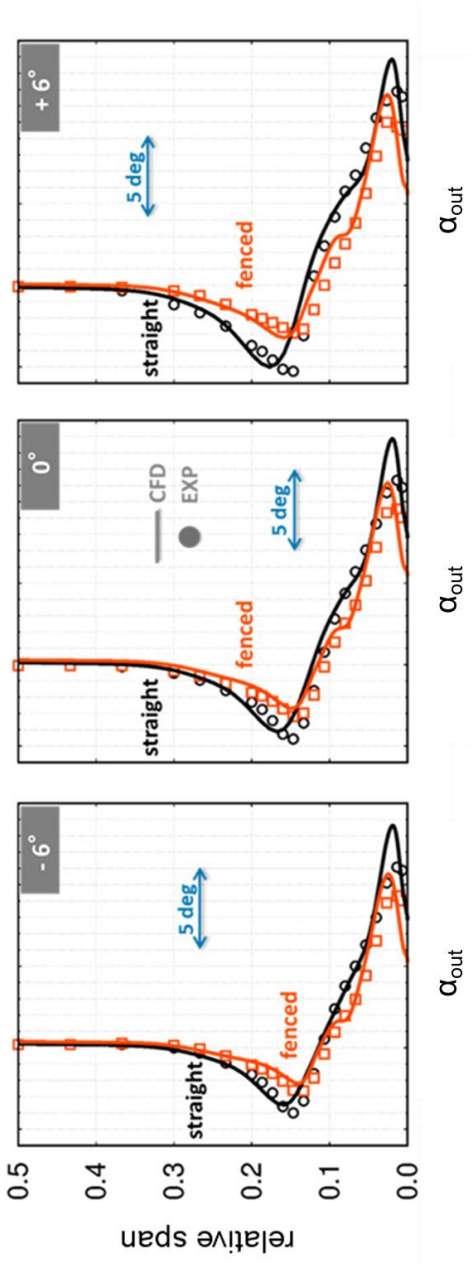

Figure 5.21: CFD vs. EXP: Span-wise distributions of the flow angle at the cascade exit plane for three incidence conditions

5.4.2 Flow-field Analysis

The CFD allows a deeper insight into the basic mechanisms of the secondary flow reduction triggered by the fences: the mitigation of the horseshoe and the passage vortices. Figure 5.22 shows the hub endwall streamlines for the straight and fenced configurations. In addition, the two legs of the horseshoe vortex are highlighted: the suction side one is coloured in blue, while the pressure side one in orange. The presence of the fences near the leading edge alters the radial pressure gradient, which is the driver of the horseshoe vortex: the streamlines in this region highlight the reduction in vorticity from the straight to the fenced configuration. The devices alter even the suction side leg of the horseshoe vortex, which is weaker and flows downstream closer to the blade with respect to the straight configuration. These aspects clearly affect the interaction with the other vortical structures reducing the related loss.

The other main effect is due to the presence of the devices along the pressure side and concerns the direction of the boundary layer particles that turns out to be much more axial in the fenced case. As a result, the low-momentum fluid of the endwall boundary layer reaches the suction side of the adjacent blade later than in the straight configuration. This effect determines a weaker interaction between the two legs of the horseshoe vortices and, consequently, the mitigation of the resulting flow structures (above all the passage vortex). Since the low-momentum fluid migration from the pressure side towards the suction side is above all the mechanism that feeds the passage vortex, it turns out to be weaker in the fenced configuration.

Figure 5.22: Fence impact on the horse-shoe vortex: PS- and SS-legs

The fence impact on the secondary flows may be further analysed in Figure 5.23 that shows the three-dimensional development of the streamlines in the close-to-the-wall region. The streamlines on the pressure side interact with fences so that the coherent structure, which is observable in the straight configuration, looks disrupted and weakened. In addition, this effect prevents the fluid in that region, i.e., at the same span height of the fences, from travelling towards the suction side of the adjacent blade, like in the straight configuration.

Consequently, the pressure side leg of the horseshoe vortex and the passage vortex are mitigated so that the secondary flow penetration in the span-wise direction is lower. Indeed, in the straight configuration, the endwall streamlines tend to climb up towards the midspan in the rear part of the blade. This flow feature is heavily weakened when the fences are applied. It is worth noting that the blade region with the highest entropy generation rate is the rear part of the suction side itself [9]. Indeed, the interaction between the rising vortices and the blade boundary layer causes the loss generation to severely increase.

Besides, the axial vorticity contours show the intensity of the counterrotating vortices at about the 15% of the span. In the straight configuration not only the vortex strength is higher, but also the region occupied by vortical structures is wider.

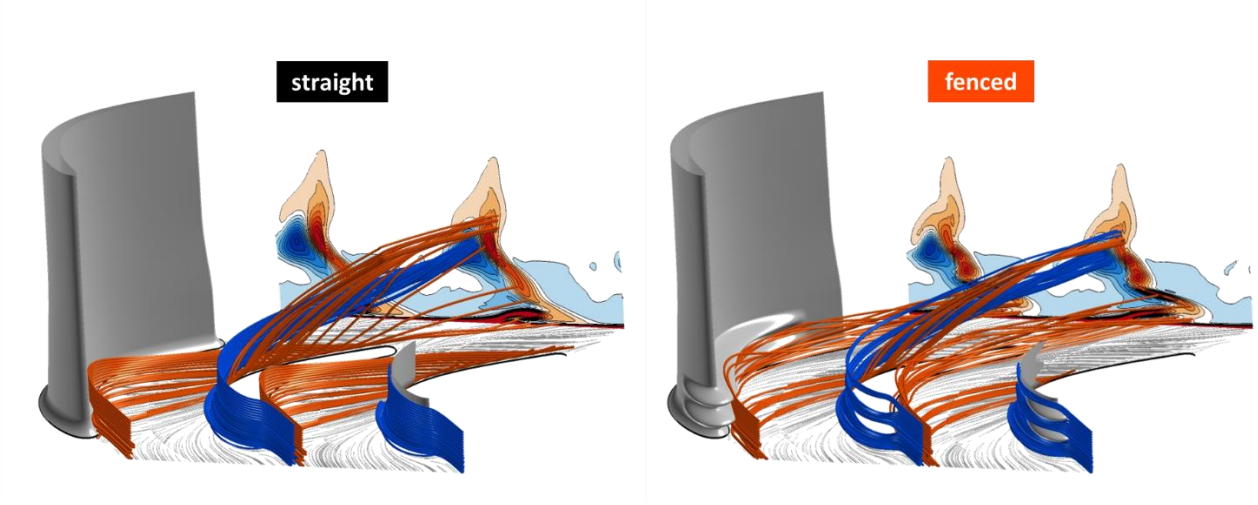

Figure 5.23: Fence impact on secondary flows: Streamlines and axial vorticity contours at cascade exit

5.5 Linear Stage Analysis

The results obtained in the linear stage environment confirm the beneficial effect of the fences both in terms of loss reduction and efficiency gain. In other words, these results not only prove the positive effects of the devices on the stator but also quantify the impact of the carry-over effect on the downstream row. The integral values of the total pressure loss coefficient for stator and rotor and the stage efficiency are reported in Table 3.

Moreover, the benefits observed in this setup are similar to those obtained in the engine-like environment. Indeed, the difference in terms of loss is equal to -0.2% for the stator between fenced and straight configurations. The gain in the efficiency is slightly lower (0.22%) since the engine-like setup has a larger aspect ratio than the cascade so that the weight of the secondary loss with respect to the overall performance is lower. As a consequence, the secondary flow mitigation due to the fences translated into a smaller overall benefit.

	fenced - straight
$\mathbf{cpt_{STA}}$	- 0.19
$\mathbf{cpt_{ROT}}$	- 0.15
$\boldsymbol{\eta_{tt}}$	0.30

Table 3: Percent gain in performance

The span-wise distributions of the flow angle and the total pressure loss coefficient at the stator and rotor exit planes are

reported for the straight and the fenced configurations in Figure 5.24. As far as the stator is concerned, the devices induce two positive effects: the reduction in the loss peak and its displacement towards the endwall. Indeed, in the span region between the 15 and the 30% of the blade height, the straight blade experiences higher loss than the fenced one. In addition, the devices induce a remarkable reduction in the under-turning, which is apparent in the aforementioned span portion. The over-turning in the near-endwall region reduces as well.

In light of this, the flow-field is more uniform at the rotor inlet in the fenced configuration, and consequently, the rotor loss decreases, and the stage efficiency increases.

It is worth remarking that no devices are applied on the rotor blades in both the straight and the fenced configurations. Therefore, for the rotor, the differences in the span-wise distributions of flow angle and loss coefficient with respect to those concerning the straight blade are entirely due to the presence of the devices in the upstream row. However, the effect of the fences is still observable at the rotor exit, where the secondary flows prove to be weakened. Indeed, the analysis of the graphs concerning the rotor highlights a noticeable loss reduction due to the stator fences in the span portion between the 24% and the 32% of the blade height. With respect to the device impact on the flow angle distribution along the span, even though the over-tuning in the near-endwall region looks larger, beyond the 5% of the blade height the flow looks much more uniform in the fenced configuration.

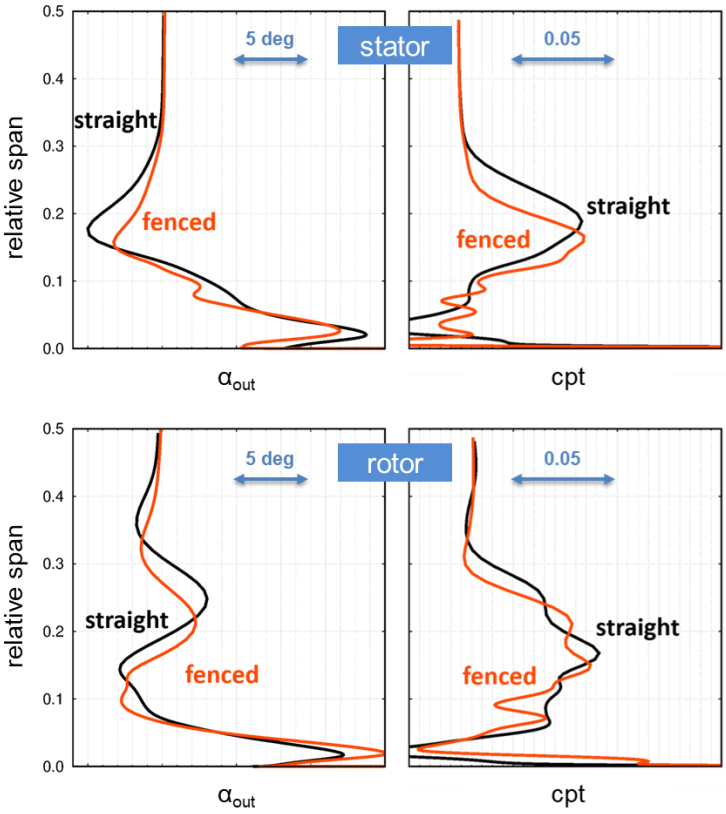

Figure 5.24: Span-wise distributions of flow angle and total pressure loss coefficient at stator (top) and rotor (bottom) outlet

6 Conclusions

Two effective design solutions for reducing aerodynamic losses in aeronautical Low-Pressure Turbines (LPTs) are explained in the present thesis: a lean model for optimizing airfoils in a multi-row environment and the development of a passive control device, referred to as blade fence, for reducing secondary losses. Both concepts are developed through the combined use of Artificial Neural Networks (ANNs) and CFD (Computational Fluid Dynamics).

The airfoil optimization model is generated by starting from a single blade profile, which is one of the standard configurations of low TRL (Technology Readiness Level) design phases. It is apparent that the isolated blade cannot be representative of actual engines; however, such setup is the simplest and cheapest one for experimental tests. On the other hand, the reliability and affordability of numerical simulations are higher and higher so that their utilization to investigate complex configurations in the early design phases should be considered.

Therefore, a 1.5 stage is built by mirroring the single blade profile, and such setup is used to optimize the stator airfoil in place of the standard single blade setup. The multi-row environment is simulated via both RANS and URANS simulations. The RANS approach is the reference one as it is the most widespread in the industrial world. By contrast, the URANS approach is adopted to prove the importance of considering the unsteady interactions even in the first design process stages.

A fair comparison between the results of the steady and unsteady optimization approaches must consider four different aspects: the performance benefit under design and off-design operating conditions, the advantage concerning the reduction in blade count and the computational cost related to the methods.

The benefits in terms of loss reduction at the design point are remarkable for both the optimal airfoils: OPT-S (steady approach) and OPT-U (unsteady approach). Indeed, the total pressure loss coefficient (cpt) decreases by about 0.16% for OPT-S and 0.32% for OPT-U, if compared to the baseline case. However, OPT-S shows a far higher sensitivity to the reduced frequency ($\bar{f}$) and Reynolds number than OPT-U. In other words, the performance of OPT-S significantly varies by changing the operating point, while OPT-U shows higher robustness in off-design conditions.

The additional advantage provided by the unsteady approach concerns the 15% increase in blade pitch to chord ratio (g/C) for OPT-U if compared to the baseline case. Indeed, this aspect is crucial in turbomachines since the reduction in blade count leads to relevant benefits in terms of reliability and costs. On the other hand, the steady approach dictates a 1% reduction in g/C with respect to the baseline case.

Finally, the computational cost must be considered since it is the main limitation of unsteady CFD approaches, especially in activities like optimizations that require thousands of calculations. In the present work, 5000 geometries are analyzed to generate the ANN training datasets. On average, one URANS simulation takes 1.92 hours to achieve convergence with the adopted setup on one Intel® Core™ i5-6500 CPU @ 3.20 GHz, and the steady-to-unsteady computational time ratio is about 1/4. Such increase turns out to be easily manageable considering

the increasing HPC cluster size. Moreover, 95.2% of the URANS analyses achieve convergence against 66.8% of the steady ones. This aspect may be thought of as a reduction in the overall number of performed simulations that is necessary to reach the goal. However, such information deals with a qualitative issue rather than a quantitative one. Indeed, the convergence ratio proves not to be uniformly distributed over the considered design space. In other words, the steady approach turns out to be inadequate to investigate some design space regions, which, in turn, deem to be relevant to gain a more accurate ANN model and, above all, a more performant airfoil (i.e., OPT-U).

The last part of the thesis describes the design and validation of the blade fences. Their development has been performed in collaboration with Avio Aero and Università degli Studi di Genova (UniGE).

More in details, the fence is a shelf-like protrusion of the blade surface located near the endwalls. The device geometry is optimized in both the B2B plane and span-wise direction via the combined use of CFD and ANNs. In particular, the number of fences, their position along the blade surfaces and their width turn out to be the most relevant parameters.

The presence of the device around the leading edge alters the local radial pressure gradient, which is the physical driver of the horseshoe vortex. Also, the fence development along the blade pressure side causes the flow migration towards the adjacent blade suction side to reduce so that the passage vortex turns out to be undermined. Consequently, the fence determines the hindering of secondary flows so that the related losses lower. Moreover, the device causes the so-called carry-over effect to occur. Indeed, the flow-field non-uniformity at the row exit

plane reduces, and thus the downstream blades experience flow angles more similar to the design ones.

Besides, the blade fences are validated through both numerical and experimental analyses. The latter ones are performed by UniGE in a low-speed linear cascade. The devices undergo a redesign process to respect the additional constraints related to the manufacturing and the operating conditions of the test-rig. Moreover, fences characterized by two different widths are produced and tested.

Both the experimental and CFD analyses indicate the benefits due to the devices in terms of loss decrease and straightening of the exit flow angle span-wise distribution. In particular, the cpt reduction is equal to 0.11% and 0.14% for experiments and CFD, respectively. Advantages are noticeable even at off-design conditions as three different incidence angles are analyzed. Likewise, the impact of the incoming boundary layer thickness is assessed since it is one of the main drivers of the endwall flows.

In brief, one could state that the fence effect lowers as the secondary flow intensity decreases, but it never turns negative in any of the experimental and CFD analyzed setups.

Finally, as the cascade tests allow evaluating only the fence impact on one single row, a linear stage model is numerically generated to assess the carry-over effect. The benefits are not only confirmed in terms of stage efficiency gain but also are comparable to those evaluated in the original design environment (i.e., an embedded LPT stage).

Future Developments

As far as the airfoil optimization model is concerned, a feasible future development might consider 3D blades instead of 2D airfoils. However, Full Navier-Stokes analyses would require a massive increase in computational cost since both the DoFs and the geometry discretization along the span-wise direction would rise. Therefore, Thin-Layer 3D analyses could represent a fair trade-off between computational cost increase and model accuracy improvement. As an approximation, 16 cells could be adopted in the radial direction so that one URANS analysis would take around 30.72 hours on one CPU core. Besides, the number of DoFs should be increased and possibly doubled. As a consequence, the higher complexity of the resulting design space might require a larger database to generate an accurate ANN model.

Another future development may concern the adoption of a hybrid RANS-URANS approach. For example, the Non-Linear Harmonic method would allow simulating one block per row, even if the considered rows had different circumferential gaps. In this way, a wide range of $\bar{f}$ could be analyzed without altering the computational cost. However, the design space would become more complex as the DoF concerning the rotor pitch should be added.

Finally, feasible developments for the blade fences might concern the analysis of their interaction with casing and tip endwall flows in an annular geometry since differences in vortical structures are detected if compared to linear cascades with straight blades. Moreover, the secondary air flows significantly alter the endwall boundary layer conditions, and thus their effects should be included in the secondary flow analyses. Such an environment would be more representative of

real LPTs so that the fence impact assessment would be more reliable.

References

[1] Eurostat, «Air Transport Statistics,» 12 2019. [Online]. Available: https://ec.europa.eu/eurostat/statistics-explained/index.php/Air_transport_statistics. [Consultato il giorno 22 10 2020].

[2] European Commission, «EU Aviation: 25 years of reaching new heights,» 22 10 2020. [Online]. Available: https://ec.europa.eu/transport/modes/air/25years-eu-aviation_en. [Consultato il giorno 22 10 2020].

[3] Eurocontrol, «COVID-19 impact on the European air traffic network,» 09 2020. [Online]. Available: https://www.eurocontrol.int/covid19. [Consultato il giorno 22 10 2020].

[4] Directorate General for Research and Innovation, «European Aeronautics: A Vision for 2020,» European Commission, 2001.

[5] Directorate General for Research and Innovation; Directorate General for Mobility and Transport, «Flightpath 2050: Europe's Vision for Aviation,» European Commission, 2011.

[6] Advisory Council for Aviation Research and Innovation in Europe (ACARE), «A New Beginning for European Aviation Research,» 2016. [Online]. Available: https://www.acare4europe.org/about-acare. [Consultato il giorno 22 10 2020].

[7] J. Weatheritt and R. Sandberg, "A novel evolutionary algorithm applied to algebraic modifications of the RANS stress-strain relationship," *Weatheritt, J., & Sandberg, R. (2016). A novel evolutionary algorithm applied to algebraic modifications of Journal of Computational Physics,* vol. 325, pp. 22-37, 2016.

[8] H. D. Akolekar, J. Weatheritt, N. Hutchins, R. D. Sandberg, G. Laskowski and V. Michelassi, "Development and Use of Machine-Learnt Algebraic Reynolds Stress Models for Enhanced Prediction of Wake Mixing in Low Pressure Turbines," in *Proceedings of ASME Turbo Expo 2018*, Oslo, Norway, 2018.

[9] F. Rubechini, M. Giovannini, A. Arnone, D. Simoni e F. Bertini, «Reducing Secondary Flow Losses in Low-Pressure Turbines with Blade Fences. Part I: Design in an Engine-like Environment,» in *Proceedings of ASME Turbo Expo 2019: Turbomachinery Technical Conference and Exposition*, Phoenix, 2019.

[10] M. Giovannini, F. Rubechini, G. Amato, A. Arnone, D. Simoni, V. Yepmo, F. Satta e F. Bertini, «Reducing Secondary Flow Losses in Low-Pressure Turbines with Blade Fences. Part II: Experimental Validation on Linear Cascades,» in *Proceedings of ASME Turbo Expo 2019: Turbomachinery Technical Conference and Exposition*, Phoenix, 2019.

[11] D. C. Wisler, «The Technical and Economic Relevance of Understanding Blade Row Interactions Effects in Turbomachinery,» 1998.

[12] J. Kurze, «Fundamental Differences Between Conventional and Geared Turbofans,» in *Proceedings of ASME Turbo Expo*, Orlando, FL, USA, 2009.

[13] D. E. Halstead, D. Wisler, T. H. Okiishi, G. J. Walker, H. P. Hodson e H. W. Shin, «Boundary Layer Development in Axial Compressors and Turbines: Part 1 of 4—Composite Picture1,» *Journal of Turbomachinery,* vol. 119, 1997.

[14] L. Qi e Z. Zou, Unsteady Flows in Turbines, Noise Control, Reduction and Cancellation Solutions in Engineering, Daniela Siano - InTech, 2012.

[15] J. D. Denton, «Loss Mechanisms in Turbomachines,» *Journal of Turbomachinery,* 1993.

[16] V. S. P. Chaluvadi, A. I. Kalfas e H. P. Hodson, «Blade Row Interaction in a High-Pressure Steam Turbine,» *Journal of Turbomachinery,* vol. 125, 2003.

[17] D. Lengani, D. Simoni, R. Pichler, R. D. Sandberg, V. Michelassi e F. Bertini, «On the Identification and Decomposition of the Unsteady Losses in a Turbine Cascade,» *Journal of Turbomachinery,* vol. 141, 2019.

[18] O. P. Sharma e T. L. Butler, «Predictions of Endwall Losses ans Secondary Flows in Axial Flow Turbine Cascades,» *Journal of Turbomachinery,* vol. 109, 1987.

[19] S. L. Dixon e C. A. Hall, Fluid Mechanics and Thermodynamics of Turbomachinery, seventh a cura di, Elsevier Inc., 2014.

[20] V. Michelassi, L. Chen, R. Pichler, R. Sandberg e R. Bhaskaran, «High-Fidelity Simulations of Low-Pressure Turbines: Effect of Flow Coefficient and Reduced Frequency on Losses,» *Journal of Turbomachinery,* vol. 138, 2016.

[21] D. Lengani, D. Simoni, M. Ubaldi, P. Zunino, F. Bertini e V. Michelassi, «Accurate Estimation of Profile Losses and Analysis of Loss Generation Mechanisms in a Turbine Cascade,» *Journal of Turbomachinery,* vol. 139, 2017.

[22] J. E. LaGraff, D. E. Aships, M. L. G. Oldfield e J. P. Gostelow, «Unsteady Flows in Turbomachinery,» NASA, 2006.

[23] M. B. Giles, «UNSFLO: a Numerical Method for the Calculation of Unsteady Flow in Turbomachinery,» MIT Department of Aeronautics and Astronautics, 1991.

[24] H. P. Hodson e R. J. Howell, «Bladerow Interactions, Transition, and High-Lift Aerofoils in Low-Pressure Turbines,» *Annual Reviews of Fluid Mechanics,* vol. 37, 2005.

[25] H. P. Hodson e R. J. Howell, «The Role of Transition in High-Lift Low-Pressure Turbines for Aeroengines,» *Progress in Aerospace Sciences,* n. 41, 2005.

[26] S. D. Hunter e S. R. Manwaring, «Endwall Cavity Flow Effects on Gaspath Aerodynamics in an Axial Flow Turbine: Part I - Experimental and Numerical Investigation,» 2000.

[27] A. M. Wallis, J. D. Denton e A. A. J. Demargne, «The Control of Shroud Leakage Flows to Reduce Aerodynamics Losses in a Low Aspect Ratio, Shrouded Axial Flow Turbine,» 2000.

[28] J. E. Anker e J. F. Mayer, «Simulation of the Interaction of Labyrinth Seal Leakage Flow and Main Flow in an Axial Turbine,» 2002.

[29] P. Peters, V. Breisig, A. Giboni, C. Lerner e H. Pfost, «The Influence of the Clearance of Shrouded Rotor Blades on the Development of the Flowfield and Losses in the Subsequent Rotor,» 2000.

[30] G. Pullan, «Secondary Flows and Loss Caused by Row Interaction in a Turbine Stage,» 2004.

[31] A. Arnone, M. Marconcini, A. S. D. Greco e E. Spano, «Numerical Investigation of Three-Dimensional Clocking Effects in a Low Pressure Turbine,» 2003.

[32] A. Arnone, M. Marconcini e R. Pacciani, «On the Use of Unsteady Methods in Predicting Stage Aerodynamic Performance,» Lyon, 2000.

[33] E. M. Greitzer, A. H. Epstein, M. B. Giles, J. E. McCune e C. S. Tan, «Unsteady Flow Phenomena in Turbomachines,» MIT Department of Aeronautics and Astronautics, 1992.

[34] H. P. Hodson, T. P. Hynes, E. M. Greitzer e C. S. Tan, «A Physical Interpretation of Stagnation Pressure and

Enthalpy Changes in Unsteady Flows,» *Journal of Turbomachinery,* vol. 134, 2012.

[35] H. P. Hodson e W. N. Dawes, «On the Interpretation of Measured Profile Losses in Unsteady Wake-Turbine Blade Interaction Studies,» vol. 120, 1998.

[36] E. M. Greitzer, C. S. Tan e M. Graf, «Internal Flow: Concepts and Applications,» 2004.

[37] T. Korakianitis, «On the propagation of viscous wakes and potential flow in axial-turbine cascades,» *Journal of Turbomachinery,* vol. 115, 1993.

[38] H. P. Hodson, «Blade row interactions in low pressure turbines,» 1998.

[39] P. G. Hill e A. H. Stenning, «Laminar Boundary Layers in Oscillatory Flow,» *Journal of Basic Engineering,* vol. 82, 1960.

[40] M. H. Patel, «On the Turbulent Boundary Layers in Oscillatory Flow,» 1977.

[41] M. J. Lighthill, «The Response of Laminar Skin Friction and Heat Transfer to Fluctuations in the Stream Velocity,» 1954.

[42] H. W. Emmons, «The Laminar-Turbulen Transition in a Boundary Layer – Part I,» *Journal of Aerospace Science and Technology,* n. 18, 1951.

[43] R. E. Mayle, «The Role of Laminar-Turbulent Transition in Gas Turbine Engines,» Orlando, 1991.

[44] H. Schlichting, Boundary Layer Theory, New York: McGraw-Hill, 1979.

[45] B. J. Abu-Ghannam e R. Shaw, «Natural Transition of Boundary Layers - The Effects of Turbulence, Pressure Gradient and Flow History,» *Journal of Mechanical Engineering Science,* n. 22, 1980.

[46] M. V. Morkovin, On the Many Faces of Transition, Viscous Drag Reduction, New York: Plenum Press, 1969.

[47] A. Hatman e T. Wang, «Separated-Flow Transition part I - Experimental Methodology and Mode Classification,» Stockholm, 1998.

[48] A. Hatman e T. Wang, «Separated-Flow Transition part II - Experimental Results,» Stockholm, 1998.

[49] A. Hatman e T. Wang, «Separated-Flow Transition Part III - Primary Modes and Vortex Dynamics,» Stockholm, 1998.

[50] A. Hatman e T. Wang, «A Pediction Model for Separated Flow Transition,» Stockholm, 1998.

[51] B. R. McAuliffe e M. I. Yaras, «Transition Mechanisms in Separation Bubbles under Low and High Freestream Turbulence,» *Journal of Turbomachinery,* vol. 132, 2010.

[52] A. Mahallati, B. R. McAuliffe, S. A. Sjolander e T. J. Praisner, «Aerodynamics of a Low-Pressure Turbine Airfoil at Low Reynolds Numbers - Part I: Steady Flow

Measurements,» *Journal of Turbomachinery,* vol. 135, 2013.

[53] M. Gaster e R. E. Mayer, «On Transition to Turbulence in Boundary Layers,» in *Proceedings of a Symposium*, 1980.

[54] J. H. Watmuff, «Evolution of a Wave Packet into Vortex Loops in a Laminar Separation Bubble,» *Journal of Fluid Mechanics,* n. 397, 1999.

[55] S. S. Diwan e O. N. Ramesh, «On the inflectional instability of a laminar separation bubble,» *Journal of Fluid Mechanics,* vol. 629, 2009.

[56] J. D. Coull e H. P. Hodson, «Unsteady Boundary-Layer Transition in Low-Pressure Turbines,» *Journal of Fluid Mechanics,* vol. 681, 2011.

[57] R. G. Jacobs e P. A. Durbin, «Shear Sheltering and the Continuous Spectrum of the Orr-Sommerfeld equation,» *Physics of Fluids,* vol. 10, 1998.

[58] R. G. Jacobs e P. A. Durbin, «Simulations of Bypass Transition,» *Journal of Fluid Mechanics,* vol. 428, 2001.

[59] P. H. Alfredsson e M. Matsubara, «Streaky Structures in Transition,» *In Transitional Boundary Layers in Aeronautics,* 1996.

[60] G. B. Schubauer e P. S. Klebanoff, «Contributions on the Mechanics of Boundary Layer Transition,» NACA, 1956.

[61] W. J. Solomon, G. J. Walker e J. P. Gostelow, «Transition Length Prediction for Flows with Rapidly Changing Pressure Gradients,» *Journal of Turbomachinery,* n. 118, 1996.

[62] A. D'Ovidio, J. A. Harkins e J. P. Gostelow, «Turbulent Spots in Strong Adverse Pressure Gradient, part 2 - Spot Propagation and Spreading Rates,» in *Proceedings of the ASME TurboExpo*, New Orleans, 2001.

[63] A. Mahallati e S. A. Sjolander, «Aerodynamics of a Low-Pressure Turbine Airfoil at Low Reynolds Numbers - Part II: Blade-Wake Interaction,» *Journal of Turbomachinery,* vol. 135, 2013.

[64] X. Wu, R. G. Jacobs, J. C. R. Hunt e P. A. Durbin, «Simulation of Boundary Layer Transition Induced By periodically Passing Wakes,» *Journal of Fluid Mechanics,* vol. 398, 1999.

[65] N. A. Cumpsty, Compressor Aerodynamics, Krieger Publishing Company, 2004.

[66] H. I. H. Saravanamuttoo, G. F. C. Rogers, H. Cohen, P. V. Straznicky e A. C. Nix, Gas Turbine Theory, Pearson, 2017.

[67] W. R. Hawthorne, «Rotational Flow through Cascades,» *Journal of Mechanics and Applied Mathematics,* vol. 3, 1955.

[68] C. H. Sieverding, «Recent Progress in the Understanding of Basic Aspects of Secondary Flows in Turbine Blade Passages,» 1985.

[69] L. S. Langston, «Secondary Flows in Axial Turbines,» 2001.

[70] A. Klein, «Investigation of the Entry Boundary Layer on the Secondary Flows in the Blading of Axial Turbines,» 1966.

[71] L. S. Langston, M. L. Nice e R. M. Hooper, «Three-Dimensional Flow within a Turbine Blade Passage,» *Journal of Engineering for Power,* vol. 99, 1977.

[72] H. P. Wang, S. J. Olson, R. J. Goldstein e E. R. G. Eckert, «Flow Visualization in a Linear Turbine Cascade of High Performance Turbine Blades,» *Journal of Turbomachinery,* vol. 119, 1997.

[73] J. Cui, V. N. Rao e P. G. Tucker, «Numerical Investigation of Secondary Flows in a High-Lift Low Pressure Turbine,» *International Journal of Heat and Fluid Flow,* vol. 63, 2016.

[74] R. Pichler, Y. Zhao, R. D. Sandberg, V. Michelassi, R. Pacciani, M. Marconcini e A. Arnone, «LES and RANS Analysis of the End-wall Flow in a Linear LPT Cascade, Part I: Flow and Secondary Vorticity Fields under Varying Inlet Condition,» in *Proceedings of ASME Turbo Expo 2018*, Oslo, 2018.

[75] C. Sieverding e P. V. d. Bosch, «The Use of Coloured Smoke to Visualize Secondary Flows in a Turbine-Blade Cascade,» *Journal of Fluid Mechanics,* vol. 134, 1983.

[76] R. Goldstein e R. Spores, «Turbulent Transport on the Endwall in the Region between Adjacent Turbine Blades,» *Journal of Heat Transfer,* vol. 110, 1988.

[77] P. Lampart, «Investigation of Endwall Flows ans Losses in Axial Turbines - Part I: Formation of Endwall Flows and Losses,» *Journal of Theoretical and Applied Mechanics,* vol. 47, 2009.

[78] S. Kang e C. Hirsch, «Three Dimensional Flow in a Linear Compressor Cascade at Design Conditions,» in *Proceedings of International Gas Turbine and Aeroengine Congress and Exposition*, Orlando, 1991.

[79] H. P. Hodson e R. G. Dominy, «Three-Dimensional Flow in a Low-Pressure Turbine Cascade at its Design Condition,» *Journal of Turbomachinery,* vol. 109, 1987.

[80] M. Y. Jabbari, R. J. Goldstein, K. C. Marston e E. R. G. Eckert, «Three Dimensional Flow within Large Scale Turbine Cascades,» *Warme- und Stoffubertragung,* vol. 27, 1992.

[81] B. Winhart, M. Sinkwitz, A. Schramm, D. Engelmann, F. D. Mare e R. Mailach, «Experimental and Numerical Investigation of Secondary Flow Structures in an Annular Low Pressure Turbine Cascade under Periodic Wake Impact - Part 2: Numerical Results,» *Journal of Turbomachinery,* vol. 141, 2019.

[82] G. Pullan, J. Denton e M. Dunkley, «An Experimental and Computational Study of the Formation of a Streamwise Shed Vortex in a Turbine Stage,» *Journal of Turbomachinery,* vol. 125, 2003.

[83] M. Sinkwitz, D. Engelmann e R. Mailach, «Experimental Investigation of Periodically Unsteady Wake Impact on the Secondary Flow in a 1.5 Stage Full Annular LPT Cascade with Modified T106 Blading,» Charlotte, 2017.

[84] M. Marconcini, R. Pacciani, A. Arnone, V. Michelassi, R. Pichler, Y. Zhao e R. Sandberg, «LES and RANS Analysis of the End-wall Flow in a Linear LPT Cascade, Part I: Loss Generation,» in *Proceedings of ASME Turbo Expo 2018*, Oslo, 2018.

[85] M. Giovannini, F. Rubechini, M. Marconcini, D. Simoni, V. Yepmo e F. Bertini, «Secondary Flows in Low-Pressure Turbines Cascades: Numerical and Experimental Investigation of the Impact of the Inner Part of the Boundary Layer,» *Journal of Turbomachinery,* vol. 140, 2018.

[86] J. Cui e P. Tucker, «Numerical Study of Purge and Secondary Flows in a Low-Pressure Turbine,» *Journal of Turbomachinery,* vol. 139, 2017.

[87] G. Maclsaac, S. Sjolander e T. Praisner, «Measurement of Losses and Reynolds Stresses in the Secondary Flow Downstream of a Low-Speed Linear Turbins Cascade,» *Journal of Turbomachinery,* vol. 134, 2012.

[88] P. Bear, M. Wolff, A. Gross, C. R. Marks e R. Sondergaard, «Experimental Invesitgation of Total

Pressure Loss Development in a Highly Loaded Low-Pressure Turbine Cascade,» *Journal of Turbomachinery,* vol. 140, 2018.

[89] J. Denton e G. Pullan, «A Numerial Investigation into the Sources of Endwall Loss in Axial Flow Trbines,» 2012.

[90] C. Casciaro, M. Treiber e M. Shell, «Unsteady Transport Mechanisms in an Axial Turbine,» *Journal of Turbomachinery,* vol. 122, 2000.

[91] J. Zabski e Z. Wiercinski, «Influence of the Negative and Positive Jet Wake on Laminar-Turbulent Transition in a Boundary Layer,» *Journal of Theoretical and Applied Mechanics,* vol. 47, 2009.

[92] R. D. Stieger e H. P. Hodson, «The Unsteady Development of a Turbulent Wake Through a Downstream Low-Pressure Turbine Blade Passage,» 2005.

[93] J. L. Kerrebrock e A. A. Mikolajczak, «Intra-stator Transport of Rotor Wakes and its Effect on Compressor performance,» *Journal of Engineering for Power,* vol. 92, 1970.

[94] E. M. Curtis, H. P. Hodson, M. R. Banieghbal, J. D. Denton, R. J. Howell e N. W. Harvey, «Development of Blade Profiles for Low-Pressure Turbine Applications,» *Journal of Turbomachiney,* vol. 119, 1997.

[95] E. M. Greitzer, «An Introduction to the Unsteady Flow in Turbomachines,» AGARD, 1984.

[96] R. X. Meyer, «The Effects of Wakes on the Transient Pressure and Velocity Distributions in Turbomachines,» *Journal of Basic Engineering,* vol. 80, 1958.

[97] M. Sinkwitz, B. Winhart, D. Engelmann, F. D. Mare e R. Mailach, «Experimental and Numerical Investigation of Secondary Flow Structures in a n Annular Low Pressure Turbine Cascade Under Periodic Wake Impact - Part 1: Experimental Results,» *Journal of Turbomachinery,* vol. 141, 2019.

[98] M. Berrino, D. Lengani, D. Simoni, M. Ubaldi e P. Zunino, «Dynamics and Turbulence Characteristics of Wake-Boundary Layer Interaction in a Low Pressure Turbine Blade,» in *Proceedings of TurboExpo*, Montreal, 2015.

[99] X. Wu e P. A. Durbin, «Evidence of Longitudinal Vortices Evolved from Distorted Wakes in a Turbine Passage,» *Journal of Fluid Mechanics,* vol. 446, 2001.

[100] K. Lee e J. T. C. Liu, «On the growth of mushroomlike structure in nonlinear spatially developng Gortler vortex flow,» *Physics of Fluids,* vol. 4, 1991.

[101] R. D. Stieger e H. P. Hodson, «The Transition Mechanism of Highly Loaded Low-Pressure Turbine Blades,» in *ASME turbo expo*, Atlanta, 2003.

[102] A. Binder, T. Schroeder e J. Hourmuziadis, «Turbulence measurements in a multistage low pressure turbine,» *Journal of Turbomachinery,* vol. 111, 1989.

[103] N. Arndt, «Blade Row Interaction in a Multistage Low Pressure Turbine,» 1991.

[104] X. Schroeder, «Investigations of Blade Row Interaction and Boundary Layer Transition Phenomena in a Multistage Aero Engine Low Pressure Turbine by Measurements with Hot-film Probes and Surface-mounted Hot-film gauges,» 1991.

[105] D. E. Halstead, «Flowfield Unsteadiness and Turbulence in Multistage Low Pressure Turbine,» 1997.

[106] H. Pfeil, R. Herbst e T. Schroder, «Investigation of the Laminar-Turbulent Transition Boundary Layers Disturbed by Wakes,» *Journal of Engineering for Power,* n. 105, 1983.

[107] V. Schulte e H. P. Hodson, «Wake-Separation Bubble Interaction in Low Pressure Turbines,» in *30th Joint Propulsion Conference and Exhibit*, Indianapolis, 1994.

[108] V. Schulte e H. P. Hodson, «Unsteady Wake-Induced Boundary Layer Transition in High Lift LP Turbines,» *Journal of Turbomachinery,* n. 120, 1998.

[109] J. S. Addison e H. P. Hodson, «Modelling of Unsteady Transitional Boundary Layers,» *Journal of Turbomachinery,* n. 114, 1992.

[110] S. Zhong, C. Kittichaikarn, H. P. Hodson e P. Ireland, «A Study of Unsteady Wake-Induced Boundary Layer Transitionl with Thermochromic Liquid Crystals,» in *Proceedings of the IMECH conference*, London, 1998.

[111] A. B. Johnson, M. L. G. Oldfield, M. J. Rigby e M. B. Giles, «Nozzle Guide Vane Shock Wave Propagation and Bifurcation in a Transonic Turbine Rotor,» 1990.

[112] R. Stieger, D. Hollis e H. Hodson, «Unsteady Surface Pressures due to Wake Induced Transition in a Laminar Separation Bubble on a LP Turbine Cascade,» in *Proceedings of ASME Turbo Expo*, Atlanta, 2003.

[113] R. D. Stieger e H. P. Hodson, «Unsteady Dissipation Measurements on a Flat Plate Subject to Wake Passing,» Prague, 2003.

[114] R. D. Stieger, *The Effects of Wakes on Separating Boundary Layers in Low Pressure Turbines,* Cambridge: University of Cambridge, 2002.

[115] V. Michelassi, L. W. Chen, R. Pichler e R. D. Sandberg, «Compressible Direct Numerical Simulation of Low-Pressure Turbines - Part II: Effect of Inflow Disturbances,» *Journal of Turbomachinery,* vol. 137, 2015.

[116] M. T. Schobeiri e B. Ozturk, «Experimental Study of the Effect of the Periodic Unsteady Wake Flow on Boundary Layer Development, Separation, and Re-attachment Along the Surface of a Low Pressure Turbine Blade,» 2004.

[117] R. Ciorciari, I. Kirik e R. Niehuis, «Effects of Unsteady Wakes on the Secondary Flows in the Linear T106 Turbine Cascade,» *Journal of Turbomachinery,* vol. 136, 2014.

[118] B. S. Baldwin and H. Lomax, "Thin Layer Approximation and Algebraic Model for Separated Turbulent Flows," *AIAA paper 78--257,* 1978.

[119] D. Degani and L. B. Schiff, "Computation of Turbulent Supersonic Flows Around Pointed Bodies Having Crossflow Separation," *Journal of Computational Physics,* vol. 66, pp. 173-196, 1986.

[120] A. Arnone and R. Pacciani, "IGV-Rotor Interaction Analysis in a Transonic Compressor Using the Navier--Stokes Equations," *ASME Journal of Turbomachinery,* vol. 120, pp. 143-155, 1 1998.

[121] P. R. Spalart and S. R. Allmaras, "A One-equation Turbulence Model for Aerodynamic Flows," *AIAA Paper 92-0439,* 1 1992.

[122] P. R. Spalart and M. Shur, "On the Sensitization of Turbulence Models to Rotation and Curvature," *Aerospace Science and Technology,* vol. 1, pp. 297-302, 1997.

[123] D. C. Wilcox, Turbulence Modeling for CFD, 2nd ed., DCW Ind. Inc., La Cañada, CA, USA, 1998.

[124] F. R. Menter, "Two-Equations Eddy Viscosity Turbulence Models for Engineering Applications," *AIAA J.,* vol. 32, pp. 1598-1605, 8 1994.

[125] D. C. Wilcox, "Formulation of the k-ω Turbulence Model Revisited," *#AIAAJ#,* vol. 46, pp. 2823-2838, 11 2008.

[126] R. Pacciani, M. Marconcini, A. Fadai-Ghobti, S. Lardeau e M. A. Leschziner, «Calculation of High-Lift Cascades in Low Pressure Turbine Conditions Uisng a Three-Equation Model,» *Journal of Turbomachinery,* vol. 133, n. 3, 2011.

[127] R. B. Langtry e F. R. Menter, «Correlation-Based Transition Modeling for Unstructured Parallelized Computational Fluid Dynamics Codes,» *AIAA Journal,* vol. 47, 2009.

[128] R. Pacciani, M. Marconcini, A. Arnone e F. Bertini, «An Assessment of the Laminar Kinetic Energy Concept for the Prediction of High-Lift, Low-Reynolds Number Cascade Flows,» *Proceedings of the Institution of Mechanical Engineers, Part A: Journal of Power and Energy,* vol. 225, n. 7, pp. 995-1003, 2011.

[129] R. Pacciani, M. Marconcini, A. Arnone e F. Bertini, «Predicting High-Lift LP Turbine Cascades Flows Using Transition-Sensitive Turbulence Closures,» *Journal of Turbomachinery,* vol. 136, 2014.

[130] A. Jameson, W. Schmidt and E. Turkel, "Numerical Solutions of the Euler Equations by Finite Volume

Methods Using Runge--Kutta Time--Stepping Schemes," *AIAA paper 81--1259,* 1981.

[131] R. H. Ni, "A Multiple-Grid Scheme for Solving the Euler Equations," *AIAA paper 81-1025,* 1981.

[132] D. Holmes and S. Tong, "A Three-Dimensional Euler Solver for Turbomachinery Blade Rows," *ASME J. Eng. Gas Turbines Power,* vol. 117, no. 2, pp. 258-264, 1985.

[133] R. C. Swanson and E. Turkel, "On Central-Difference and Upwind Schemes," *Journal of Computational Physics,* vol. 101, pp. 292-306, 1992.

[134] L. Martinelli and A. Jameson, "Validation of a Multigrid Method for Reynolds Averaged Equations," *AIAA paper 88--0414,* 1988.

[135] R. C. Swanson and E. Turkel, "Artificial Dissipation and Central Difference Schemes for the Euler and Navier--Stokes Equations," *AIAA paper 87--1107--CP,* 1987.

[136] P. L. Roe and M. J. Baines, "Algorithms for advection and shock problems," in *Proceedings of the Fourth GAMM Conference on Numerical Methods in Fluid Mechanics, Notes on Numerical Fluid Mechanics, 5; p. 281*, Vieweg, 1981.

[137] M. Arora and P. L. Roe, "A Well-Behaved TVD Limiter for High-Resolution Calculations of Unsteady Flow," *Journal of Computational Physics,* vol. 132, pp. 3-11, 1997.

[138] A. Arnone, "Viscous Analysis of Three–Dimensional Rotor Flow Using a Multigrid Method," *J. Turbomach.,* vol. 116, no. 3, pp. 435-445, 1994.

[139] A. Arnone, M. S. Liou and L. A. Povinelli, "Integration of Navier-Stokes Equations Using Dual Time Stepping and a Multigrid Method," *AIAA Journal,* vol. 33, pp. 985-990, 6 1995.

[140] A. Arnone, "Multigrid Methods for Turbomachinery Navier-Stokes Calculations," in *Solution Techniques for Large--Scale CFD Problems*, 1995.

[141] A. Lerat, "Une Classe de Schemas aux Differences Implicites Pour les Systemes Hyperboliques de Lois de Conservation," *Comptes Rendus Hebdomadaires des Seances de l'Academic des Sciences, Series A: Sciences Mathematiques,* vol. 288A, 1979.

[142] A. Jameson, "The Evolution of Computational Methods in Aerodynamics," *J. Appl. Mech.,* vol. 50, 1983.

[143] A. Brandt, "Multi-Level Adaptive Computations in Fluid Dynamics," *AIAA paper 79-1455,* 1979.

[144] P. Boncinelli, F. Rubechini, A. Arnone, M. Cecconi and C. Cortese, "Real Gas Effects in Turbomachinery Flows: a CFD Model for Fast Computations," *ASME paper 2003--GT--38101,* 2003.

[145] A. J. Chorin, «A Numerical Method for Solving Incompressible Viscous Flow Problems,» *Journal of Computational Physics,* vol. 2, pp. 12-26, 1967.

[146] M. Giovannini, M. Marconcini, A. Arnone and A. Dominguez, "A Hybrid Parallelization Strategy of a CFD Code for Turbomachinery Applications," in *11th European Turbomachinery Conference, paper ETC2015-188*, Madrid, 2015.

[147] J. L. Steger and R. L. Sorenson, "Automatic Mesh Point Clustering Near a Boundary in Grid Generation with Elliptic Partial Differential Equations," *Journal of Computational Phisycs,* vol. 33, pp. 405-410, 12 1979.

[148] T. Mitchell, Machine Learning, McGraw Hill, 1997.

[149] F. Vanti, «Development of an Automatic Procedure for Aeromechanical Optimization of Axial Turbomachines,» Università degli Studi di Firenze, Firenze, 2020.

[150] Y. Goldberg, «A Primer on Neural Network Models for Natural Language Processing,» *Journal of Artificial Intelligence Research,* vol. 57, pp. 345-420, 2016.

[151] S. Lieblein, «Experimental Flow in 2D Cascades. The aerodynamic Design of the Axial Flow Compressor,» NACA RME, 1956.

[152] J. Hourmouziadis, «Aerodynamic design of low pressure turbines,» 1989.

[153] K. Hashimoto e T. Kimura, «Preliminary Study of Forward Loaded Cascades Designed with Inverse Method for Low Pressure Turbine,» 1984.

[154] H. Hoheisel, R. Kiock, H. J. Lichtfuss e L. Fottner, «Influence of Free-stream Turbulence and Blade Pressure

Gradient on Boundary Layer and Loss Behaviour of Turbine Cascades,» 1986.

[155] R. J. Howell, O. N. Ramesh, H. P. Hodson, N. W. Harvey e V. Schulte, «High Lift and Aft Loaded Profiles for Low Pressure Turbines,» in *Proceedings of ASME TURBOEXPO 2000*, Munich, 2000.

[156] R. J. Howell, H. P. Hodson, V. Schulte, H. P. Schiffer, F. Haselbach e N. W. Harvey, «Boundary Layer Development in the BR710 and BR715 LP Turbines - the Implementation of High Lift and Ultra High Lift concepts,» *Journal of Turbomachinery,* vol. 124, 2001.

[157] F. Rubechini, A. Schneider, A. Arnone, F. Daccà, C. Canelli e P. Garibaldi, «Aerodynamic Redesigning of an Industrial Gas Turbine,» Vancouver, 2011.

[158] J. D. Coull, R. L. Thomas e H. P. Hodson, «Velocity Distributions for Low Pressure Turbines,» *Journal of Turbomachinery,* vol. 132, 2010.

[159] H. T. K. K. A. Rona, «Perspectives on the Treatment of Secondary Flows in Axial Turbines,» in *Proceedings of International Conference on Applied Energy*, Cardiff, 2017.

[160] M. E. Lyall, P. I. King, J. P. Clark e R. Sondergaard, «Endwall Loss Reduction of High Lift Low Pressure Turbine Airfoils Using Profile Contouring - PART I: Airfoil Design,» *Journal of Turbomachinery,* vol. 136, n. 8, 2014.

[161] T. J. Praisner, E. Allen-Bradley, E. A. Grover, D. C. Knezevici e S. A. Sjolander, «Application of Non-Axisymmetric Endwall Contouring to Conventional and High-Lift Turbine Airfoils,» in *Proceedings of TurboExpo*, 2007.

[162] M. Giovannini, F. Rubechini, M. Marconcini, A. Arnone e F. Bertini, «Reducing Secondary Flow Losses in Low-Pressure Turbines: the "snaked" blade,» in *Proceedings of 13th European Conference on Turbomachinery Fluid Dynamics & Thermodynamics*, Lausanne, 2019.

[163] H. Prumper, «Application of Boundary Layer Fences in Turbomachinery,» AGARD, 1972.

[164] C. A. Bielek, «Gas Turbine Nozzle with a Flow Fence». USA Brevetto US 8,944,774 B2, 3 February 2015.

[165] F. Bertini, «Method for Making a Shaped Turbine Aerofoil». USA Brevetto US 9,506,348, B2, 29 November 2016.

[166] D. Simoni, M. Berrino, M. Ubaldi, P. Zunino e F. Bertini, «Off-Design Performance of a Highly Loaded LP Turbine Cascade Under Steady and Unsteady Incoming Flow Conditions,» *Journal of Turbomachinery,* vol. 137, n. 7, 2015.

[167] M. Marconcini, R. Pacciani, A. Arnone e F. Bertini, «Low-Pressure Turbine Cascade Performance Calculations with Incidence Variation and Periodic Unsteady Inflow Conditions,» Montreal, 2015.

[168] N. Harvey, G. Brennan, D. Newman e M. Rose, «Improving Turbine Efficiency Using Nonaxisymmetric Endwalls: Validation in the Multi-row Environment and with Low Aspect Ratio Blading,» 2012.

[169] G. Ingram, D. Gregory-Smith e N. Harvey, «Investigation of a Novel Secondary Flow Feature in a Turbine Cascade with Endwall Profiling,» *Journal of Turbomachinery,* vol. 127, n. 1, pp. 209-214, 2005.